Technical Report

NATIONAL ENVIRONMENTAL SATELLITE CENTER NESC-38

Angular Distribution of Solar Radiation Reflected from Clouds as Determined from TIROS IV Radiometer Measurements

I. RUFF, R. KOFFLER, S. FRITZ,
J.S. WINSTON, and P.K. RAO

ATMOSPHERIC SCIENCES
LIBRARY
MAY 26 1967
E. S. S. A.
U. S. Dept. of Commerce

WASHINGTON, D.C.
March 1967

NATIONAL ENVIRONMENTAL SATELLITE CENTER REPORTS

(1-3, 5-23, 26, 28-33 are available through the Clearinghouse for Federal Scientific and Technical Information, U. S. Department of Commerce, Sills Bldg., Port Royal Road, Springfield, Virginia 22151. The CFSTI number and price follow each entry.)

Number

1. Cloud Conference Summary, L. F. Whitney, Jr., (July 1960) PB 163 727 $2.60
*2. Analysis of Project Hugo Test Firing, December 5, 1958, L. F. Hubert, (August 1960) PB 163 728 $5.60
*3. Preliminary Studies of Atmospheric Energy Parameters, J. S. Winston, (January 1961) PB 163 729 $3.60
4. Open
5. TIROS I - Camera Attitude Data, Analysis of Location Errors. and Derivation of Correction for Calibration, L. F. Hubert, (April 1961) N 6211116 $6.60
   Supplement to 5: Canadian Grids for TIROS I, Additional Orientation Data, Errata, L. F. Hubert, (June 1961) N6211117 $4.60
*6. Nimbus Data Utilization Plan, (Anon), (April 1961) PB 163 732 $2.60
7. Identification of Cloud Forms from TIROS I Pictures, C. O. Erickson and L. F. Hubert, (June 1961) N6214286 $7.60
8. Ice Photography from the Meteorological Satellites TIROS I and TIROS II, D. Q. Wark and R. W. Popham, (March 1962) PB 163 734 $4.60
*9. Documentation for TIROS III Television Data, L. F. Hubert, (March 1962) PB 163 735 $6.60
*10. Infrared Flux and Surface Temperature Determinations from TIROS Radiometer Measurements, D. Q. Wark, G. Yamamoto, and J. H. Lienesch, (August 1962) N6311881 $8.60
   Supplement to 10: (April 1963) PB 165 208 $1.10
11. Perspective Locator Grids for TIROS Pictures, M. H. Frankel and C. L. Bristor, (October 1962) PB 163 737 $4.60
12. Catalog of Supplemental Meteorological Data Concurrent with TIROS Satellite Observations (TIROS I-V), R. L. Pyle, (August 1962) PB 163 738 $4.60
*13. Conference on Sferics Measurements, S. Soules (Ed.), (October 1962) PB 163 739 $5.60
14. A Technique for Precise Analysis for Satellite Data - Vol. 1, Photogrammetry, T. Fujita, (February 1963) PB 163 740 $9.60
15. Calibration of Image Distortion in TIROS Wide Angle Photography, R. C. Doolittle, (July 1963) PB 163 741 $5.60
16. Documentation for TIROS IV Television Data, R. L. Pyle, (May 1963) PB 163 742 $8.10
17. On the Use of Redundancy in the Design of Operational Satellites, S. F. Singer, (April 1963) PB 163 743 $1.60
18. An Analysis of CDA Station Effectiveness in Relation to Satellite Orbit, R. L. Pyle and S. F. Singer, (July 1963) PB 163 744 $3.60

*Out of Print

(Continued on inside of back cover)

U.S. DEPARTMENT OF COMMERCE
Alexander B. Trowbridge, Acting Secretary

ENVIRONMENTAL SCIENCE SERVICES ADMINISTRATION
Robert M. White, Administrator

NATIONAL ENVIRONMENTAL SATELLITE CENTER
David S. Johnson, Director

ESSA TECHNICAL REPORT NESC-38

Angular Distribution of Solar Radiation Reflected from Clouds as Determined from TIROS IV Radiometer Measurements

QC
879.5
.U45

I. RUFF, R. KOFFLER, S. FRITZ, J. S. WINSTON, and P. K. RAO

U.S. NATIONAL ENVIRONMENTAL SATELLITE CENTER REPORT No. 38
WASHINGTON, D.C.
March 1967

M07.362.2
U58Tro
no.38

140 652

National Oceanic and Atmospheric Administration
TIROS Satellites and Satellite Meteorology

ERRATA NOTICE

One or more conditions of the original document may affect the quality of the image, such as:

Discolored pages
Faded or light ink
Binding intrudes into the text

This has been a co-operative project between the NOAA Central Library and the Climate Database Modernization Program, National Climate Data Center (NCDC). To view the original document contact the NOAA Central Library in Silver Spring, MD at (301) 713-2607 x124 or Library.Reference@noaa.gov.

HOV Services
Imaging Contractor
12200 Kiln Court
Beltsville, MD 20704-1387
January 26, 2009

Addendum

Reference 6 has been published in Journal of the Atmospheric Sciences, Vol. 24, No. 1, January 1967, pp. 70-79.

Errata

Page 8, Extreme right hand side of Eq. 10 should be multiplied by a factor of 1/2.

Page 8, First line after Eq. 12: Omit "half".

Figure 6. Same as figure 5, for wall direction in period 1 vs. wall direction in period 3.

Figure 39, line 3: for "0", read " ρ ".

Figure 44, line 3 of caption, should read:

"tion, $\zeta < 60^{\circ}$; (2) diffuse assumption, all δ ; (3) empirical patterns when"

Figure 44, at $\phi = 55^{\circ}$S, read " $\triangle$ " for " $\boxdot$ ".

Errata

Page 11, second paragraph, fifth sentence should read: "Figure 38 shows the results of these calculations, giving the reflection coefficient and the reflected filtered flux as a function of solar zenith angle. The reflected flux decreases monotonically with solar zenith angle, as a consequence of the cos ζ decrease of the incoming energy per unit horizontal area."

Figure 23, page 39, and figure 32, page 48 should have double-headed arrows along the line $\alpha = 0°$, as follows:

Figure 23

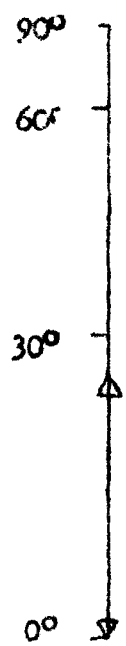

Figure 32

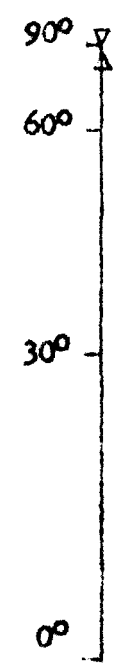

Figures 40, 41, and 42, pages 56, 57, and 58 respectively, should have solid and dashed lines along the θ axis, as follows:

Figure 40

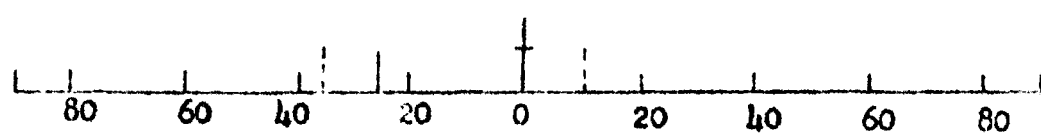

Figure 41

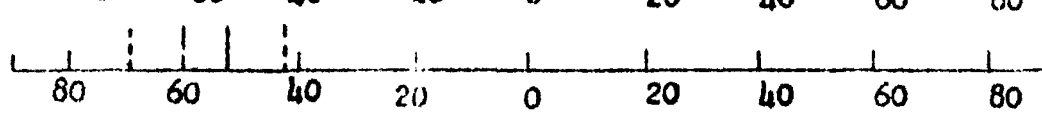

Figure 42

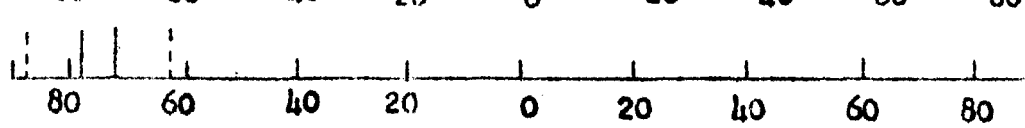

Blank page retained for pagination

TABLE OF CONTENTS

		Page
ABSTRACT		1
I.	INTRODUCTION	1
II.	DATA	2
III.	DATA RESTRICTIONS AND RELIABILITY	4
IV.	RESULTS	8
V.	DETERMINATION OF FLUXES	10
VI.	COMPARISON WITH THEORY	11
VII.	COMPARISON OF EMPIRICAL AND DIFFUSE RESULTS	13
ACKNOWLEDGEMENTS		15
REFERENCES		16

ANGULAR DISTRIBUTION OF SOLAR RADIATION REFLECTED FROM CLOUDS AS DETERMINED FROM TIROS IV RADIOMETER MEASUREMENTS

I. Ruff, R. Koffler, S. Fritz, J. S. Winston, and P. K. Rao
National Environmental Satellite Center

ABSTRACT

The pattern of reflection of solar radiation from clouds as a function of angle is obtained by statistical analysis of observations from the TIROS IV visible radiation channel (0.55 μ to 0.75 μ). Readings from the water vapor window channel (8 μ to 12 μ) were used to select cases in which clouds fill the field of view of the sensor. The results show a generally non-isotropic reflection pattern, which varies with solar zenith angle. The anisotropy is greatest for large values of solar zenith angle, the main feature in these cases being the high intensity values of the radiation reflected at azimuths close to 180° from the sun, and at large zenith angles.

I. INTRODUCTION

The basic energy source for the earth-atmosphere system is the net heating represented by the difference between absorbed solar radiation and outgoing terrestrial radiation. Both of these quantities can best be investigated from satellites, since measurements are then made above the atmosphere, allowing, in principle, a true determination of the energy inputs and outgo from the earth-atmosphere system. Satellites also provide comprehensive coverage, in both space and time, over the entire earth, which is impossible with other measuring systems. The quantities actually measured by a satellite, however, are usually not the desired energies themselves, but rather quantities related to these energies. For example, a satellite cannot measure the solar energy abosrbed by the earth-atmosphere system, but rather the energy reflected and scattered back to space. By subtracting this reflected and scattered radiation from the presumably known incoming solar radiation, the amount of energy remaining in the earth-atmosphere system may be determined.

A more difficult problem arises from the fact that a satellite senses the radiation coming from a given area of the earth at a given time at only a single angle, regardless of the type of sensor employed. This is most obviously true for a narrow angle sensor, such as is found in the scanning radiometers of the TIROS satellites. However, even though a sensor with wide angular coverage will observe simultaneously radiation emerging at many different angles, the intensity at each angle will have originated from a different area of the earth. Thus, in order to determine the total energy passing to space at a given place and time, it is necessary to know the pattern of the outgoing radiation as a function of angle.

With regard to incoming solar radiation, clouds represent one of the most important factors influencing the amount and distribution of its absorption, because of their variability and their generally high reflectivity. Thus a study of the angular reflection pattern of clouds for solar radiation will help greatly in interpreting observations from satellites of reflected solar radiation, and hence in determining the net heating. Moreover, the study of the distribution of reflected solar energy is an interesting problem in physical meteorology in its own right.

It would be preferable to know the reflection pattern of each individual cloud observed by a satellite. This is not possible at present. However, a reflection pattern representative of the average of a large number of clouds may be obtained by a statistical study of the satellite data. Such a pattern, applied to the determination of absorbed solar radiation, would be expected to yield better results than the assumption of an isotropic reflection pattern for clouds.

II. DATA

The data used in this study were the values given on the National Aeronautics and Space Administration Final Meteorological Radiation (FMR) magnetic tapes for TIROS IV, channel 5 (0.55-0.75 μ) and channel 3 (0.2-6.0 μ). The quantities which are observed are intensities (energy in a given direction, per unit time, per unit solid angle, per unit area normal to the beam). However, values listed on the FMR tapes are in units of flux (watt m^{-2}). These are derived quantities, based on the calibration procedure [5] in which as the radiometer viewed a diffusely reflecting target of known reflectivity and with known illumination, the radiometer output was then plotted as a function of the total flux reflected from the target. The use of a calibration based on a diffuse target, combined with expressing the terrestrial reflection in units of flux, makes the implicit assumption that the terrestrial features viewed by the radiometer are diffuse reflectors.

Relationships involved in an examination of cloud reflection may be presented by first considering the geometry of the reflection, shown in figure 1. A spherical coordinate system is centered at the point of reflection, having coordinates of zenith angle, θ , and of azimuth, α . The azimuth is relative to the azimuth of the solar beam, and is positive in a clockwise direction. ζ is the zenith angle of the sun at the point of reflection. The scattering angle, ψ , is the angle between the incoming solar beam and the reflected ray, and is defined as zero when the reflected ray is directed toward the sun.

ψ is related to θ, α, and ζ by

$$\cos\psi = \cos\zeta\cos\theta + \sin\zeta\sin\theta\cos\alpha \tag{1}$$

The relationship between intensity and flux may be examined by letting $I(\theta,\alpha,\zeta)$ be the intensity at zenith angle θ, azimuth α, and solar zenith angle ζ. Then the total reflected flux from a unit horizontal area, and at a fixed solar zenith angle, is given by:

$$F(\zeta) = \int_0^{\pi/2}\int_0^{2\pi} I(\theta,\alpha,\zeta)\sin\theta\cos\theta\, d\alpha\, d\theta \tag{2}$$

For the case of diffuse reflection, $I(\theta,\alpha,\zeta)$ = constant (for a given value of ζ), and

$$F_{diffuse}(\zeta) = \pi I(\zeta) \tag{3}$$

The flux incident on a horizontal surface is given by

$$F_i(\zeta) = \cos\zeta\int_0^{\infty} S(\lambda)\, d\lambda \tag{4}$$

where $\int_0^{\infty} S(\lambda)\, d\lambda$ is the solar constant, λ being wavelength. Therefore, for a reflection pattern and reflection coefficient which do not depend on solar zenith angle, the intensity as a function of solar zenith angle is given by

$$I(\theta,\alpha,\zeta) = I(\theta,\alpha,0)\cos\zeta \tag{5}$$

Since the purpose of this study is to investigate the actual angular reflection pattern of clouds, it is necessary to work with the observed intensities, rather than with fluxes which assume diffuse reflection. The intensities may be obtained from the diffuse fluxes given on the FMR tapes by using equation (3):

$$I(\theta,\alpha,\zeta) = \frac{F_{diffuse}(\zeta)}{\pi} \tag{6}$$

It should be noted that the intensity obtained is a function of zenith angle and azimuth, since the radiometer observation on which it is based was taken in a particular direction.

Even if the angular reflection pattern remains constant with solar zenith angle, it will be seen from equation (5) that the magnitude of the reflected intensity will decrease as the solar zenith angle increases. In order to facilitate comparison of patterns at different solar zenith angles, an adjusted intensity was defined from equation (5):

$$I_a(\theta,\alpha) = I(\theta,\alpha,0) = \frac{I(\theta,\alpha,\zeta)}{\cos\zeta} \tag{7}$$

Since the TIROS radiometer observations are made through a filter, having filter function $\phi(\lambda)$, where λ is wavelength,

$$I(\theta,\alpha,\zeta) = \int_0^\infty I(\theta,\alpha,\zeta,\lambda)\,\Phi(\lambda)\,d\lambda \tag{8}$$

$I(\theta,\alpha,\zeta,\lambda)$ being the total intensity, and $I(\theta,\alpha,\zeta)$ being the intensity as seen by the radiometer. In order to determine the reflection coefficient from the observations, the outgoing flux found from equation (2) must be divided, not by the total incoming flux given in equation (4), but by a filtered incoming flux:

$$F_{I_\Phi}(\zeta) = \cos\zeta \int_0^\infty S(\lambda)\,\Phi(\lambda)\,d\lambda \tag{9}$$

where $S(\lambda)$ is the solar constant as a function of wavelength. This step assumes that the spectral distribution of the reflected energy is similar to the spectrum of the incident energy [1], and will be explained further in the discussion of equation (15), below.

III. DATA RESTRICTIONS AND RELIABILITY

In order to restrict the data to energy reflected from clouds, it is necessary to determine for every observation whether or not clouds fill the field of view of the sensor. Because of the large number of observations being processed, it is not practical to examine each situation individually. It is therefore necessary to use an indirect criterion, preferably information already on the FMR tapes. Such a criterion can be obtained from the outgoing radiation in the water vapor window (8-12 μ) observed by channel 2 of the TIROS radiometer. Most of the energy emerging to space in the window region originates at the surface of the earth or at a cloud top, and is comparatively little affected by the intervening atmosphere. Since the emissivities of fairly thick clouds and of the earth's surface are close to one, both clouds (except thin clouds) and surface may be treated as blackbodies. Thus the energy received by channel 2 is closely related to the actual temperature of the emitting surface. For these reasons, a channel 2 observation is usually expressed as an "equivalent blackbody temperature", T_e. This is the temperature of a blackbody, which if viewed by the channel 2 radiometer, would result in the same radiometer output as was the case for the actual observation.

Since the large-scale temperature structure of the troposphere shows a monotonic decrease with height, except in the vicinity of the surface, the temperature of a cloud top (and thus the equivalent blackbody temperature) which is more than a few thousand feet high is generally lower than that of the surface. Situations in which clouds fill only part of the field of view of the sensor, or in which the clouds are thin, usually have an equivalent blackbody temperature intermediate between the temperatures of the surface and of the cloud top. It is thus possible in principle to select some value of channel 2 equivalent blackbody temperature, and to state that all lower temperatures indicate middle or high overcast, and that higher temperatures

indicate clear conditions, partly cloudy conditions, or the presence of a lower-level overcast. High-latitude winter observations having low surface temperatures provide one clear exception to this. However, TIROS IV observed only at latitudes less than 60°, and in the spring, thus largely eliminating this source of error. Two types of errors result from the use of a single value of T_e as a criterion. If a very low channel 2 temperature is selected, only high, cold clouds will be included, and the sample size will be considerably reduced; although for cases so selected, there will be a high probability of clouds filling the field of view of the sensor. Choice of a high temperature, on the other hand, while yielding a larger and more varied sample of clouds, will permit partly cloudy or even clear cases to be included in the sample. On the basis of case studies [2, 3], a value of $T_E \leq 255°K$. for channel 2 was chosen as being a reasonable criterion for selection of observations of predominantly cloudy conditions.

For the chosen observations, the method of analysis consisted of determining the joint frequency distribution of the four variables θ, α, ζ, and I_a. A median value of I_a was then calculated for each joint interval of the three variables θ, α, and ζ from the corresponding frequency distribution of I_a. These determinations were made separately for three samples of satellite data: passes 127-612 (February 17 - March 23, 1962), 662-1053 (March 26 - April 22, 1962), and 1061-1548 (April 23 - May 27, 1962).

Each radiation channel on TIROS consists of a sensor which receives radiation alternately from directions at angles of 45° and 135° with the optic axis of the cameras. The 45° direction is termed the "floor", since it views through the baseplate of the satellite. Similarly, the 135° direction is termed the "wall". Details of the arrangement of the radiometers may be found in the TIROS IV Radiation User's Manual [5].

Figure 2 is a histogram of the number of observations made by channel 5 during passes 127-612 of TIROS IV. The abscissa is scattering angle, and the number of observations is plotted separately for the floor and wall directions. The satellite is kept oriented such that the cameras point toward the earth during daylight. Consequently, most of the observations of solar reflection are made in the floor direction, as can be seen in figure 2. It is also evident that scattering angles less than 70° are observed almost exclusively in the floor direction while the wall direction is responsible for almost all coverage at scattering angles greater than 110°.

Two examples of actual distributions for passes 127-612 are given in figures 3 and 4. These figures present maps of the upward hemisphere, the pole of the projection being the zenith, and with zenith angle (θ) increasing outward from the pole. The outermost circle represents the horizon ($\theta = 90°$). The radius extending upward from the pole is the azimuth of the sun ($\alpha = 0°$), with the azimuth of the reflected ray measured clockwise from this line. Each map is for a different range of solar zenith angle. Isopleths are of the number of observations made in the wall and floor direction. Figure 3 shows the case of relatively small ζ (high sun). Coverage is largely in the floor direction, with some observations made in the wall direction over a small range of angles. For a lower sun, however, (fig. 4), the wall provides the bulk of the coverage in the forward direction, back reflection being seen only by the floor.

It is evident from figures 2, 3, and 4 that in order to obtain even approximately complete coverage over the upward hemisphere for all solar zenith angles, observations in both floor and wall directions must be used. It is possible to compare directly values obtained from the wall and floor directions only if their responses show reasonable agreement. Therefore, for both channel 3 and channel 5, the relative response in the wall and floor directions was studied as a function of time. The data were first compared in pairs as shown in table 1. This was done, for each channel, by pairing the wall with the floor in period 1 (passes 127-612), the wall in period 1 with the wall in period 3 (passes 1061-1548), the floor in period 1 with the floor in period 3, and the wall with the floor in period 3. For those joint intervals of solar zenith angle, ζ , reflected zenith angle, θ , and reflected azimuth, α , in which there were at least 50 observations for each member of the pair, scatter diagrams were plotted of the corresponding median values of the adjusted intensity. Least square lines were fitted, minimizing the perpendicular distances from the points to the line, and linear correlation coefficients were calculated. The equations of the fitted lines, along with the correlation coefficients, are summarized in table 1. The scatter diagrams are presented in figures 5-12, figures 5-8 being for channel 5 (0.55 - 0.75 μ), and figures 9-12 for channel 3(0.2 - 6.0 μ).

Table 1

COMPARISON OF SENSOR RESPONSE

Subscripts: f = floor, w = wall, 1 = period 1, 3 = period 3

I_a in watt m^{-2} $strdn^{-1}$

Equation of Least Square Lines	Mean Values	Correlation Coefficient
Channel 5		
$(I_a)_{f1} = 1.166\ (I_a)_{w1} - 2.49$	$\overline{(I_a)_{w1}} = 11.44$ $\overline{(I_a)_{f1}} = 10.85$	.74
$(I_a)_{w3} = 0.886\ (I_a)_{w1} - 0.38$	$\overline{(I_a)_{w1}} = 15.56$ $\overline{(I_a)_{w3}} = 13.41$	.88
$(I_a)_{f3} = 0.144\ (I_a)_{f1} + 6.64$	$\overline{(I_a)_{f1}} = 10.44$ $\overline{(I_a)_{f3}} = 8.12$	.37
$(I_a)_{f3} = 0.258\ (I_a)_{w3} + 5.46$	$\overline{(I_a)_{w3}} = 10.79$ $\overline{(I_a)_{f3}} = 8.23$	.74
Channel 3		
$(I_a)_{f1} = 0.984\ (I_a)_{w1} - 1.69$	$\overline{(I_a)_{w1}} = 12.62$ $\overline{(I_a)_{f1}} = 10.72$	.68
$(I_a)_{w3} = 0.977\ (I_a)_{w1} - 2.18$	$\overline{(I_a)_{w1}} = 17.35$ $\overline{(I_a)_{w3}} = 14.80$	.91
$(I_a)_{f3} = 0.578\ (I_a)_{f1} + 3.46$	$\overline{(I_a)_{f1}} = 10.54$ $\overline{(I_a)_{f3}} = 9.54$	.70
$(I_a)_{f3} = 0.518\ (I_a)_{w3} + 4.67$	$\overline{(I_a)_{w3}} = 12.13$ $\overline{(I_a)_{f3}} = 10.96$	.62

The results are similar for both channel 3 and channel 5. There is reasonably good agreement between the floor and wall directions during period 1, and the wall observations for period 1 are in quite good agreement with those for period 3. The floor sensor, however, shows a considerable change between the two periods. This is especially evident in the case of channel 5, where there is a marked restriction in the range of intensities observed in period 3 as compared to period 1 (fig. 7). Finally, as may be seen from the equations of the least-square lines, or from the mean value, agreement between the wall and floor in period 3 is rather poor, although the comparatively large value of the correlation coefficient indicates only a moderate amount of scatter.

In order to use the values obtained during period 3 (and also period 2, the analyses of which have not been shown) it would be necessary to adjust empirically the floor values to those of the wall, and to then adjust both to the levels of period 1. In view of the additional uncertainties that such a procedure would introduce, it was decided to restrict the analysis to cases that do not require adjustment in order to achieve correspondence between wall and floor sensors. Therefore, only period 1 (passes 127-612) was examined further.

Either channel 3 or 5 would be satisfactory for this study. Channel 3 would be the better choice for the purpose of incorporation into investigations of the atmospheric heat budget, since it covers essentially the entire solar spectrum. The radiation observed by channel 3 is, however, more subject to influences other than reflection from clouds than is the case for channel 5. For example, channel 5 will be much less influenced by small particle scattering of the short wavelengths, or by water vapor absorption in the infrared, than channel 3. Thus channel 5 will yield a truer picture of the actual cloud reflection, although considering to a lesser extent atmospheric processes which affect the total reflected radiation at all wavelengths.

Correspondence between the wall and floor directions for period 1 is about the same for channels 3 and 5. Examination of figures 5 and 9, and of the least-square equations, indicates that channel 5 is slightly better, since the points are grouped more closely along the 45° line. The data for this study were therefore confined to channel 5, although there appears to be only a very slight advantage in this choice. Any major results found for channel 5 are probably applicable to channel 3.

It should be pointed out that the absolute values obtained from channels 3 and 5 on TIROS IV may be in error. Comparisons of reflection data obtained from TIROS with those found from other sources [4] suggests that the TIROS measurements may be low by 20 to 30 percent, although uncertainties in the comparisons make it impossible to state an exact figure. As a result of these uncertainties, this study will not attempt to determine the exact magnitude of the solar energy reflected from clouds, but will attempt to determine only the angular pattern of the reflected radiation.

IV. RESULTS

Figures 13-22 present the distribution of reflected, filtered, adjusted intensity over the upward-facing unit hemisphere, each map being for a single interval of solar zenith angle. The pole of the projection is the zenith. The radius extending upward from the pole is the azimuth of the sun ($\alpha = 0^{\circ}$), with the azimuth of the reflected ray measured clockwise from this line. The zenith angle, θ, increases radially outward from the pole on a scale of sin θ, the outer circle ($\theta = 90^{\circ}$) representing the horizon. The reason for this choice of scale may be seen by taking an average value of intensity over an area of the hemisphere defined by $\theta_1 \leq \theta \leq \theta_2$, $\alpha_1 \leq \alpha \leq \alpha_2$. The energy passing through this area is then, from equation (2),

$$E(\zeta) = \bar{I}(\zeta)\int_{\theta_1}^{\theta_2}\int_{\alpha_1}^{\alpha_2} \sin\theta \cos\theta \, d\alpha \, d\theta = \bar{I}(\zeta)\left[\alpha_2 - \alpha_1\right]\left[\sin^2\theta_2 - \sin^2\theta_1\right] \qquad (10)$$

The general polar projection of a sphere has coordinates of azimuth angle, β , and radius, r. The area of a sector of an annulus on such a projection is thus given by

$$A = \frac{1}{2}(\beta_2 - \beta_1)(r_2^{\,2} - r_1^{\,2}) \qquad (11)$$

If we let $\beta = \alpha$, and r = sin θ, equation (11) becomes

$$A = \frac{1}{2}(\alpha_2 - \alpha_1)(\sin^2\theta_2 - \sin^2\theta_1) \qquad (12)$$

An area on this projection is thus equal to half the factor which multiplies $\bar{I}(\zeta)$ in equation (10), and is consequently the "weighting function" for the intensities appearing on the map. That is, the contribution of a given intensity to the total flux is proportional to the area on the projection covered by that intensity.

The isopleths on these maps are for filtered values of adjusted intensity in units of watt m.$^{-2}$ strdn.$^{-1}$, as defined in equation (7). The filtered adjusted intensities may be approximately converted to unfiltered adjusted intensities by multiplying the filtered values by the ratio of the unfiltered to the filtered solar constant, the value of which is 12.80 (see discussion of equation 15). The analysis was performed only for those median values of adjusted intensity calculated from at least 50 observations. Every such value was considered, and no further smoothing was applied to these maps. The range of solar zenith angles is shown by a double-headed arrow along the line $\alpha = 0^{\circ}$. Observations at scattering angles less than about 10° cannot be made, since the complementary sensor is then looking directly at the sun, thus saturating the detector. Values which are shown within such regions are actually taken at neighboring angles, although within the solid angle at the midpoint of which the values are plotted.

It will be seen that on none of these maps is there exact symmetry about the line $\alpha = 0^\circ - 180^\circ$. In the case of a single cloud deck, such asymmetry may result from irregularities in the gross features, such as a wavy surface, an overall slope, extension of towers above the general mass, etc. With a sufficiently large random sample, however, these effects should cancel, and the reflection pattern should be symmetrical. In the maps presented here, there is a strong tendency toward symmetry, which is, however, not fully achieved. In particular, the intensities in the region $0^\circ < \alpha < 60^\circ$ are generally higher than the intensities at azimuths $300^\circ < \alpha < 360^\circ$. These departures from symmetry are probably due to lack of a sufficiently large random sample. Such a lack is responsible for incompleteness of the angular coverage, and may also result in biases in the clouds viewed. For example, certain angles may be viewed preferentially at particular times of day, or in particular geographic locations. However, the exact reasons for the lack of complete symmetry in the results have not been investigated.

The pattern for high sun (fig. 13) shows a flat field with approximately radial symmetry, the intensity values decreasing toward the horizon. When the solar zenith angle increases to the range $25^\circ.8$-$36^\circ.9$ (fig. 14), two separate areas of high intensity appear, one at small azimuth, near the zenith angle of the sun, and the second near an azimuth of 180°, close to the horizon. These two centers maintain their identity as the solar zenith angle continues to increase (figs. 15-20, $36^\circ.9 \leq \zeta < 78^\circ.5$). For this range of solar zenith angles, the high intensity area near $\alpha = 0^\circ$ is located such that its center is near the zenith angle of the sun, while the central value of the adjusted intensity remains at about 12 watts $m.^{-2}$ $strdn.^{-1}$. At very high solar zenith angles (figs. 21-22, $78^\circ.5 \leq \zeta \leq 90^\circ.0$) this area of high adjusted intensity does not appear. However, this may be due only to a lack of observations near the horizon.

The area of high intensity near $\alpha = 180^\circ$ maintains its position at or near the horizon. The exception to this, in figure 16, may be due to sampling irregularities. This area increases in maximum adjusted intensity directly with solar zenith angle. The actual central value of the adjusted intensity cannot be specified, because of the lack of observations close to the horizon.

The area of low adjusted intensity located between the two highs increases in extent and becomes smaller in central value as the solar zenith angle increases, and as the high near $\alpha = 0^\circ$ recedes toward the horizon.

These results represent the average reflection pattern of clouds. However, since the lack of symmetry and the irregularities present in the fields of values probably represent various errors and uncertainties in the observations, a smoothed and symmetrized form of these patterns may be more representative of the actual reflection pattern. Symmetry about the line $\alpha = 0^\circ$-180° was imposed by taking means, weighted according to number of observations, of each pair of values which have the same value of zenith angle, and with their azimuths related by $\alpha_2 = 360^\circ - \alpha_1$. The number of observations for each symmetrized point was then the sum of the number for the individual points of the pair. The resultant fields of filtered adjusted intensities were analyzed and smoothed subjectively. Only points which contained at least 50 observations in the symmetrized field were considered. In some cases this results in some paired

values being considered in the analysis, although the individual members of the pair had a number of observations too small to be considered in the analysis of figures 13-22. The symmetrized analyses are presented in figures 23-32, for half the hemisphere; the other half is identical. As is to be expected, the basic features are the same as for the unsmoothed patterns of figures 13-22.

The symmetrized patterns of the filtered adjusted intensity are presented as a function of scattering angle (ψ) and azimuth (η) for alternate intervals of solar zenith angle in figures 33-37. Here the pole of the coordinate system is scattering angle zero; that is, the position of the sun. The scattering angle increases outward from the pole on a linear scale. The azimuth is taken about the pole $\psi = 0$. The direction of zero azimuth passes through the zenith, and is represented on the maps by the line extending vertically downward from the pole. The heavy line enclosing the analyzed area represents the horizon. One center of high intensity remains centered at scattering angle zero, although at large solar zenith angles it is not defined, possibly because of lack of data. The second maximum increases in intensity in the forward direction with increasing scattering angle. There is a strong tendency for the intensity lines to parallel the lines of constant scattering angle. There is still, however, a definite azimuthal dependence of the reflected intensity.

V. DETERMINATION OF FLUXES

The filtered reflected fluxes (i.e., the reflected flux that passes through the filter of the TIROS radiometer) may be calculated by putting equation (8) into equation (2), making use of equation (7), and writing in a form appropriate for calculation from discrete data:

$$F_{\Phi}(\zeta) = \sum_{\theta} \sum_{\alpha} \left\{ \left[\cos\zeta \int_0^{\infty} I_{\alpha}(\theta, \alpha, \lambda)\, d\lambda \right] \sin\theta \cos\theta\, \Delta\alpha\, \Delta\theta \right\} \tag{13}$$

When this filtered flux is divided by the filtered incoming flux on a unit horizontal area, given by equation (9), the filtered reflection coefficient, $R_{\Phi}(\zeta)$, is obtained:

$$R_{\Phi}(\zeta) = \frac{F_{\Phi}(\zeta)}{\cos\zeta \int_0^{\infty} S(\lambda)\Phi(\lambda)\, d\lambda} = \frac{\sum_{\theta} \sum_{\alpha} \left\{ \left[\int_0^{\infty} I_{\alpha}(\theta, \alpha, \lambda)\Phi(\lambda)\, d\lambda \right] \sin\theta \cos\theta\, \Delta\alpha\, \Delta\theta \right\}}{\int_0^{\infty} S(\lambda)\Phi(\lambda)\, d\lambda} \tag{14}$$

If the assumption is now made that the reflection coefficient for all solar wavelengths is identical to that for the filtered energy, $R(\zeta) = R_{\Phi}(\zeta)$, the total reflected flux may be calculated by multiplying equation (14) by the total flux incident on a horizontal surface, given in equation (4).

$$F(\zeta) = R(\zeta)\cos\zeta \int_0^\infty S(\lambda)d\lambda$$

$$= \frac{\int_0^\infty S(\lambda)d\lambda}{\int_0^\infty S(\lambda)\Phi(\lambda)d\lambda} \cos\zeta \sum_\theta \sum_\alpha \left\{ \left[\int_0^\infty I_a(\theta,\alpha,\lambda)\Phi(\lambda)d\lambda \right] \sin\theta\cos\theta\, \Delta\alpha\, \Delta\theta \right\} \tag{15}$$

Thus, with this assumption, filtered intensities and fluxes may be converted to unfiltered values by multiplying them by the ratio of the unfiltered to the filtered solar constant. For TIROS IV, channel 5, this ratio is 12.80.

The data for the calculations of the flux and the reflection coefficient were the symmetrized values of $\int_0^\infty I_a(\theta,\alpha,\lambda)\Phi(\lambda)d\lambda$ used in figures 23-32. It should be noted that in order to make actual calculations, it was necessary to extrapolate the data of figures 23-32 to the horizon. This extrapolation was performed subjectively. The greatest errors probably arise in attempting to extrapolate the forward ($\alpha = 180^\circ$) peak at the largest solar zenith angles. Figure 38 shows the results of these calculations, giving the reflection coefficient and the reflected filtered flux as a function of solar zenith angle, as a consequence of the cos ζ decrease of the incoming energy per unit horizontal area. The reflection coefficient increases with solar zenith angle to the inverval $66^\circ.4 \leq \zeta < 72^\circ.5$, and then decreases as the sun approaches the horizon.

The decrease in the reflection coefficient at high solar zenith angles is somewhat open to question, since the observed intensity values in the forward peak are greatest, and are changing at the greatest rate, for the highest three intervals of solar zenith angle. As a result, the greatest uncertainty in extrapolation, and hence in the value of the reflection coefficient obtained, occurs in these intervals. It was therefore decided to determine what values of the extrapolated intensity would be needed in order to keep the reflection coefficient at the same value at solar zenith angles from $66^\circ.4$ to $90^\circ.0$. Figure 39 shows, for the three intervals of highest solar zenith angle, the azimuthal mean filtered adjusted intensities as a function of zenith angle. In all three cases, the value plotted for $\theta = 84^\circ.5$ is not observed, but is the value required to make the reflection coefficient equal to that found for the interval $66^\circ.4 \leq \zeta < 72^\circ.5$. It will be seen that none of these values would be expected from an extrapolation based only on the intensities observed for smaller values of zenith angle, unless there were some reason to believe that the intensity increased sharply near the horizon. This subject will be discussed further in the following section.

VI. COMPARISON WITH THEORY

Computations have recently been carried out of multiple scattering processes in plane parallel, horizontally infinite clouds consisting of spherical water drops [6]. Various drop size distributions and optical

thicknesses were used. Figures 40-42 show the theoretical values of filtered adjusted intensity along the 0°-180° azimuth plane, using a representative drop size distribution (Gaussian, mean radius 6 μ, standard deviation 1 μ). Each figures is for a different interval of solar zenith angle, and contains curves for three different values of optical thickness. Also plotted are the corresponding filtered adjusted intensities from this study, taken from figures 23, 27, and 30. The range of solar zenith angles for each figure, as well as the 10° limits within which the sensors may observe the sun directly, are shown by the solid and broken lines respectively on the θ scale.

Comparison of the shapes of the empirical and theoretical curves in these figures shows fair overall agreement, particularly for high sun (fig. 40). The main difference between the two sets of results is the somewhat flatter shape of the empirical curves at medium and low sun (figs. 41 and 42). In particular the sharp increase in intensity in the forward ($\alpha = 180^{\circ}$) direction is less pronounced and begins at larger zenith angles in the case of the empirical data than with the theoretical curves. The lack of agreement in the forward peak is probably due to factors in both the theoretical and empirical methods. The uncertainties involved in the empirical results, particularly with respect to the forward peak, have been discussed in the previous section. The uncertainties in the theoretical calculations also occur near the horizon, as a result of the assumption of an infinite, plane-parallel cloud. This assumption will probably yield values of intensity near the horizon that are higher than in reality.

In order to compare the theoretical and empirical results apart from the horizon effects, partial reflection coefficients were computed for that part of the upward hemisphere between zenith angles of $0^{\circ}$and 60°. These values are plotted in figure 43. Theoretical values are given for the same values of optical thickness as were used in figures 40-42. The empirical data show the same general features as are seen in figure 31. All the theoretical curves show a decrease in reflection coefficient at high solar zenith angles. At solar zenith angles less than 70°, the empirical results agree very well with the theoretical results, especially with the results for optical thickness 8.39. At higher solar zenith angles, the empirical values decrease somewhat more rapidly than do the theoretical results. Since the theoretical reflection coefficient for the entire hemisphere increases monotonically with solar zenith angle, it is clear that the reflection at zenith angles between 60° and 90°, in particular the magnitude of the forward peak, is responsible for the differences in shape of the curves of reflection coefficient.

There is no a priori reason to believe that the reflection coefficient for real clouds should either increase monotonically with solar zenith angle, or that it should have a maximum at about $\zeta = 70^{\circ}$. It is possible that there is no fundamental conflict between the theoretical and empirical results, since each is based on somewhat different cloud systems. The theoretical studies apply to a horizontal, plane-parallel cloud, of homogeneous composition, and having a smooth top. In addition, the effect on the reflected radiation of the atmosphere above the cloud has not been considered. The empirical results, however, are obtained from observations of real clouds, which are known to be irregular and inhomogeneous. Furthermore, the empirical results are not for any single cloud, but are rather the average for a large number of clouds. Theoretical calculations for a curved earth, and careful observation at large zenith angles, are needed in order to determine the true value of the forward reflected intensity.

As has been previously mentioned, the intensities observed by the satellite are probably low. The most likely correction factor is about 1.5. There is a possibility that this factor could be as large as 2, but it is rather unlikely that it is larger. Applying the maximum correction factor of 2 to the empirical results of figures 40-42 yields curves which lie somewhere in the region of the theoretical curves for optical thicknesses 4.19 and 8.39. In general, the empirical results will be less than the intensities calculated for an optical thickness of 16.8. It would thus appear that, on the average, the clouds included in this study were of optical thicknesses between 4 and 8, which would correspond, for typical drop size distributions and liquid water contents to clouds about 175 to 350 meters thick.

VII. COMPARISON OF EMPIRICAL AND DIFFUSE RESULTS

Since the reflection patterns obtained in this study were determined statistically, it is not valid to use single observations for purposes of comparison with values obtained with the diffuse assumption. This comparison is most appropriately made by examining mean absorbed fluxes; the final "product" which the reflection patterns are intended to provide. Mean latitudinal unfiltered absorbed fluxes were therefore computed for five single days from TIROS IV, channel 5 data, using both the diffuse assumption and the empirical reflection patterns. The absorbed fluxes obtained by means of the diffuse assumption were calculated in two ways. In the first method, the diffuse assumption was applied to all the data. In the second method, the observations for which the solar zenith angle was greater than 60° were discarded, and the diffuse assumption was applied to the remaining data. The second method was included because such a selection of data had previously been utilized for large scale mapping of TIROS IV solar reflection data [7].

The empirical patterns were applied in only those situations for which the channel 2 equivalent blackbody temperature was less than 255°K. When this temperature was greater than 255°K., the reflected radiation was assumed diffuse, since no empirical model had been determined for these conditions. No restriction was placed on the solar zenith angle.

The results for these five days were presented in figures 44-48. In general, the results calculated by the different methods agree quite well, especially in tropical latitudes. For obvious reasons, few or no results at higher latitudes can be obtained by using the diffuse assumption with the solar zenith angle cut-off. At latitudes where values could be obtained from all three methods, the diffuse assumption, without a limit on solar zenith angle, gives results which generally agree more closely with the empirical results than do the values obtained by using the diffuse assumption with a restriction on solar zenith angle. Since the data samples for the first two of these methods are identical, this result is not unexpected. There is a tendency at higher latitudes for the use of the empirical patterns to yield smaller values of absorbed flux (i.e., larger reflection coefficient) than does the use of the diffuse assumption. Larger differences may be expected in regions poleward of 60°, since here the solar zenith angle is always large, and the empirical reflection patterns depart most from diffuse. However, TIROS IV did not observe at high latitudes, so that no comparison can be made in these regions in the present study.

The comparisons presented for these five days are not intended to represent a complete evaluation of the effects of using the empirical reflection patterns in place of the diffuse assumption, but rather to indicate the types of differences which may occur. The present results appear to indicate that the use of the empirical reflection patterns, rather than the diffuse assumption, yields differences in the calculated values of absorbed solar radiation which, while small, may possibly be significant in determination of the heat budget.

ACKNOWLEDGEMENTS

The authors wish to acknowledge the helpful suggestions of Dr. Albert Arking of the Institute of Space Studies, National Aeronautics and Space Administration.

We also wish to thank Mrs. Jean Hyatt and Mrs. Mary Marini for their aid in the extensive computations and plotting. Thanks are also due to Messrs. Page Bridges, Donald Mercer, and Leonard Hatton for drafting the figures, and to Mrs. Dorothy Pierce and Mrs. Margaret DiNenna for their help in preparing the manuscript.

REFERENCES

1. Fritz, S., P. Krishna Rao, and M. Weinstein, "Satellite measurements of reflected solar energy and the energy received at the ground," Journal of the Atmospheric Sciences, vol. 21, no. 2, pp. 141-151.

2. Fritz, Sigmund, and Jay S. Winston, "Synoptic use of radiation measurements from satellite TIROS II," Monthly Weather Review, vol. 90, no. 1, 1962, pp. 1-9.

3. Pedersen, Finn, and Tetsuya Fujita, "Synoptic interpretation of TIROS III measurements of infrared radiation," Research Paper 19, Mesometeorology Project, Dept. of the Geophysical Sciences, University of Chicago, 1963, 39 pp.

4. Rao, P. Krishna, Elford G. Astling, and Francis J. Winninghoff, "An investigation of degradation errors in TIROS IV scanning radiometer data and the determination of correction factors," Report No. 34, Meteorological Satellite Laboratory, National Environmental Satellite Center, Environmental Science Services Administration, Washington, D. C., 1965, 22 pp.

5. Staff Members, Aeronomy and Meteorology Division, Goddard Space Flight Center, TIROS IV radiation data catalog and users' manual, National Aeronautics and Space Administration, 1963.

6. Twomey, S., H. Jacobowitz, and H. B. Howell, "Light scattering by cloud layers," 1966, (To be published.)

7. Winston, J. S., "Global distribution of cloudiness and radiation for seasons as measured from weather satellites," 1966, (To be published as Chapter VII, Vol. III "Climate of the Free Atmosphere" of World Survey of Climatology, Elsevier Publishing Co., Amsterdam.)

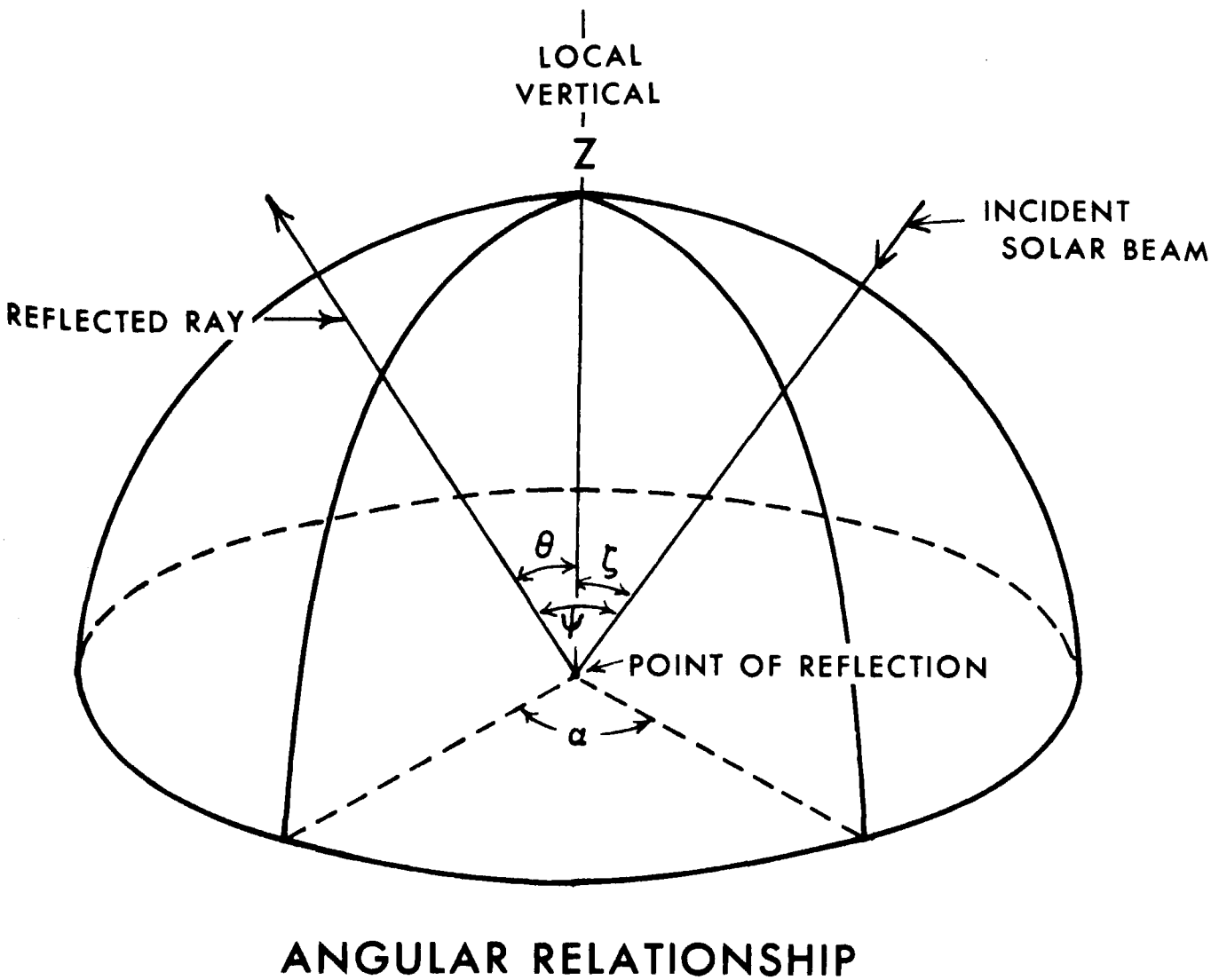

Figure 1. Diagram of upward-facing unit hemisphere, showing reflection geometry.

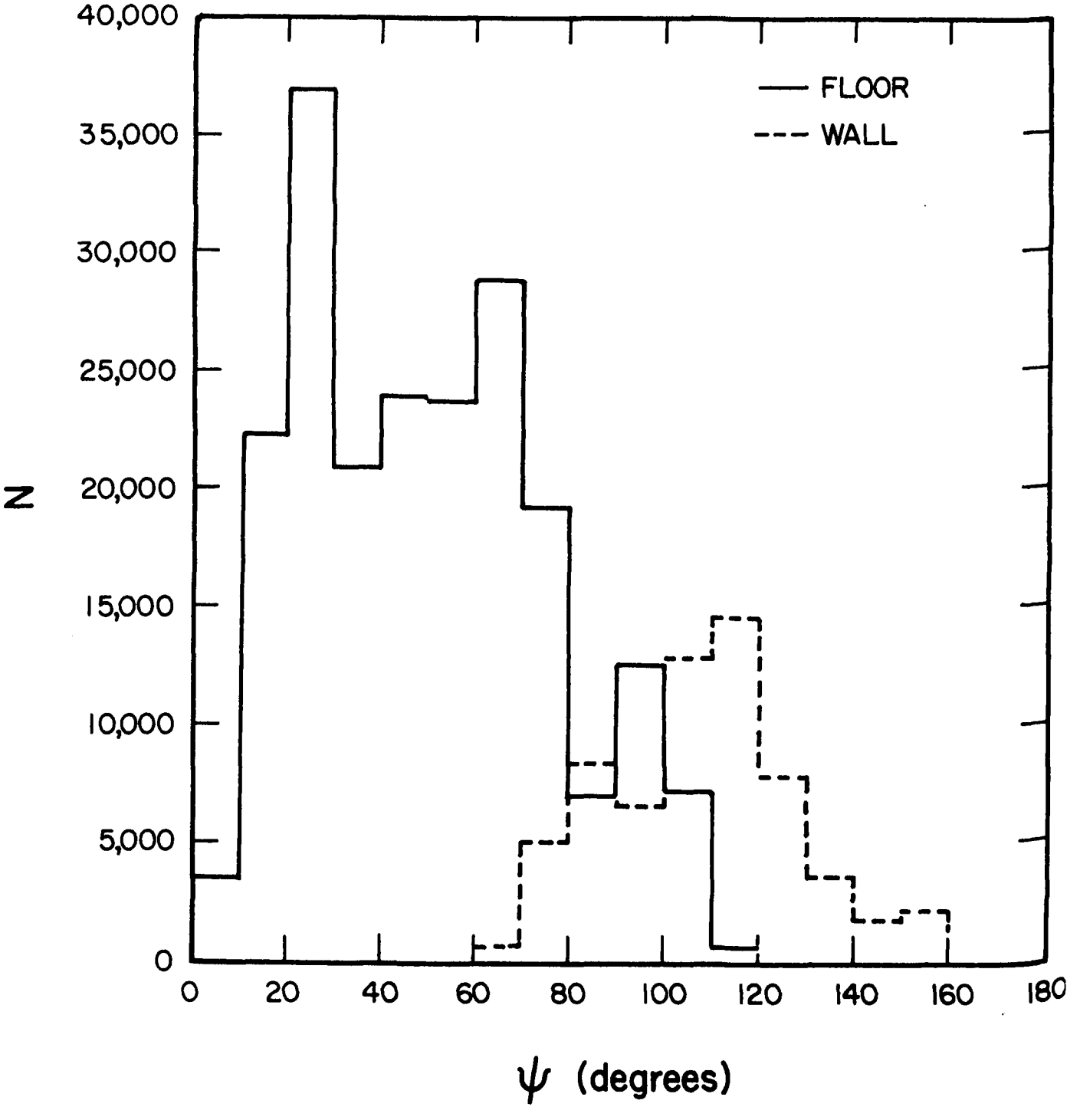

Figure 2. Histogram of the number of observations in the wall and floor directions of TIROS IV, channel 5 sensor during passes 127-612, (channel 2 equivalent blackbody temperature is less than 255°K.). Observations for all solar zenith angles are included.

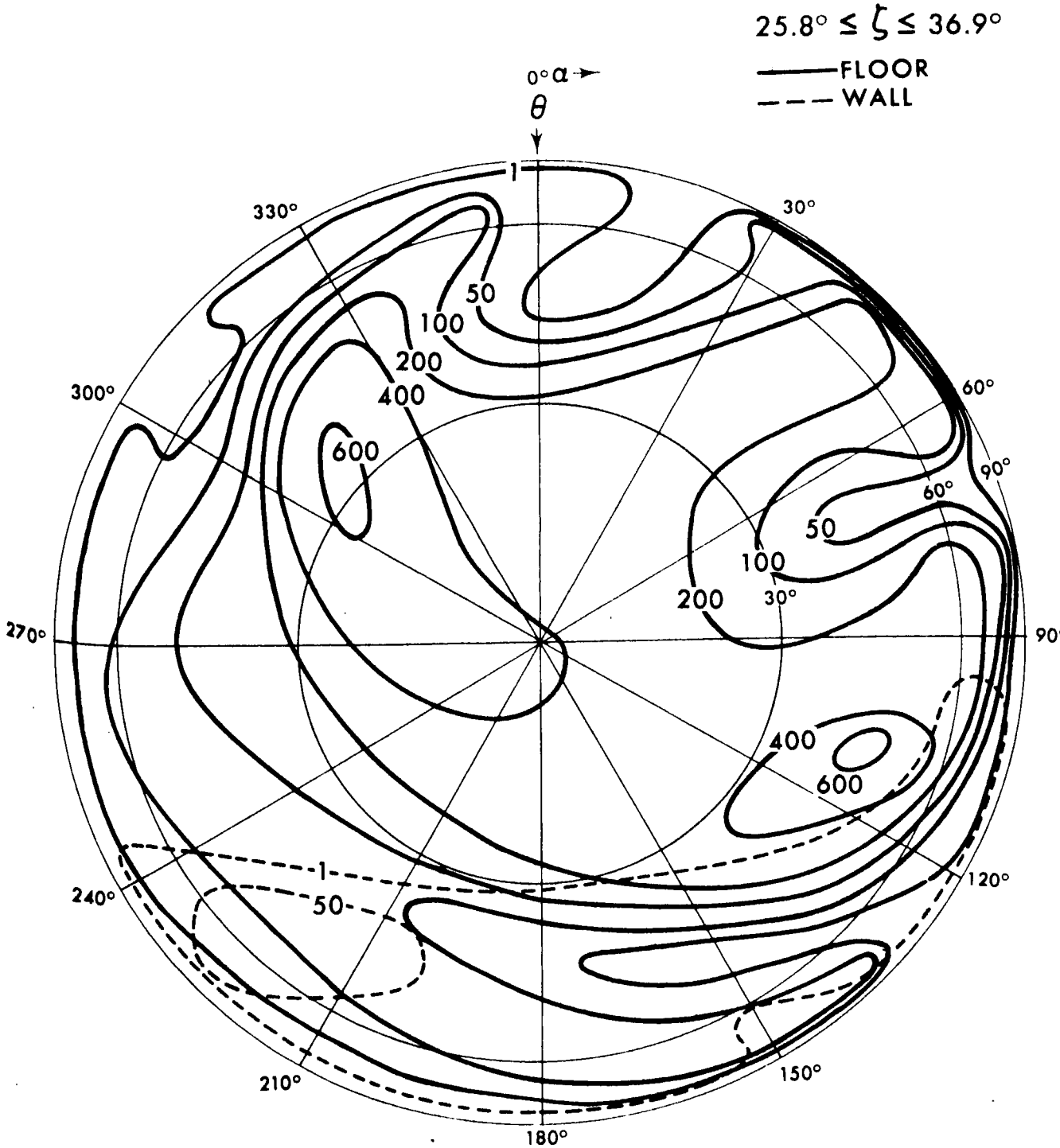

Figure 3. Map of upward-facing hemisphere showing number of observations in the wall and floor directions of the TIROS IV, channel 5 sensor during passes 127-612, when the channel 2 equivalent blackbody temperature is less than 255°K. The solar zenith angles are between 25°.8 and 36°.9.

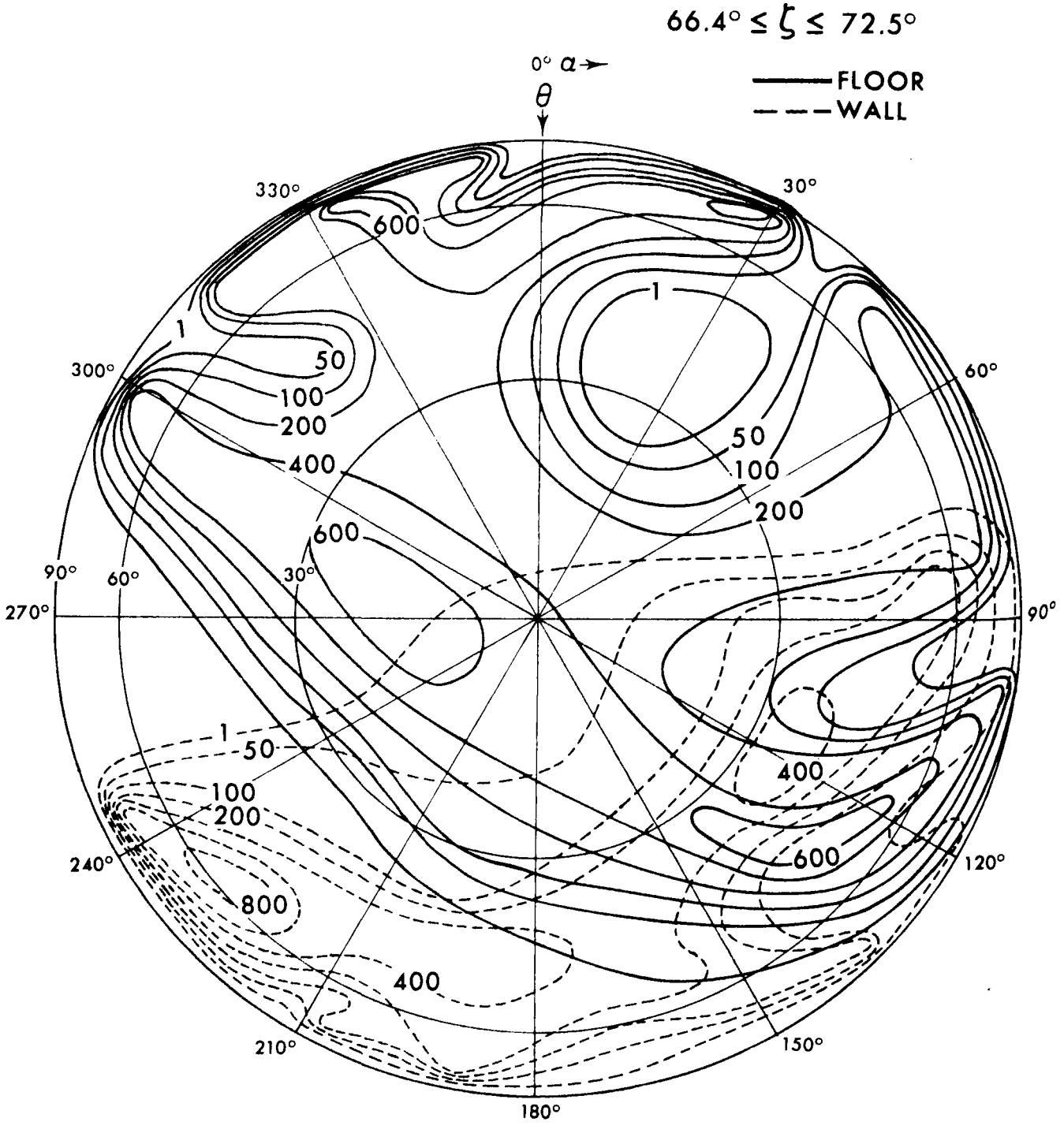

Figure 4. Same as figure 3 for solar zenith angle between 66°.4 and 72°.5.

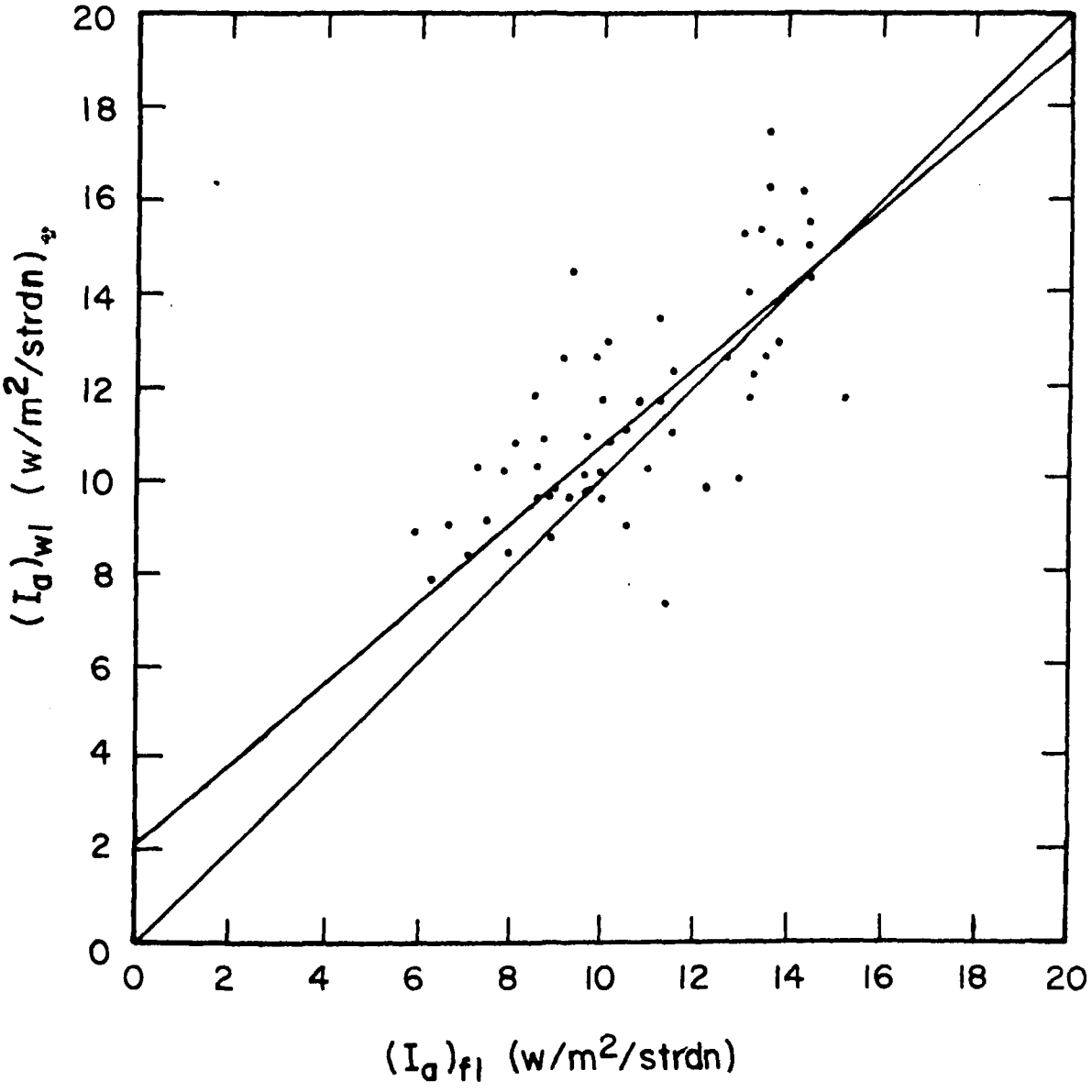

Figure 5. Scatter diagram of the filtered adjusted intensities in w.m.$^{-2}$ strdn.$^{-1}$, for TIROS IV, channel 5, at corresponding values of zenith angle, azimuth, and solar zenith angle for the wall direction during period 1 vs. floor direction in period 1. Approximate unfiltered adjusted intensities may be obtained by multiplying by 12.80. Observations include all solar zenith angles, when the channel 2 equivalent blackbody temperature is less than 255°K. Also plotted is the line of best least-square fit, and the line of equality of the two coordinates.

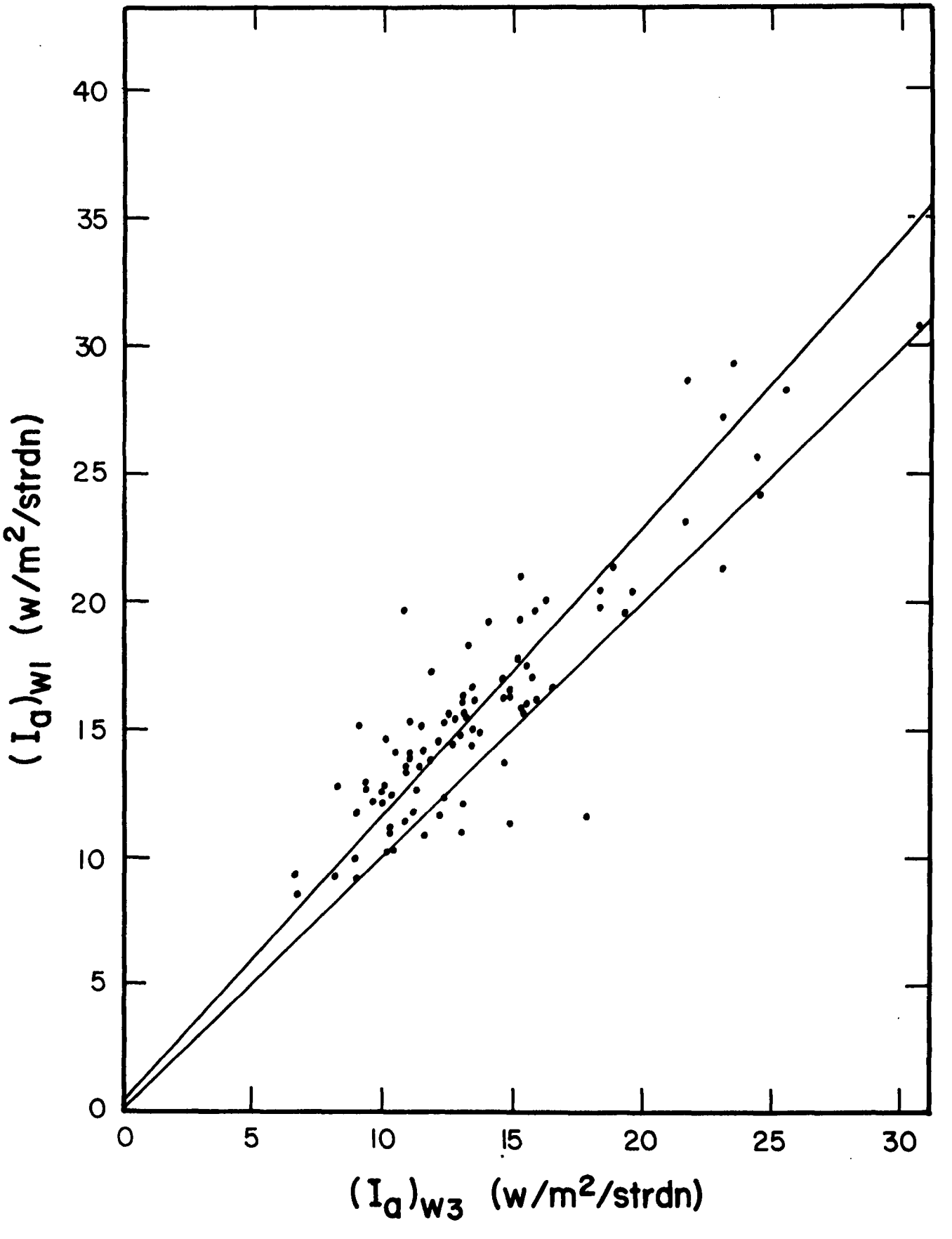
40
35
30
25
20
15
10
5
0
0
5
10
15
20
25
30
$(I_a)_{W1}$ (w/m²/strdn)
$(I_a)_{W3}$ (w/m²/strdn)

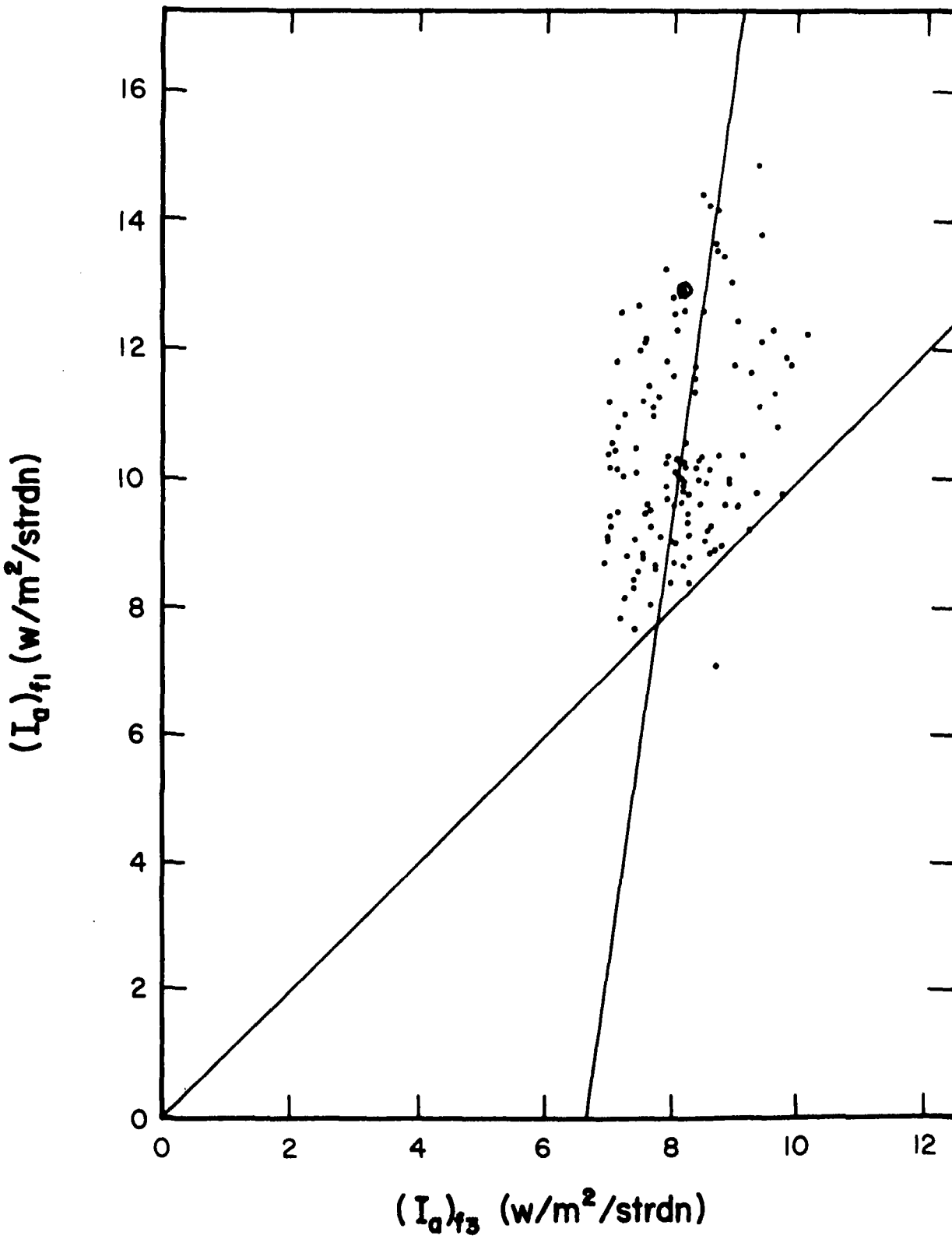

Figure 7. Same as figure 5, for floor direction in period 1 vs. floor direction in period 3.

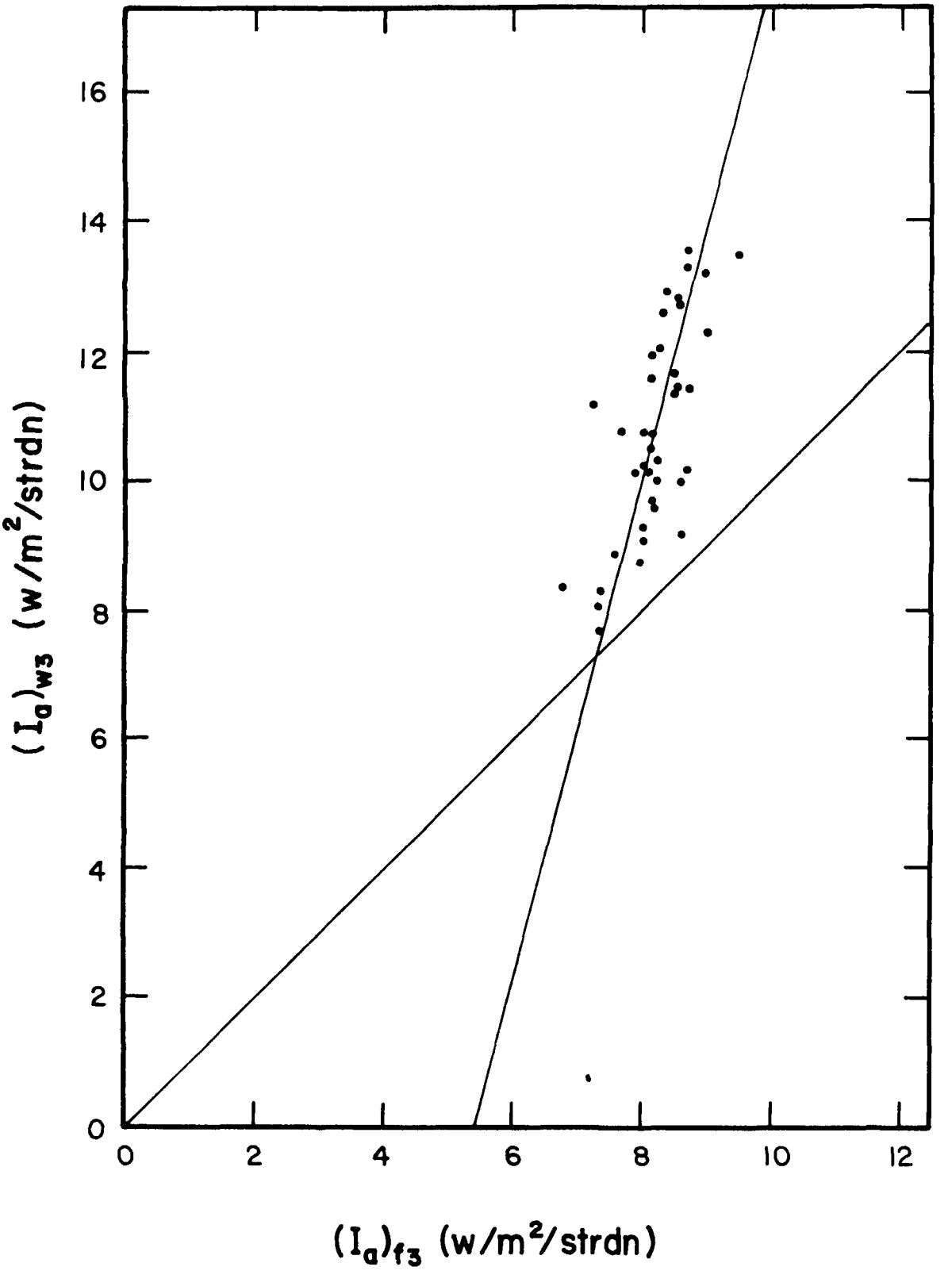

Figure 8. Same as figure 5, for wall direction in period 3 vs. floor direction in period 3.

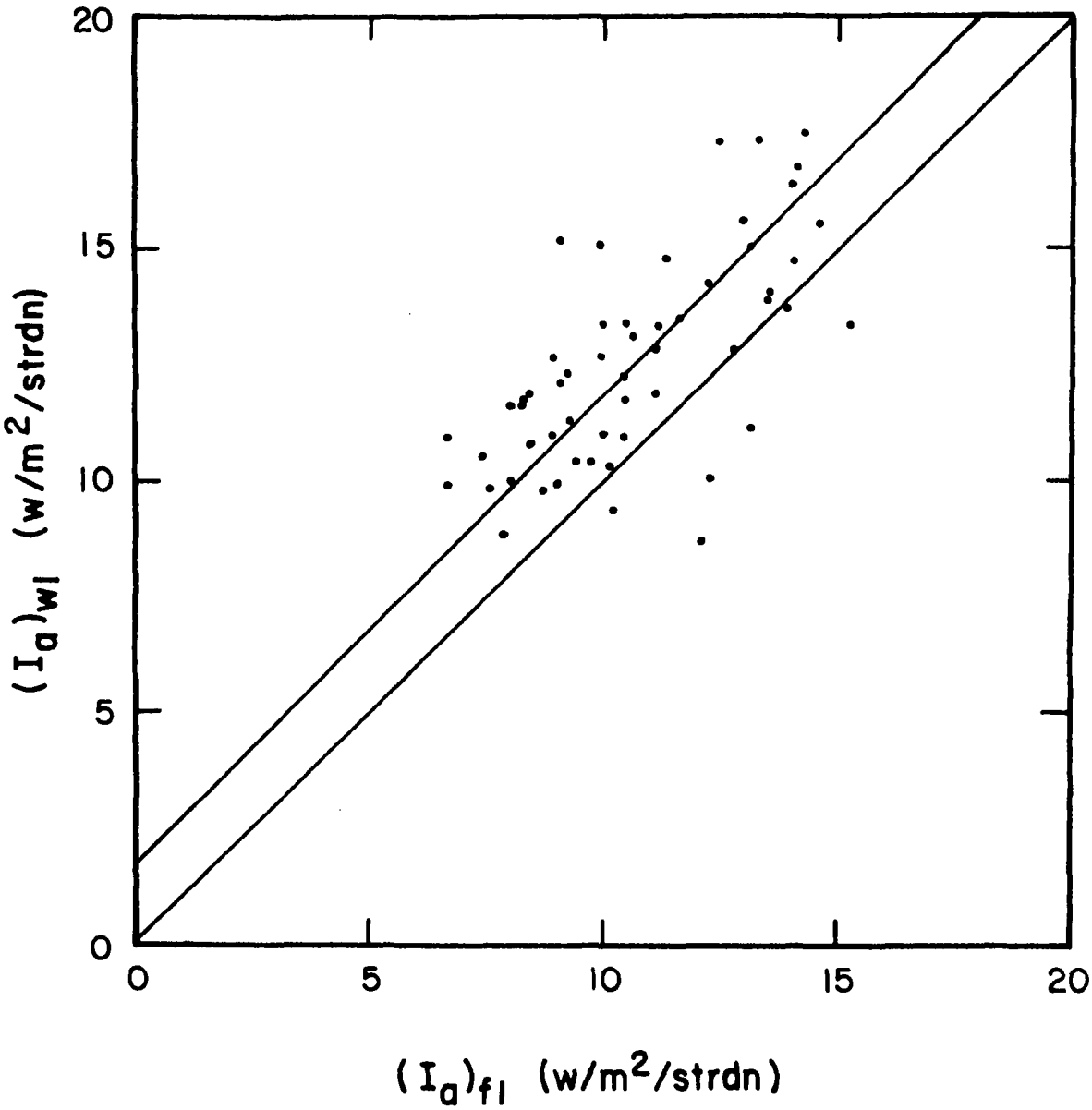

Figure 9. Scatter diagram of filtered adjusted intensities in w.m.$^{-2}$ strdn.$^{-1}$, for TIROS IV, channel 3, at corresponding values of zenith angle, azimuth, and solar zenith angle for the wall direction during period 1 vs. the floor direction in period 1. Approximate unfiltered adjusted intensities may be obtained by multiplying by 1.82. Observations include all solar zenith angles, when the channel 2 equivalent blackbody temperature is less than 255°K. Also plotted is the line of best least-square fit, and the line of equality of the two coordinates.

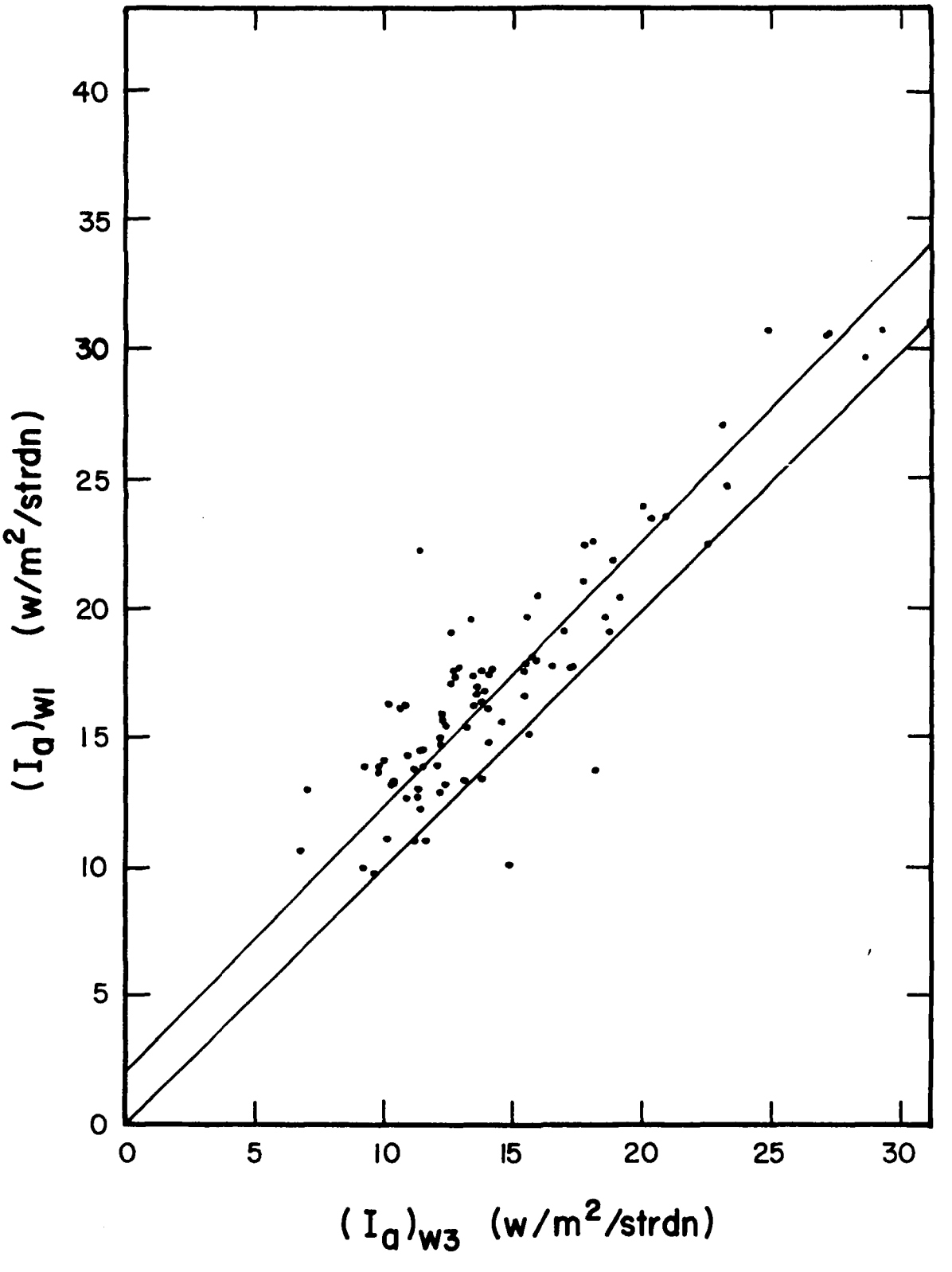

Figure 10. Same as figure 9, for wall direction in period 1 vs. wall direction in period 3.

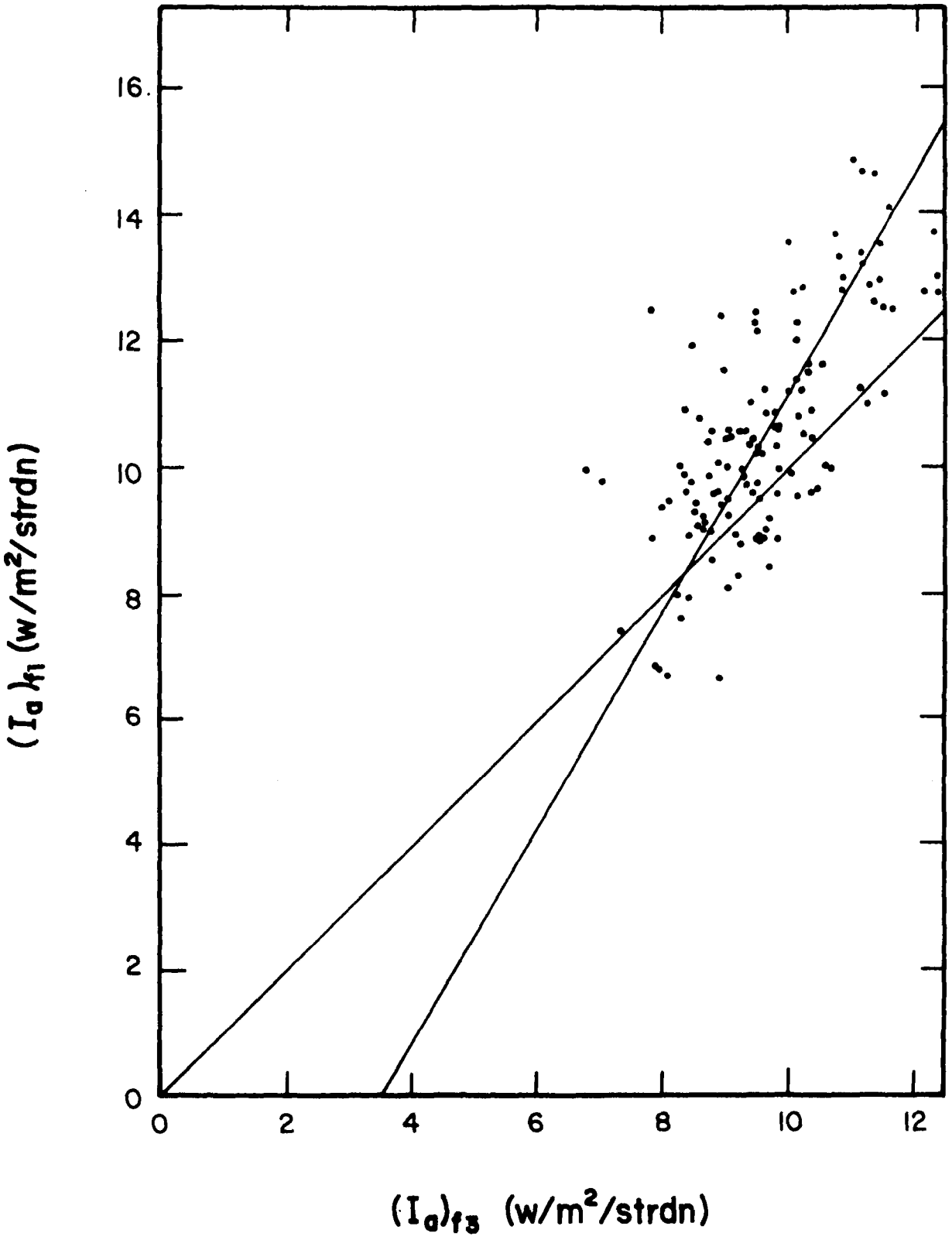

Figure 11. Same as figure 9, for floor direction in period 1 vs. floor direction in period 3.

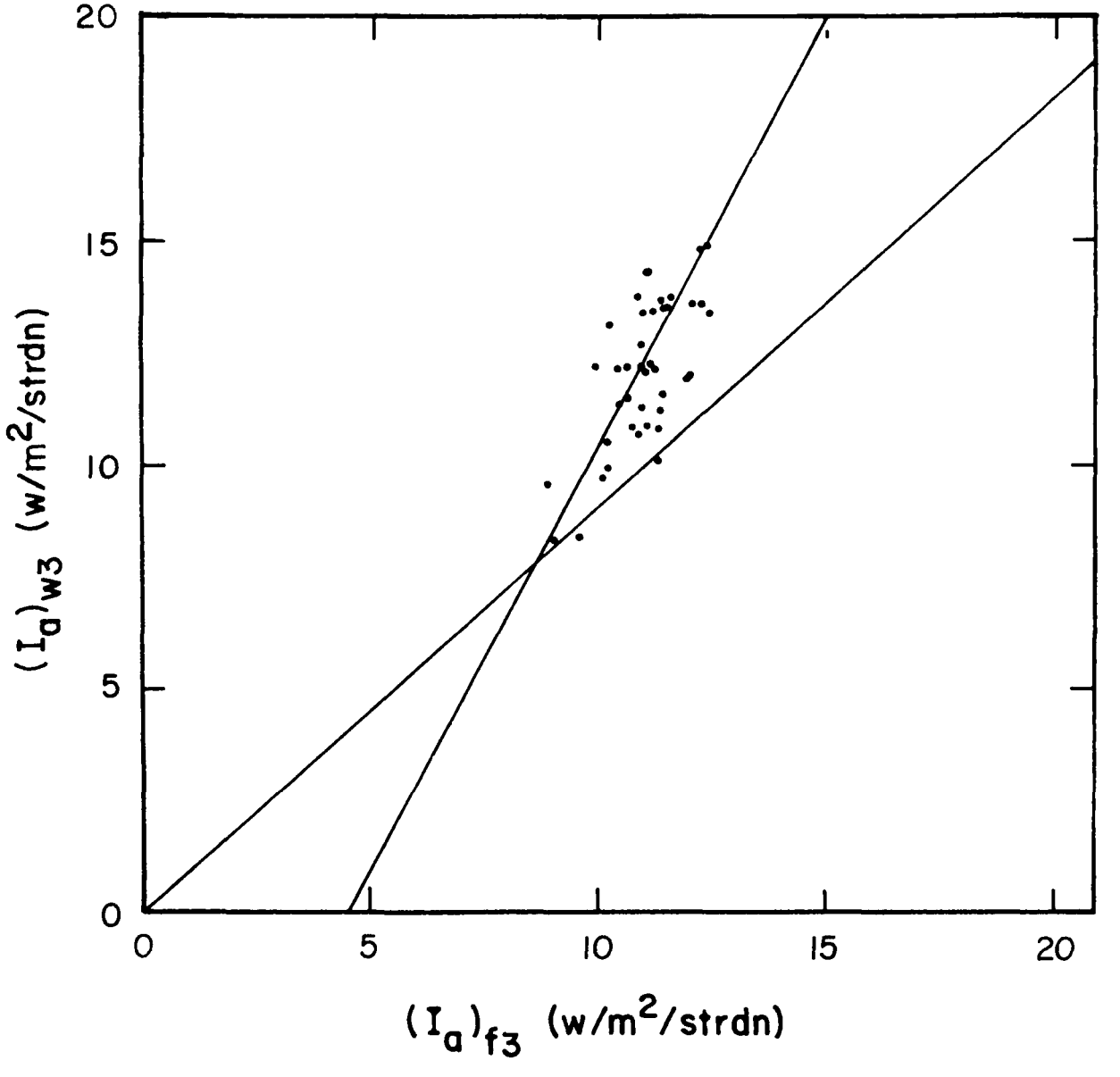

Figure 12. Same as figure 9, for wall direction in period 3 vs. floor direction in period 3.

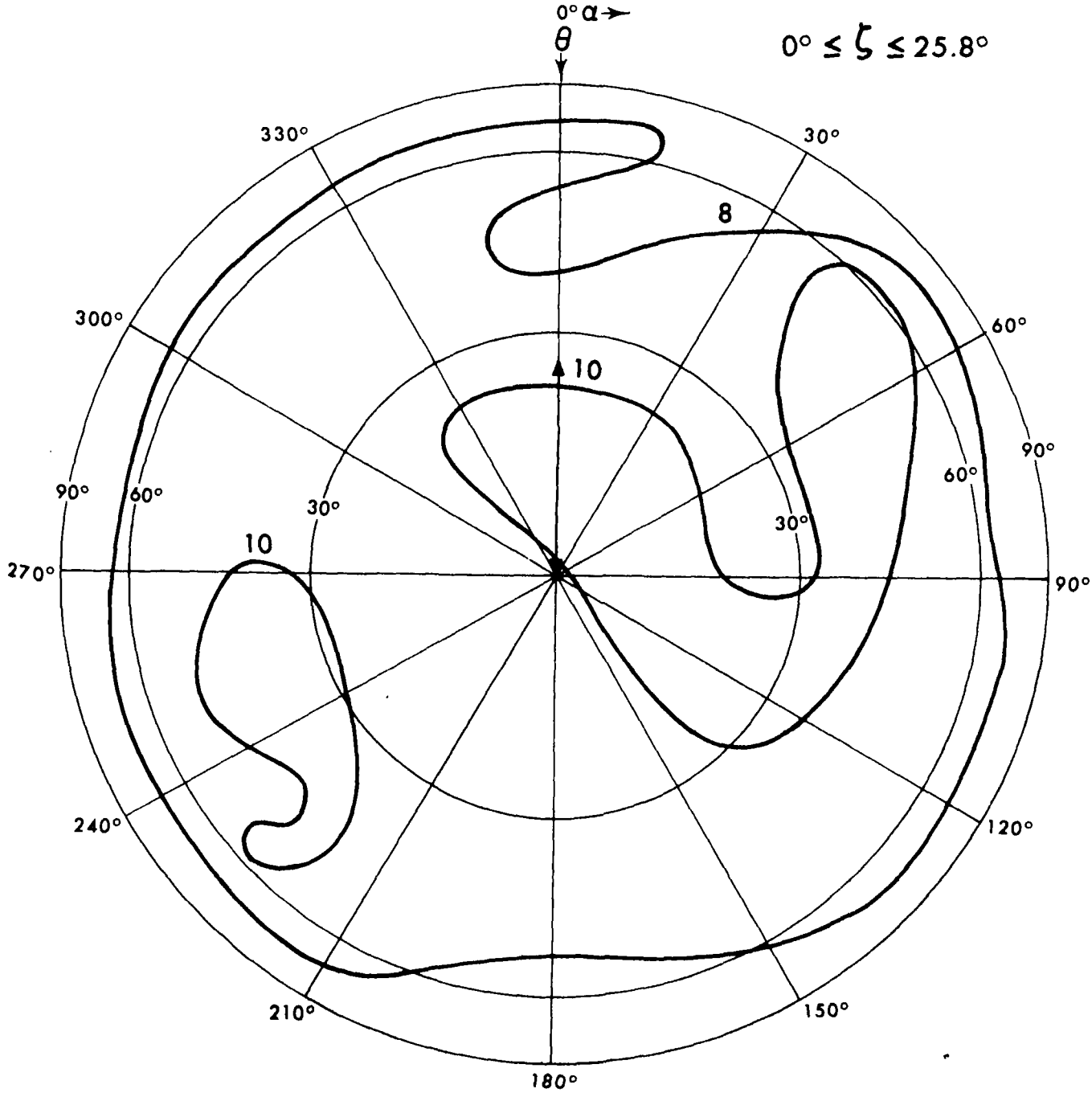

Figure 13. Distribution of reflected filtered adjusted intensities, in w.m.$^{-2}$ strdn.$^{-1}$, over the upward-facing hemisphere, for solar zenith angles between 0° and 25°.8. Double-headed arrow shows range of solar zenith angles. Approximate unfiltered adjusted intensities may be obtained by multiplying by 12.80.

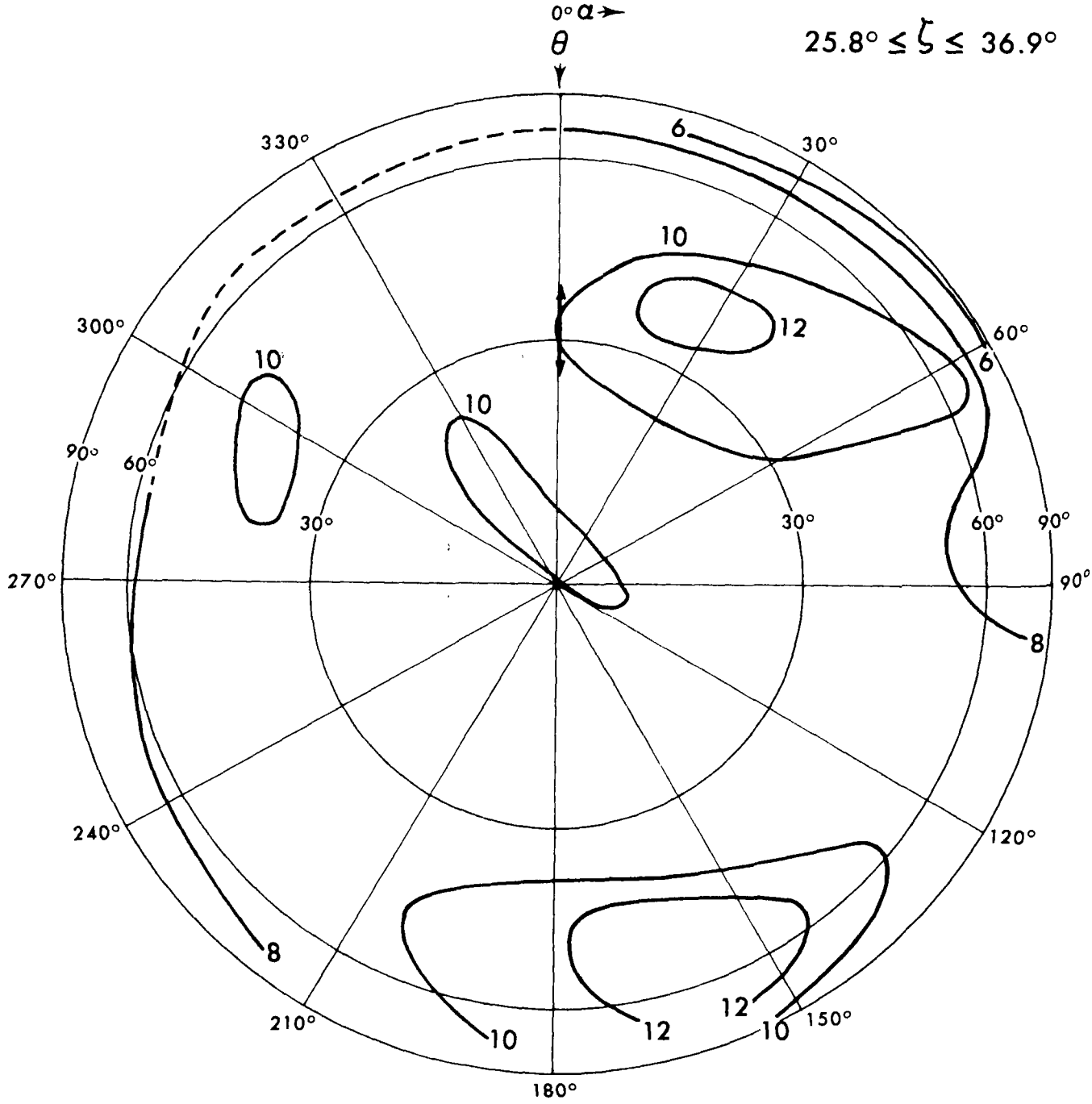

Figure 14. Same as Figure 13, for solar zenith angles between 25°.8 and 36°.9.

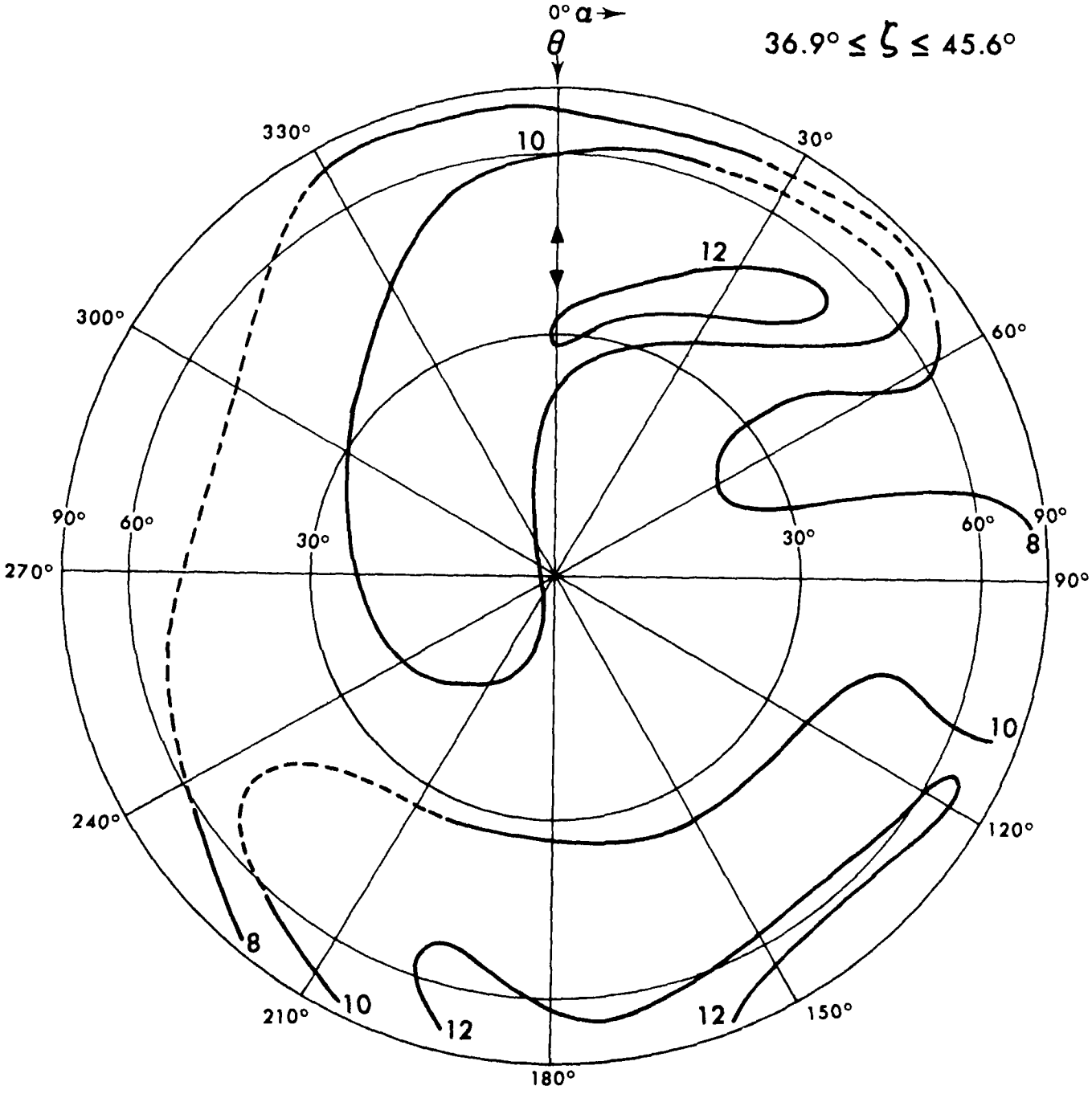

Figure 15. Same as figure 13, for solar zenith angles between 36°.9 and 45°.6.

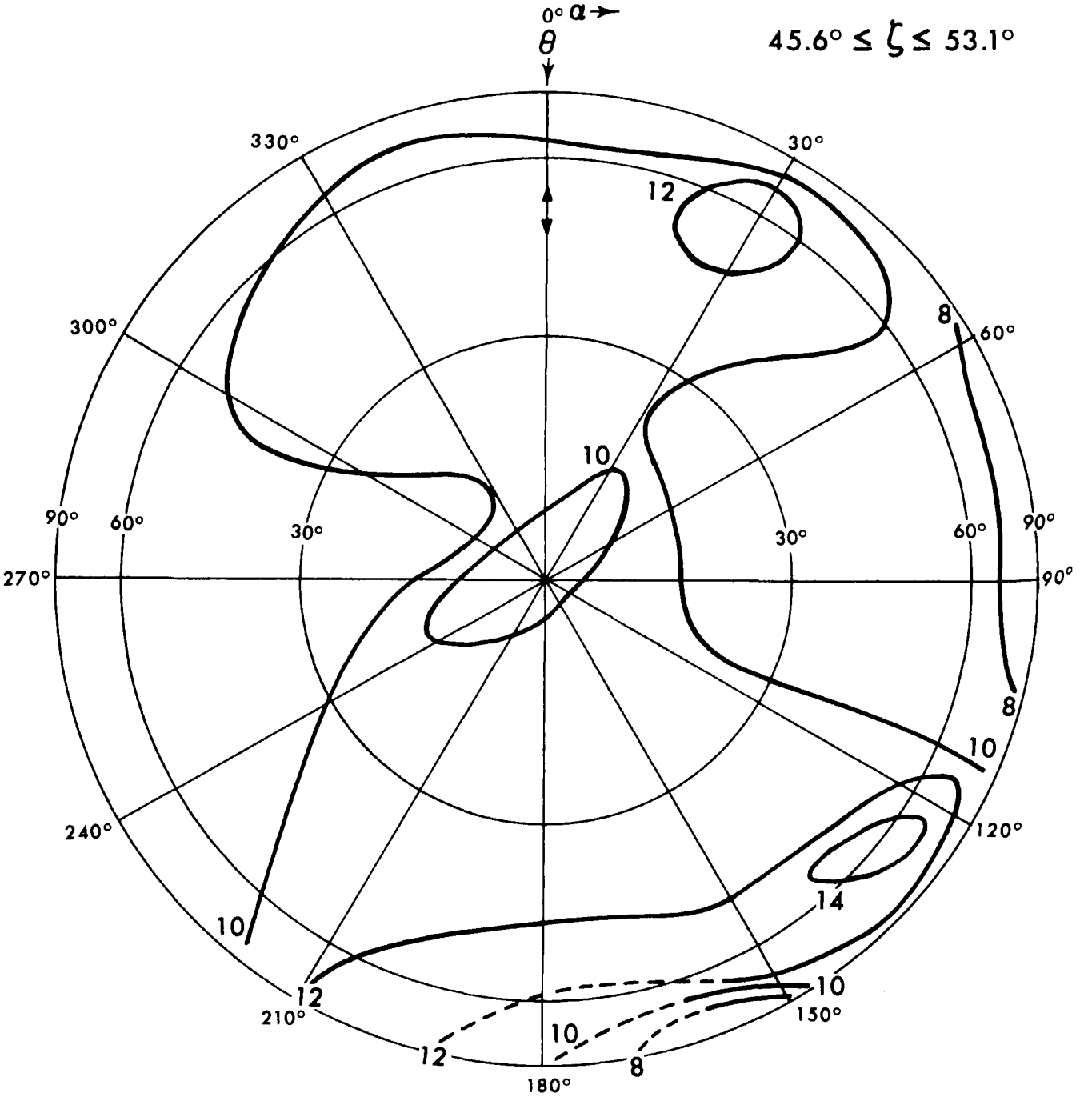

Figure 16. Same as figure 13, for solar zenith angles between 45°.6 and 53°.1.

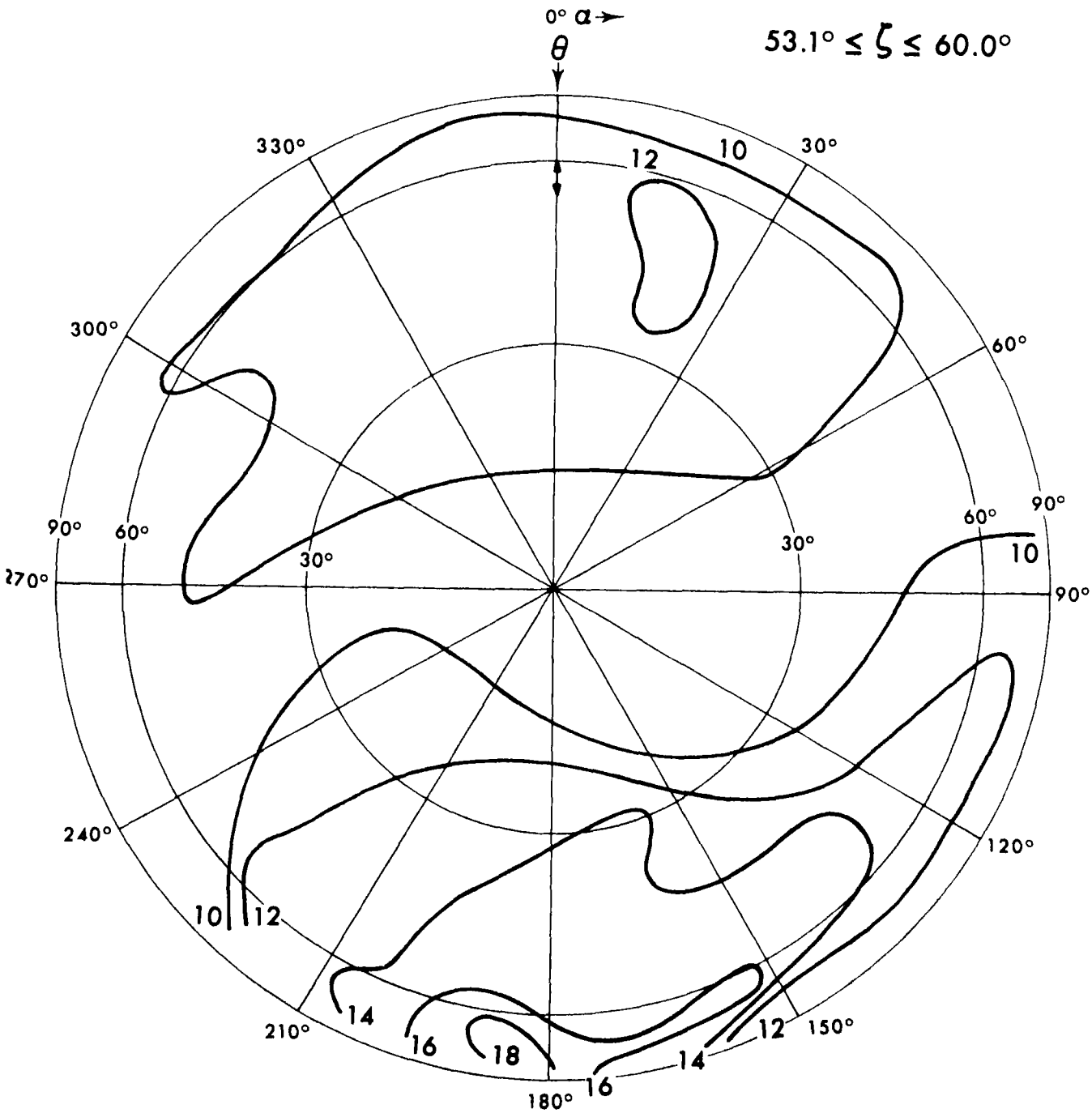

Figure 17. Same as figure 13, for solar zenith angles between 53°.1 and 60°.0.

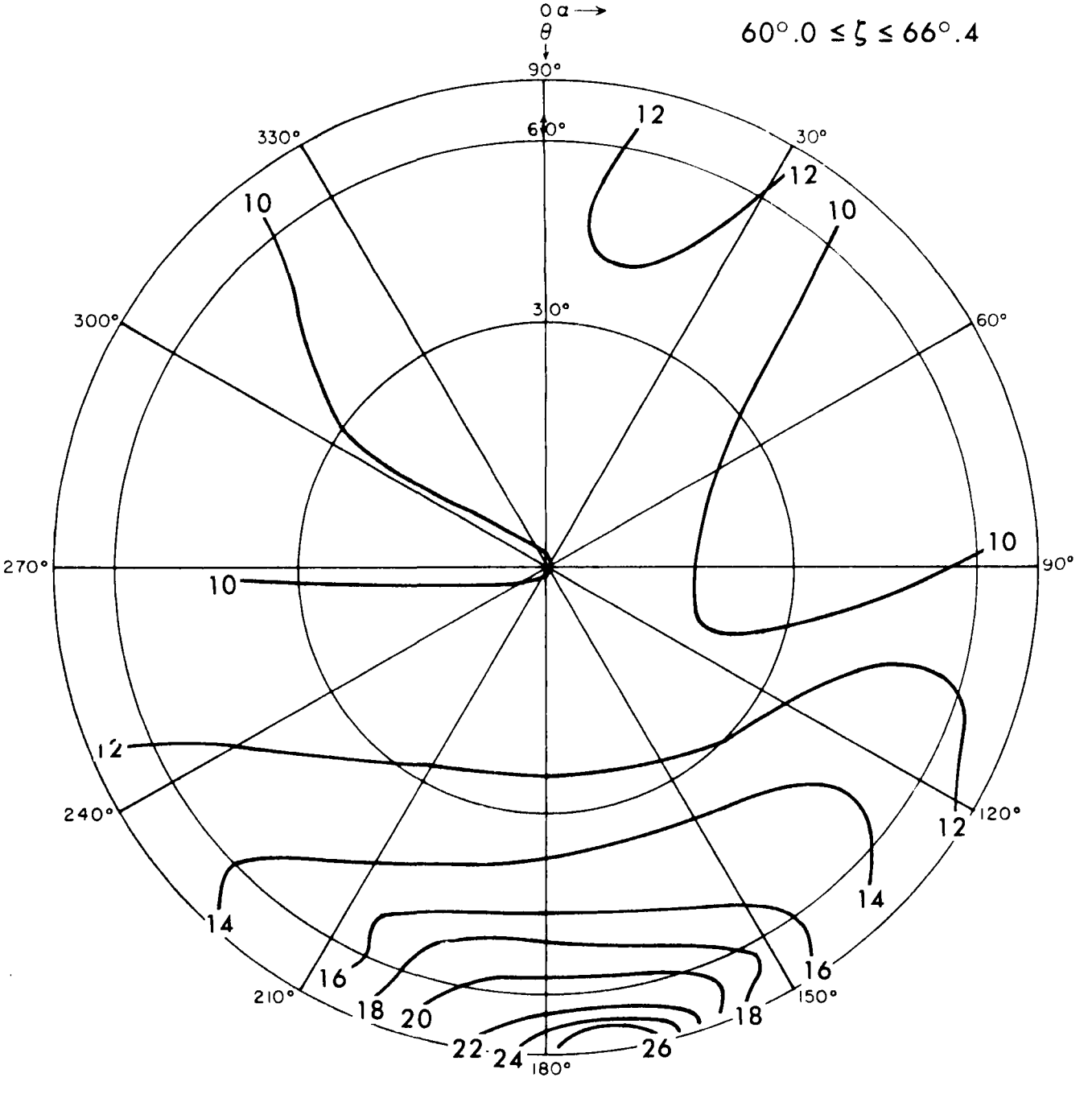

Figure 18. Same as figure 13, for solar zenith angles between 60°.0 and 66°.4.

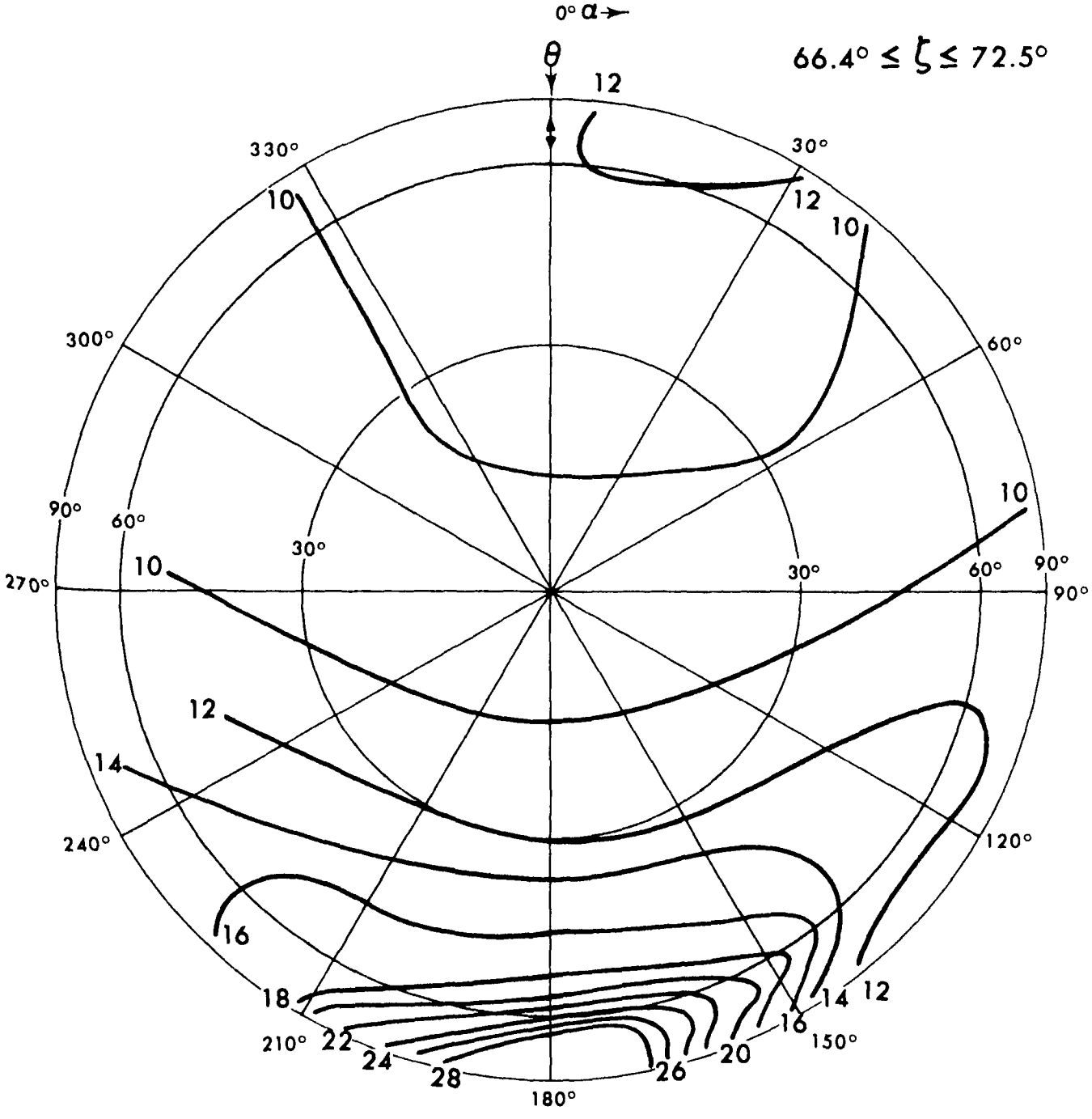

Figure 19. Same as figure 13, for solar zenith angles between 66°.4 and 72°.5.

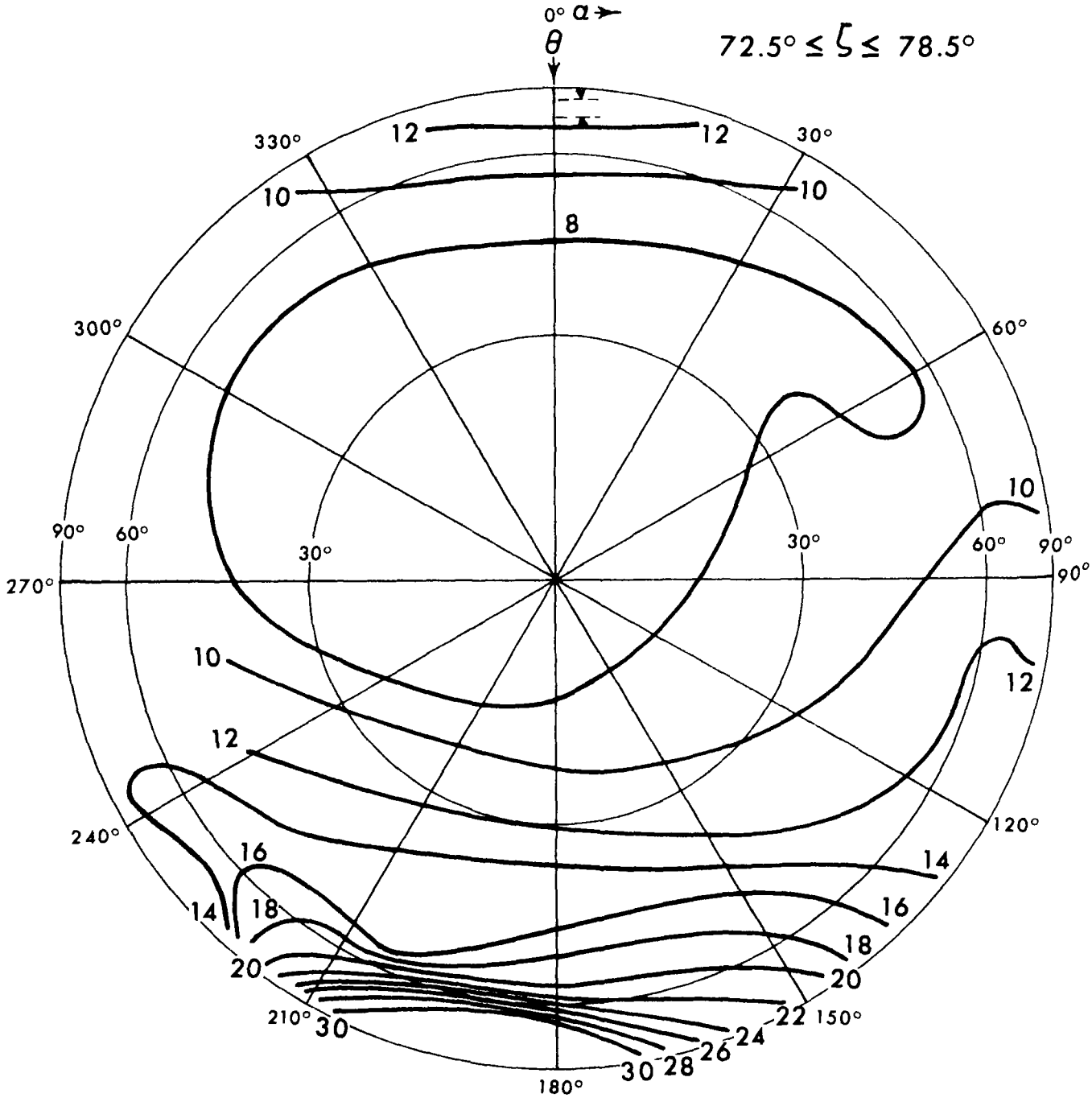

Figure 20. Same as figure 13, for solar zenith angles between 72°.5 and 78°.5.

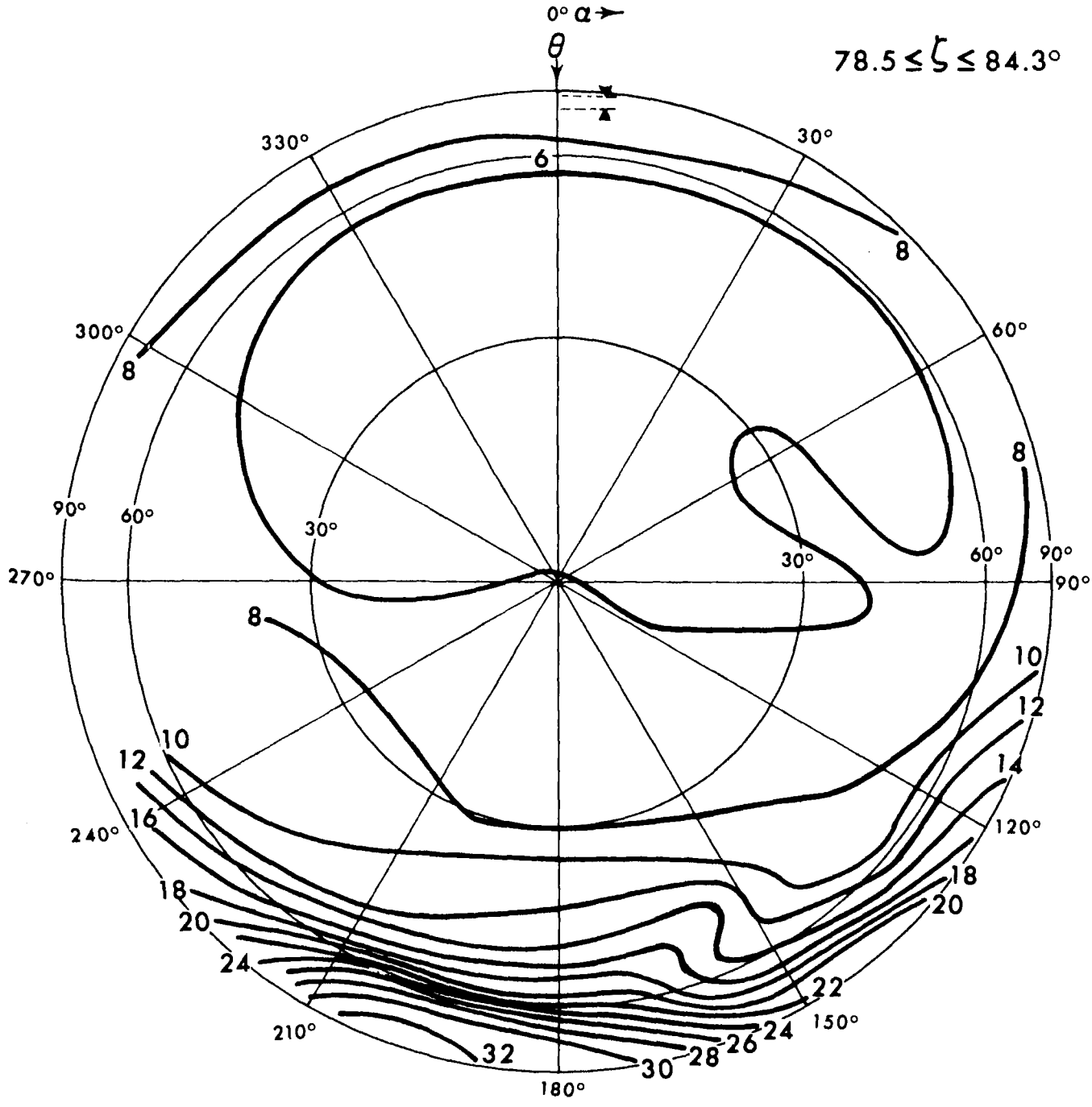

Figure 21. Same as figure 13, for solar zenith angles between 78°.5 and 84°.3.

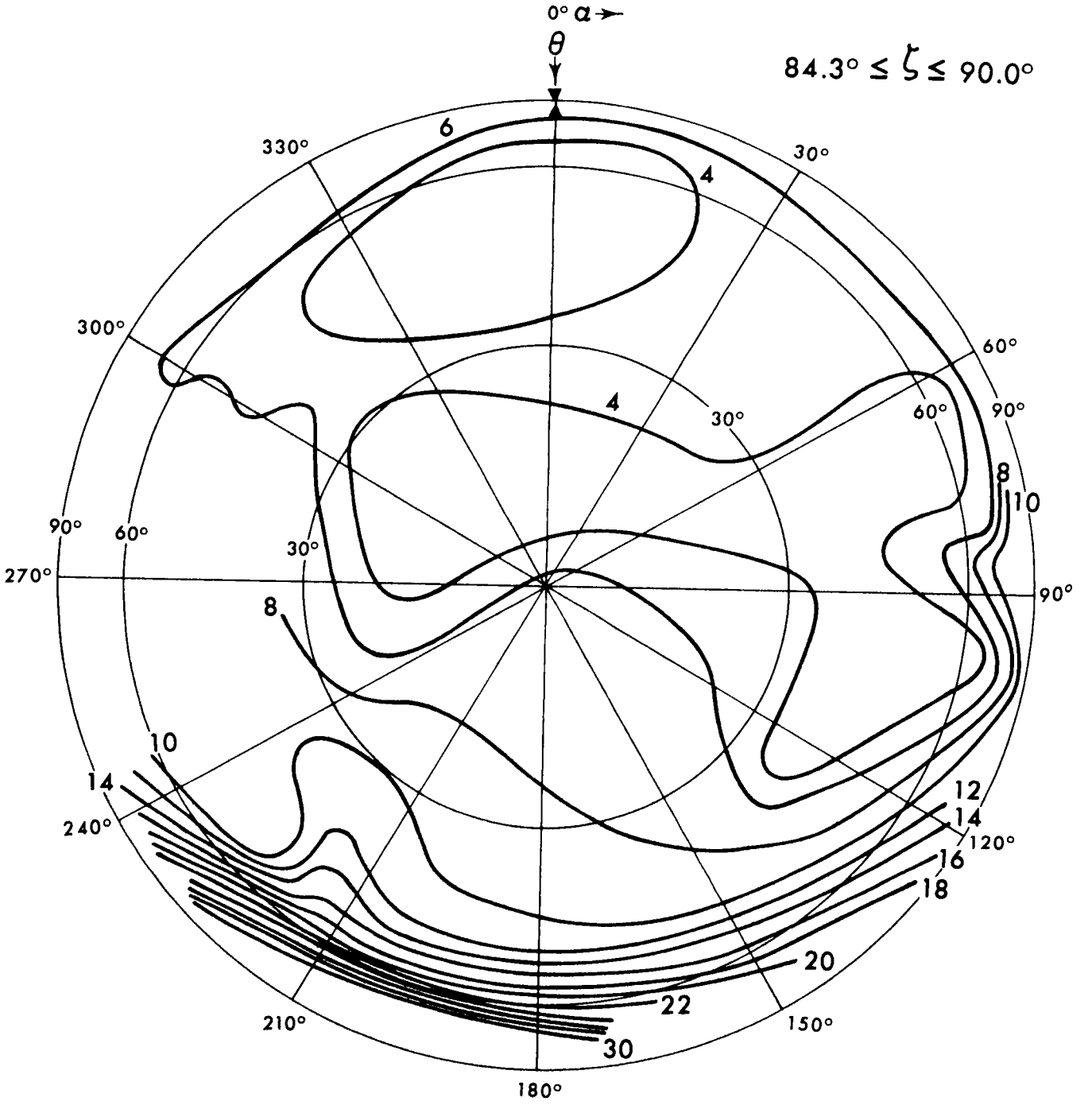

Figure 22. Same as figure 13, for solar zenith angles between 84°.3 and 90°.0.

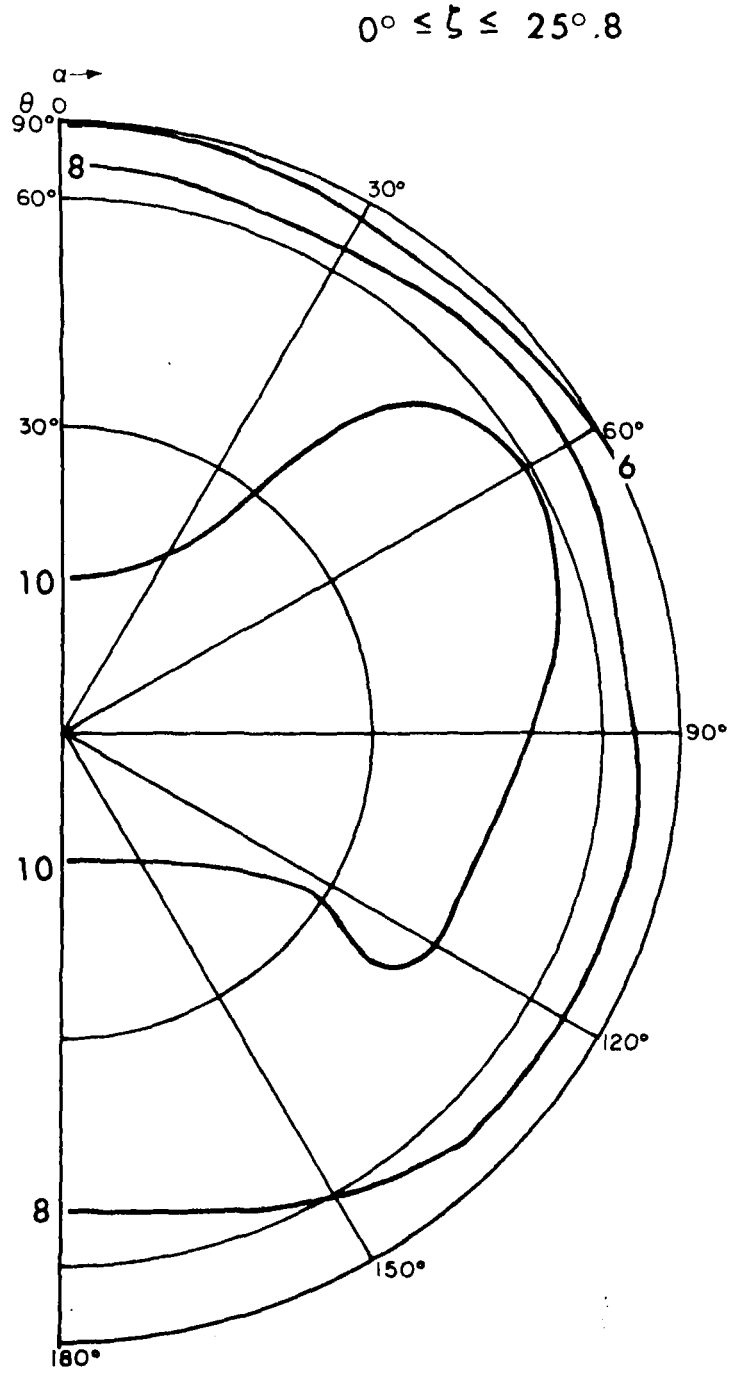

Figure 23. Symmetrized and smoothed distribution of reflected filtered adjusted intensities, in w.m.$^{-2}$ strdn.$^{-1}$, over the upward-facing hemisphere, for solar zenith angles between 0° and 25°.8. Double-headed arrows show range of solar zenith angles. Approximate unfiltered adjusted intensities may be obtained by multiplying by 12.80.

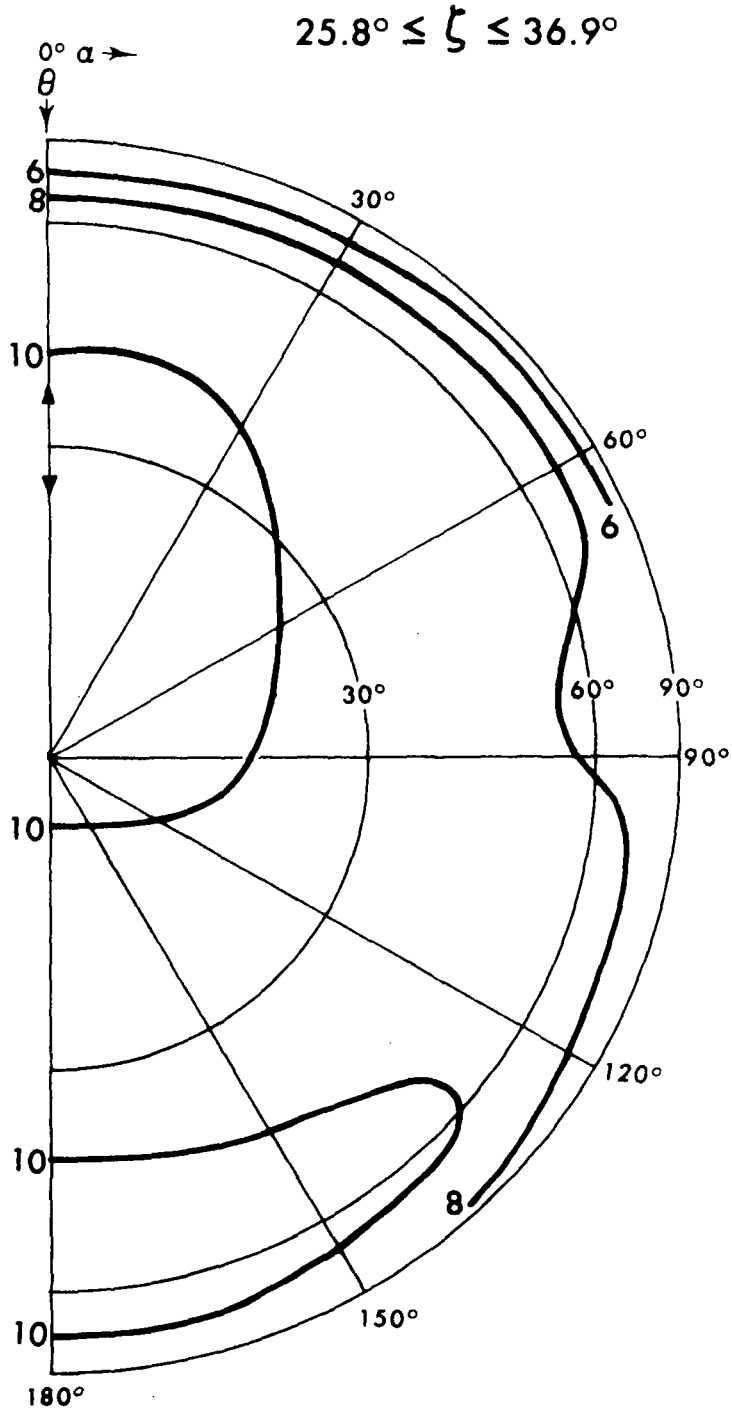

Figure 24. Same as figure 23, for solar zenith angles between 25°.8 and 36°.9.

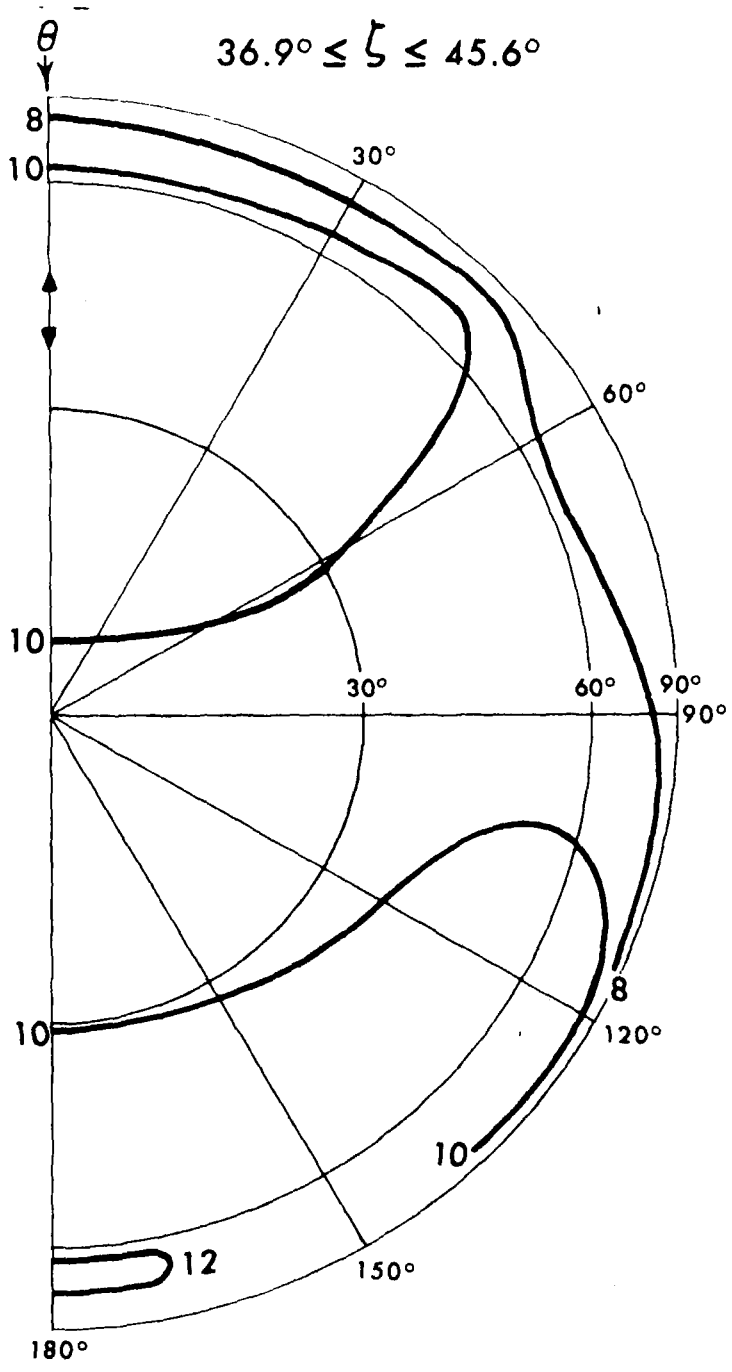

Figure 25. Same as figure 23, for solar zenith angles between 36°.9 and 45°.6.

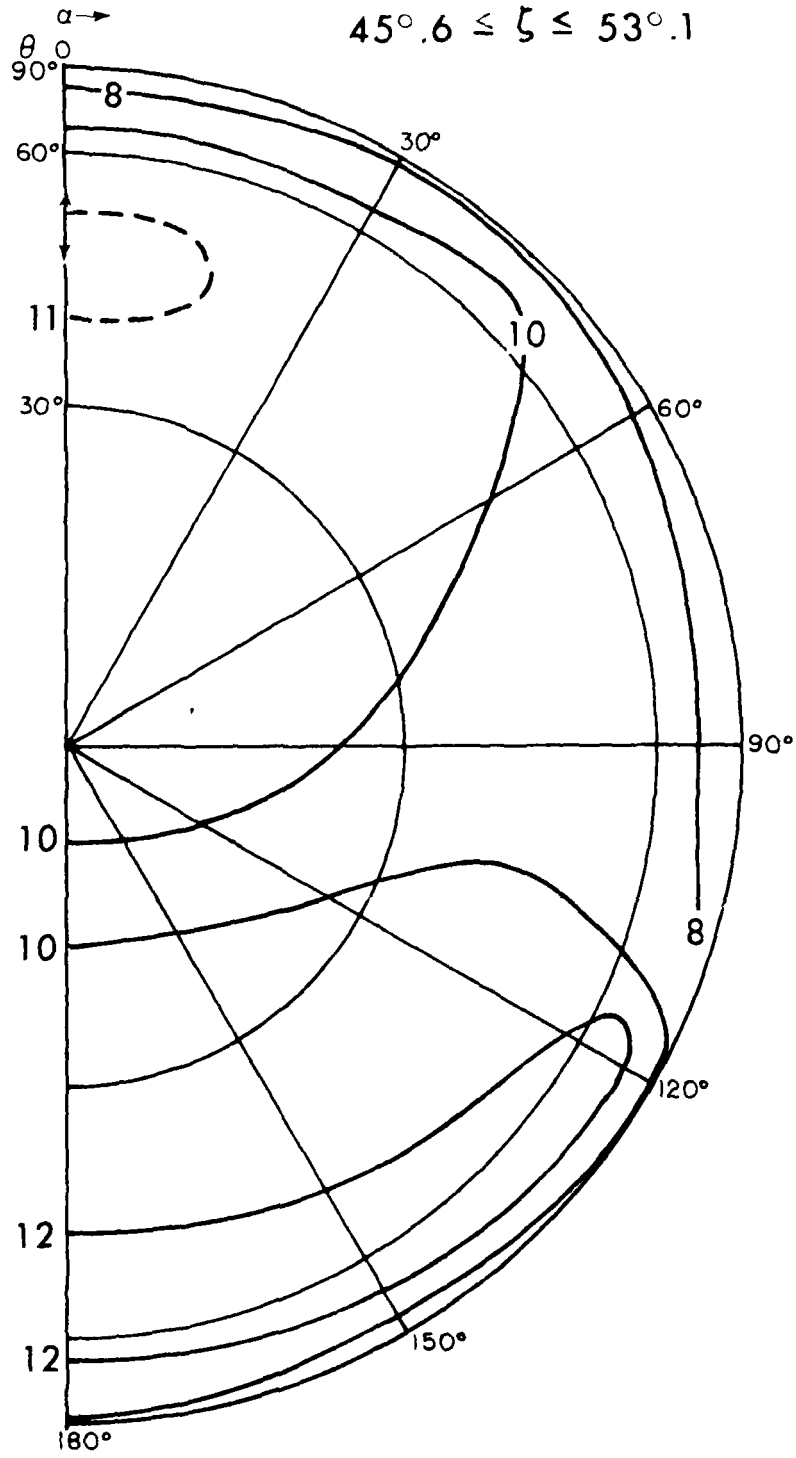

Figure 26. Same as figure 23, for solar zenith angles between 45°.6 and 53°.1.

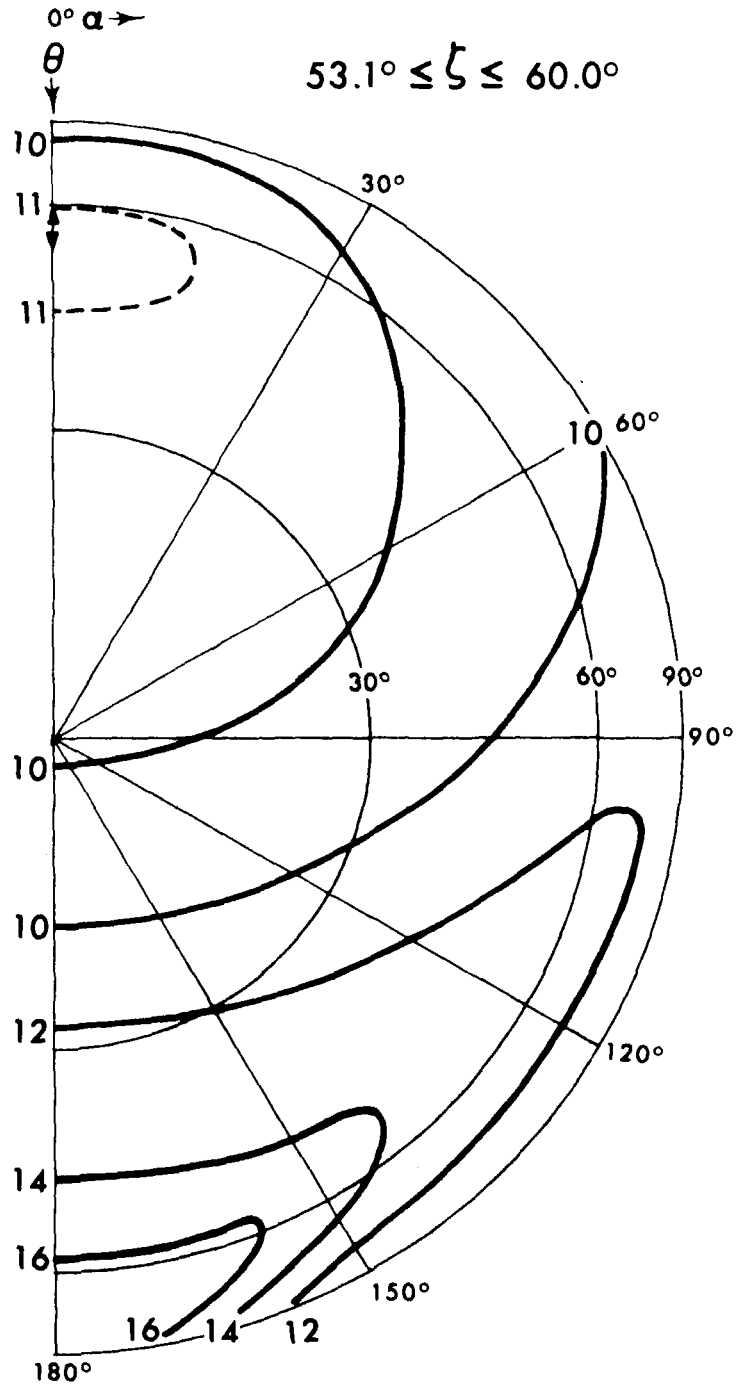

Figure 27. Same as figure 23, for solar zenith angles between 53°.1 and 60°.0.

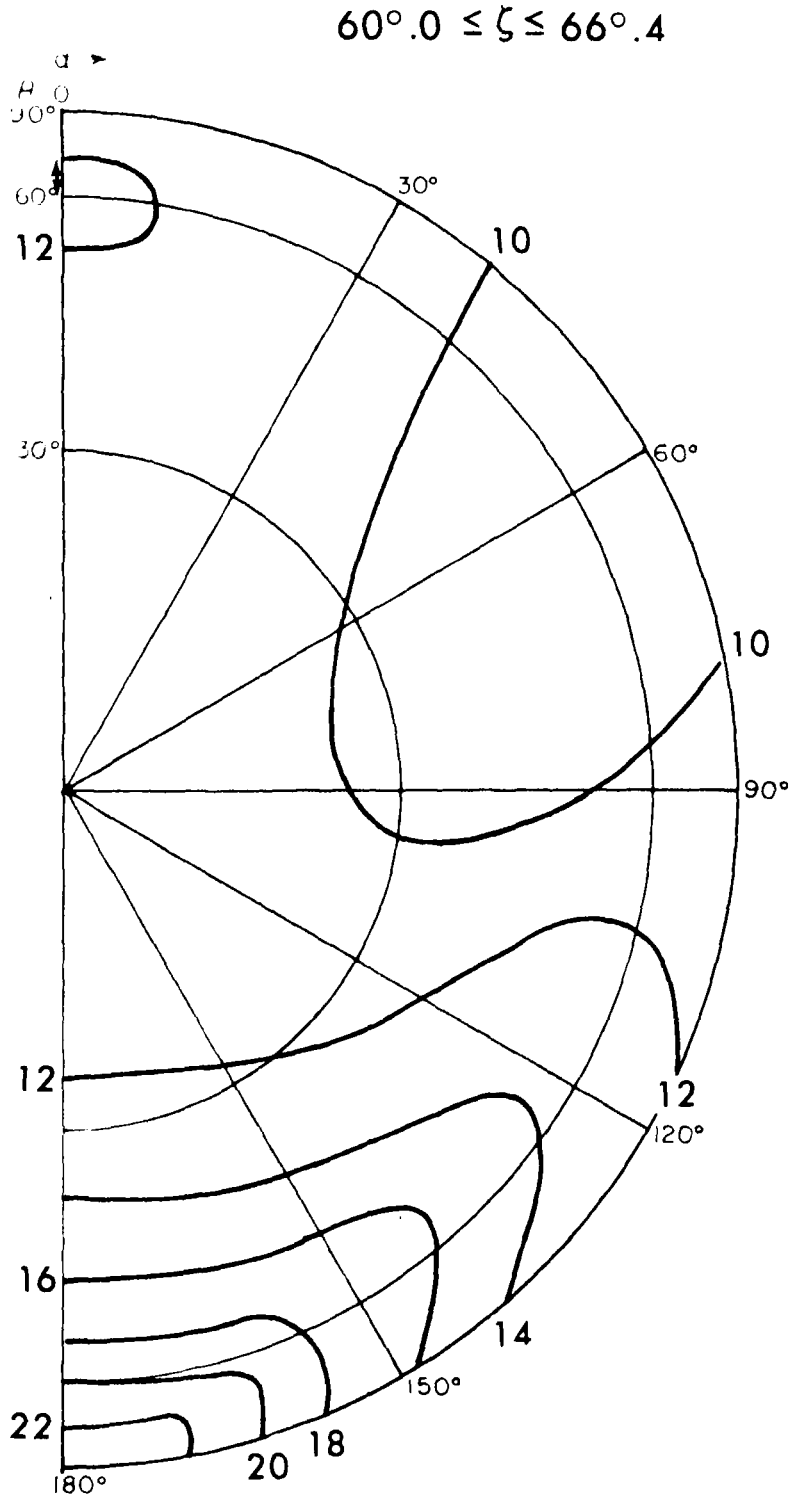

Figure 28. Same as figure 23, for solar zenith angles between 60°.0 and 66°.4.

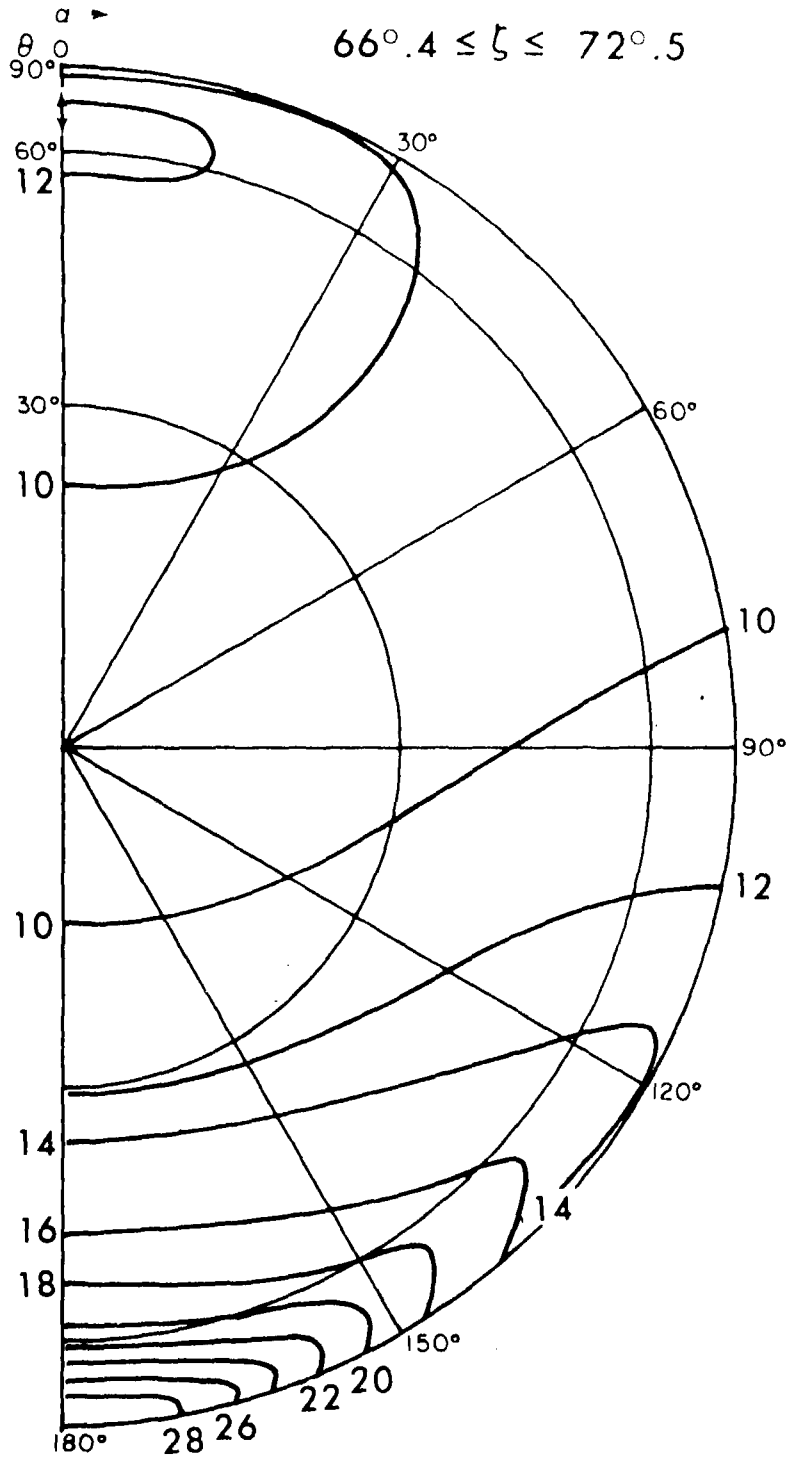

Figure 29. Same as figure 23, for solar zenith angles between 66°.4 and 72°.5.

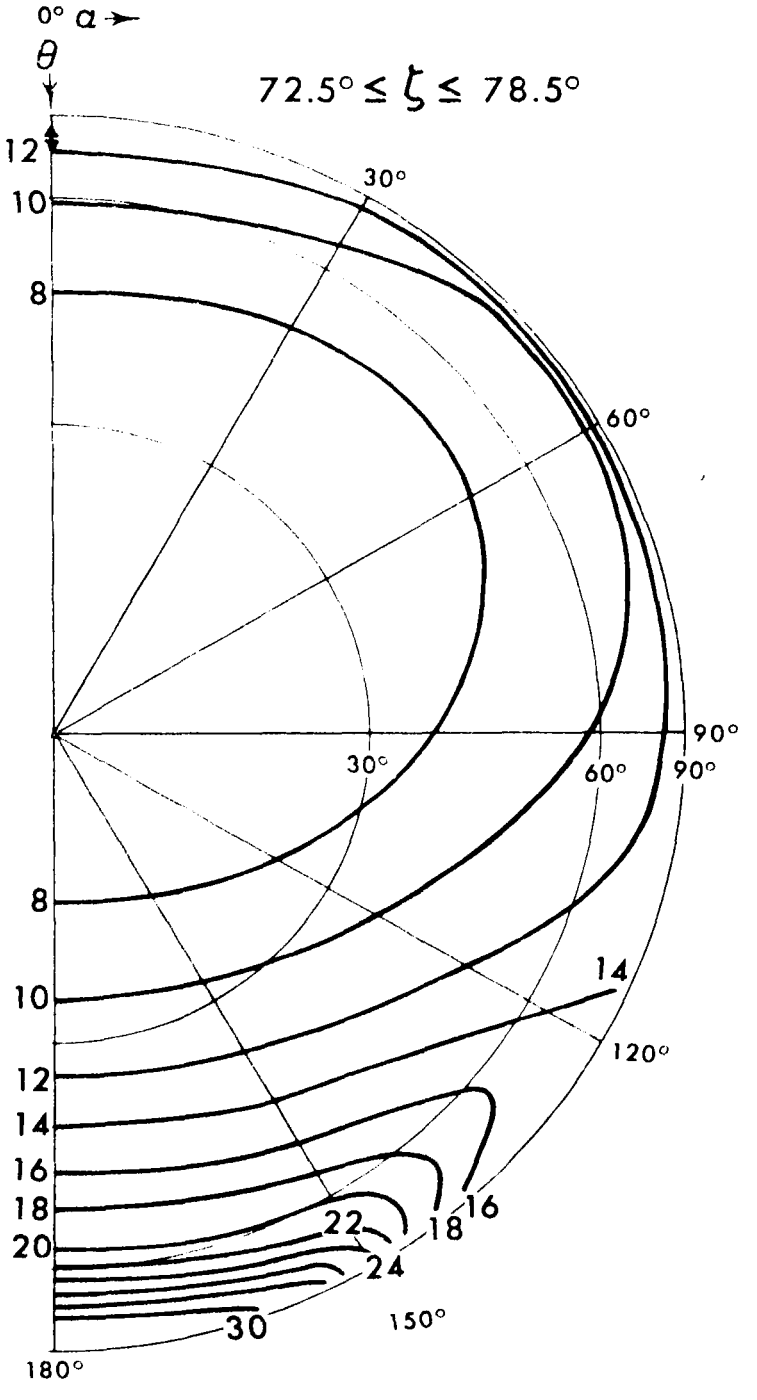

Figure 30. Same as figure 23, for solar zenith angles between 72°.5 and 78°.5.

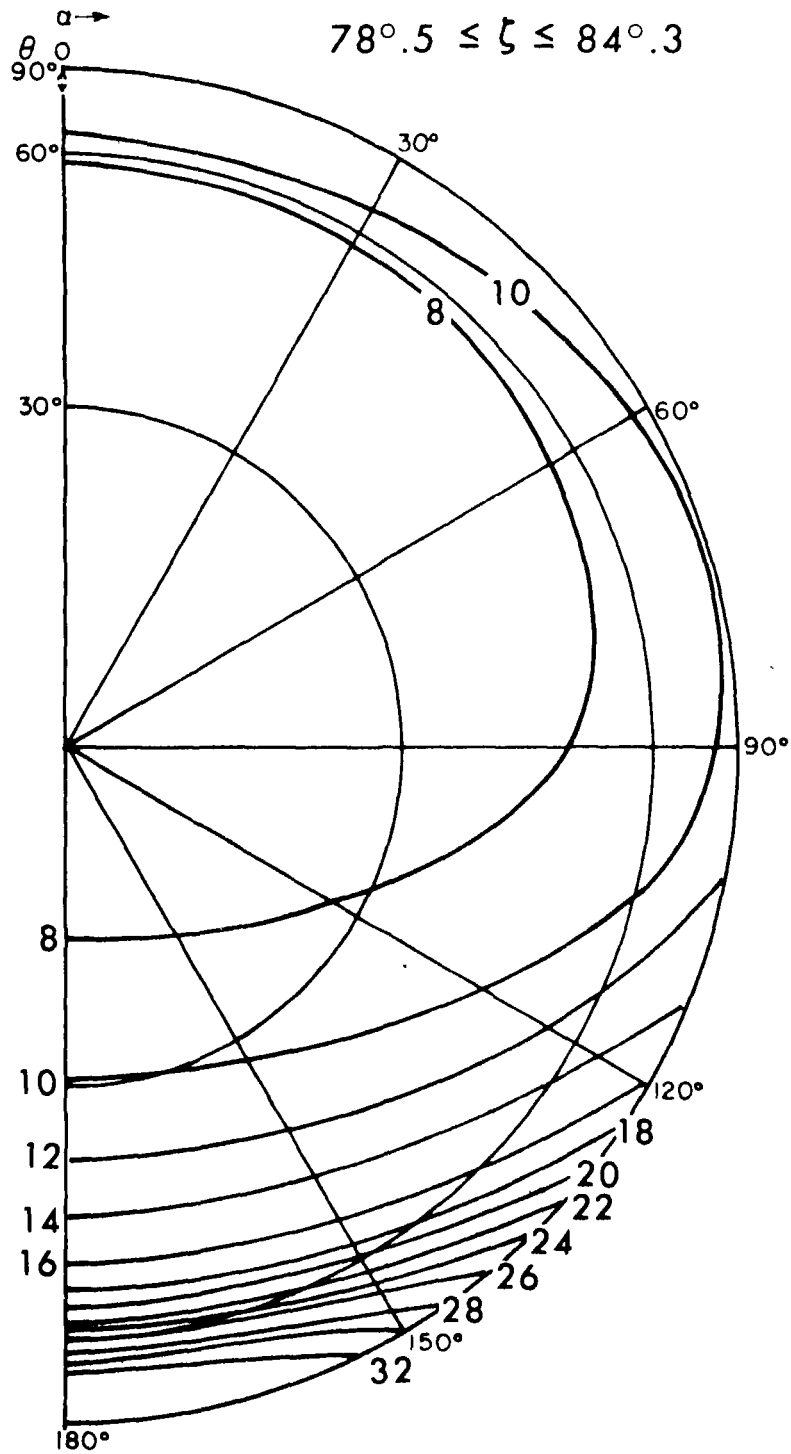

Figure 31. Same as figure 23, for solar zenith angles between 78°.5 and 84°.3.

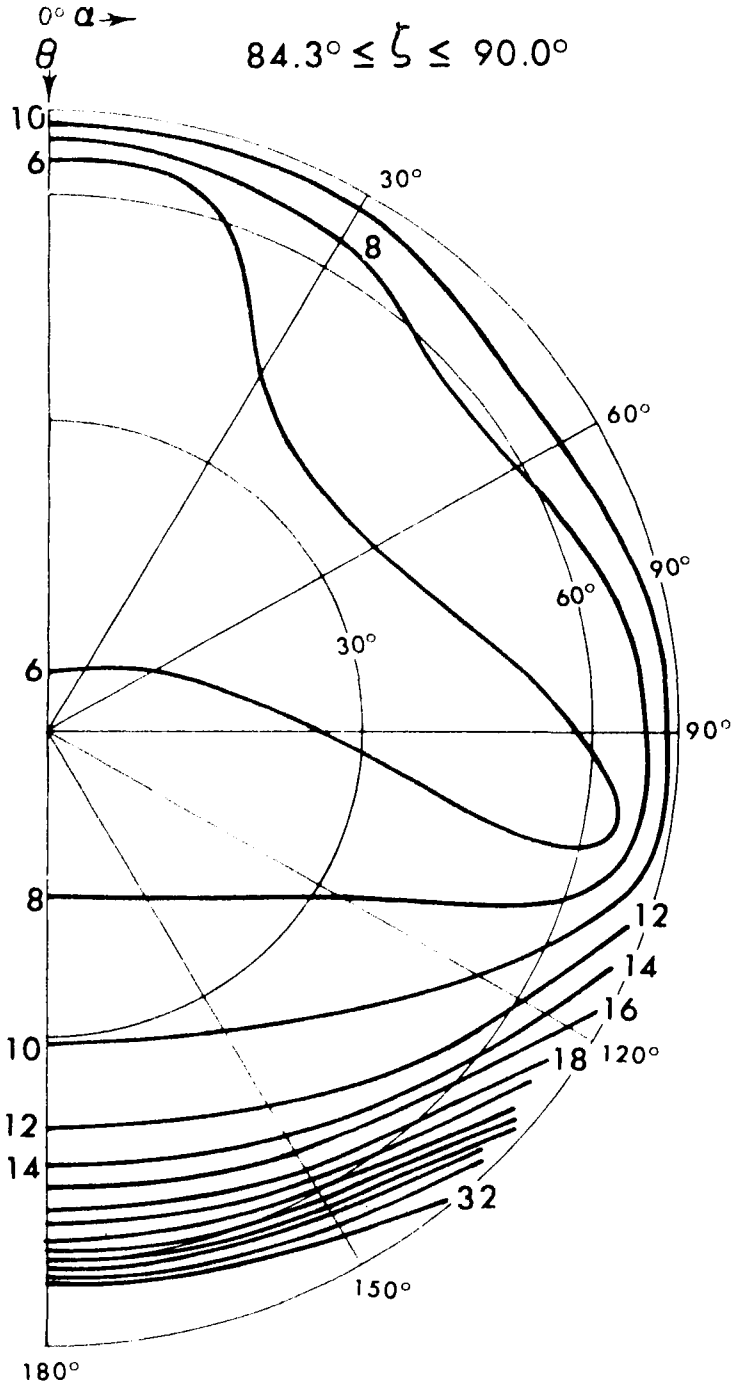

Figure 32. Same as figure 23, for solar zenith angles between 84°.3 and 90°.0.

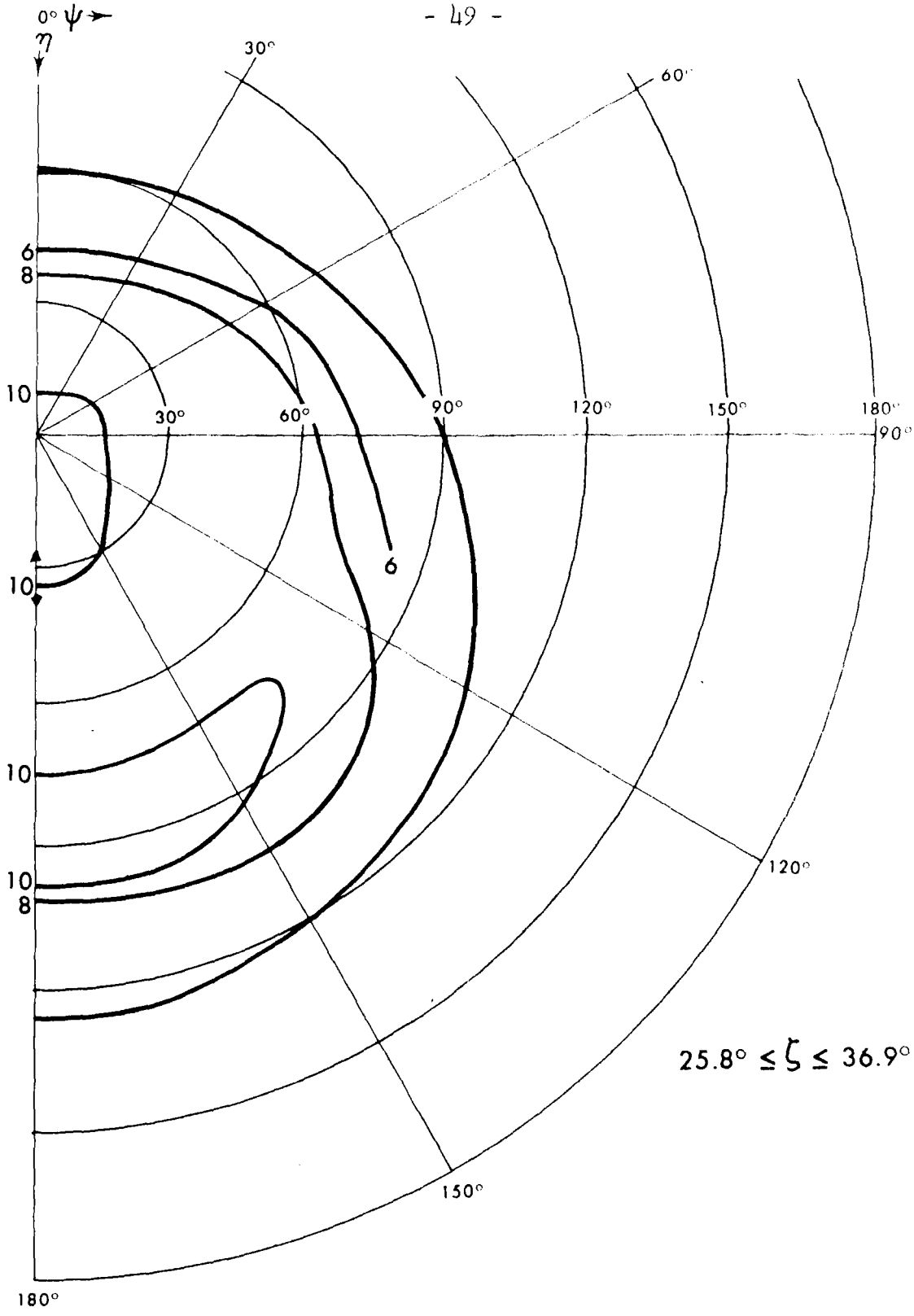

Figure 33. Projection of upward facing hemisphere centered on scattering angle zero, showing symmetrized and smoothed distribution of reflected filtered adjusted intensities (w.m.$^{-2}$ strdn.$^{-1}$) as a function of scattering angle and azimuth. The solar zenith angle lies between 25°.8 and 36°.9. Heavy line surrounding isopleths represents the horizon, and double-headed arrow shows range of zenith position. Approximate unfiltered adjusted intensities may be obtained by multiplying by 12.80.

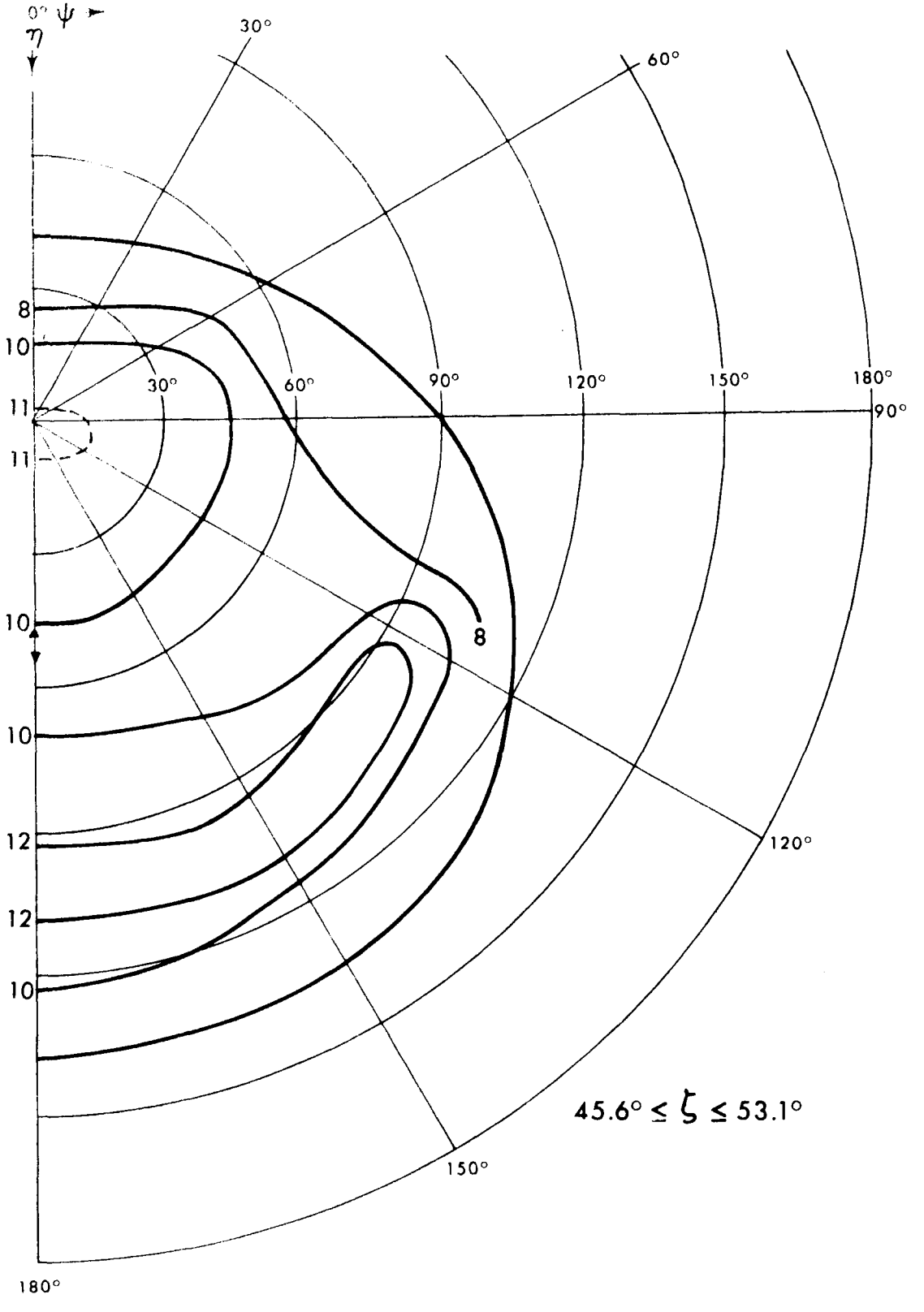

Figure 34. Same as figure 33, for solar zenith angles between 45°.6 and 53°.1.

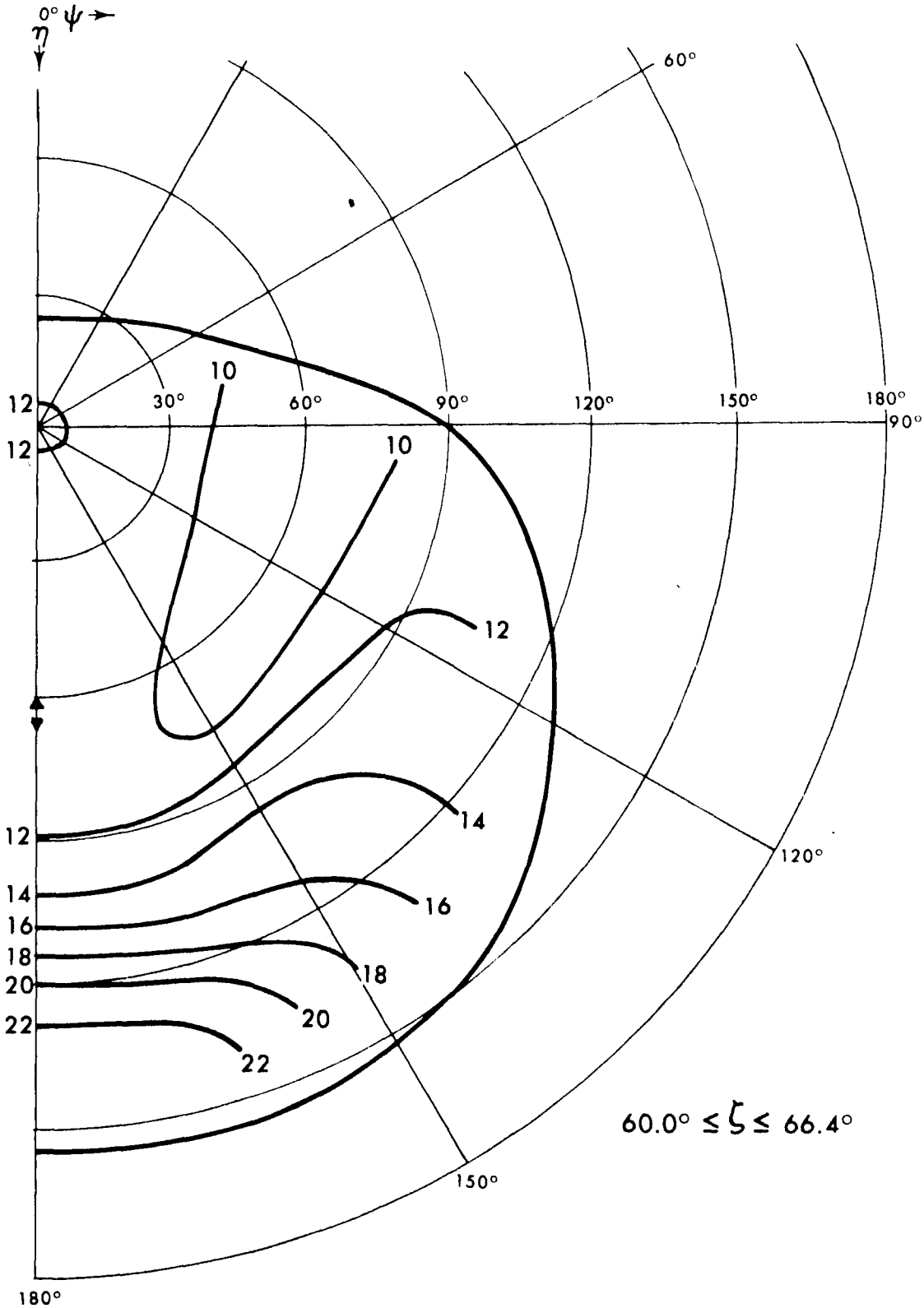

Figure 35. Same as figure 33, for solar zenith angles between 60°.0 and 66°.4.

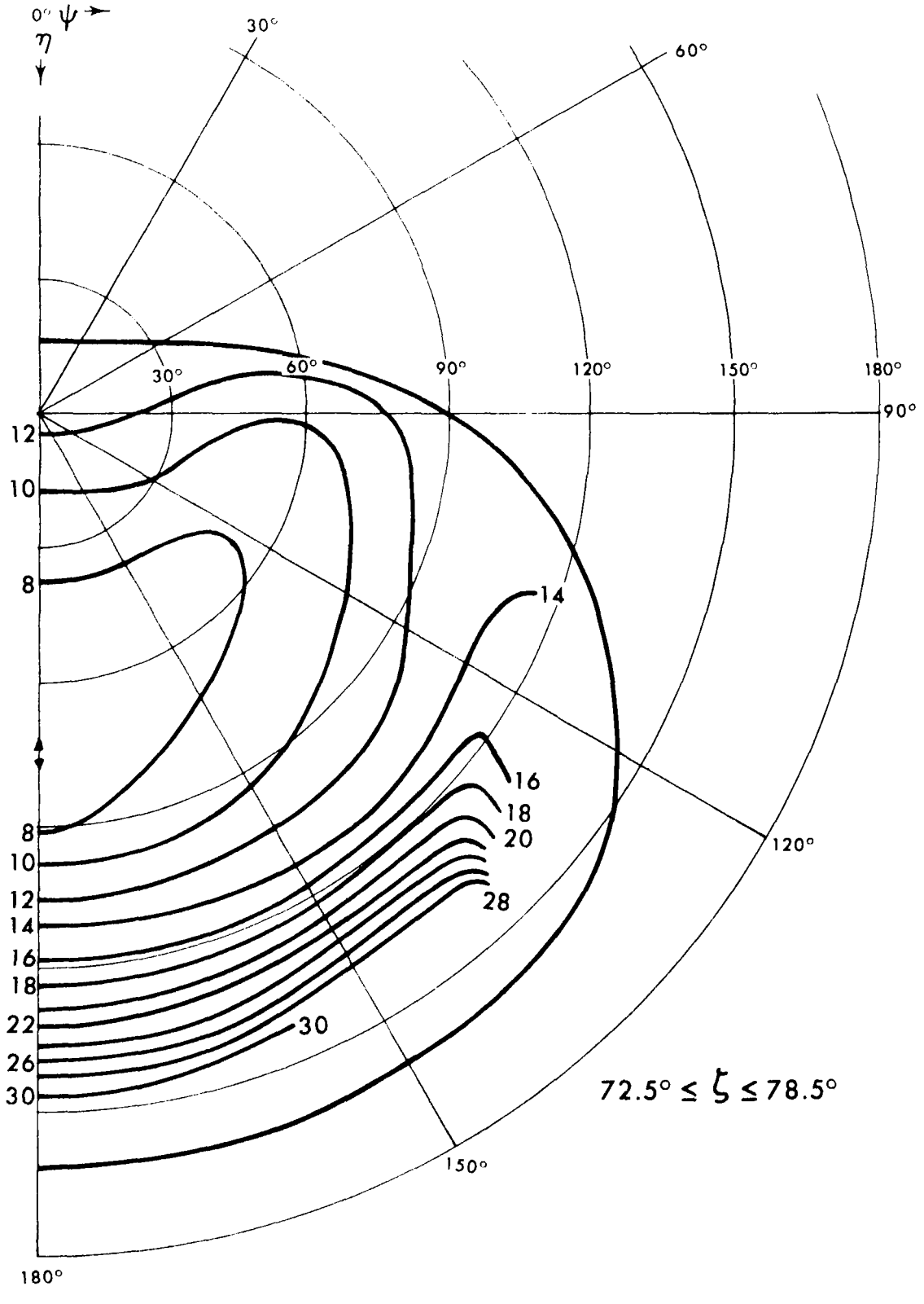

Figure 36. Same as figure 33, for solar zenith angles between 72°.5 and 78°.5.

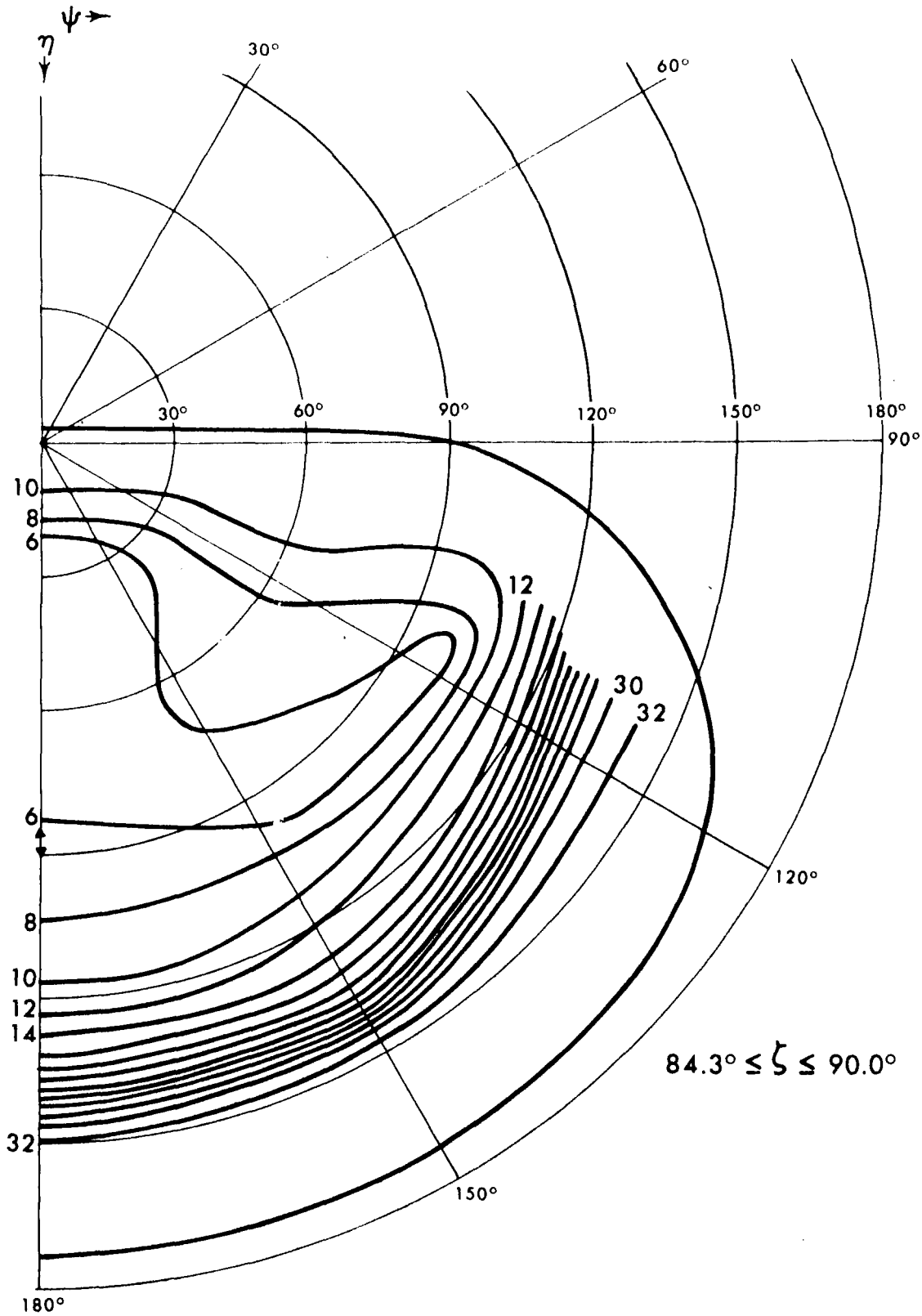

Figure 37. Same as figure 33, for solar zenith angles between 84°.3 and 90°.0.

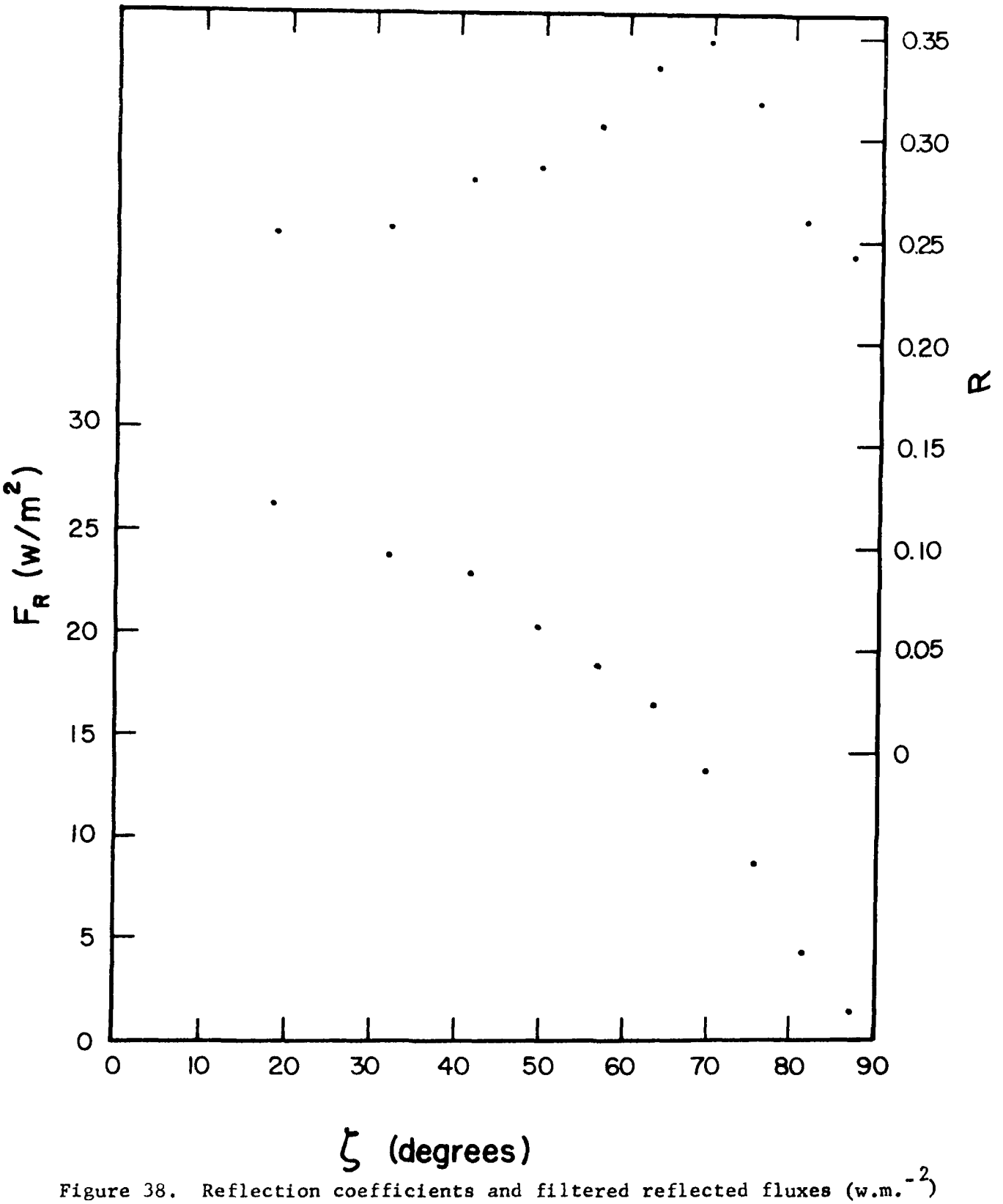

Figure 38. Reflection coefficients and filtered reflected fluxes (w.m.$^{-2}$) as a function of solar zenith angle, computed from intensity distributions of figures 23-32. Approximate unfiltered fluxes may be obtained by multiplying by 12.80.

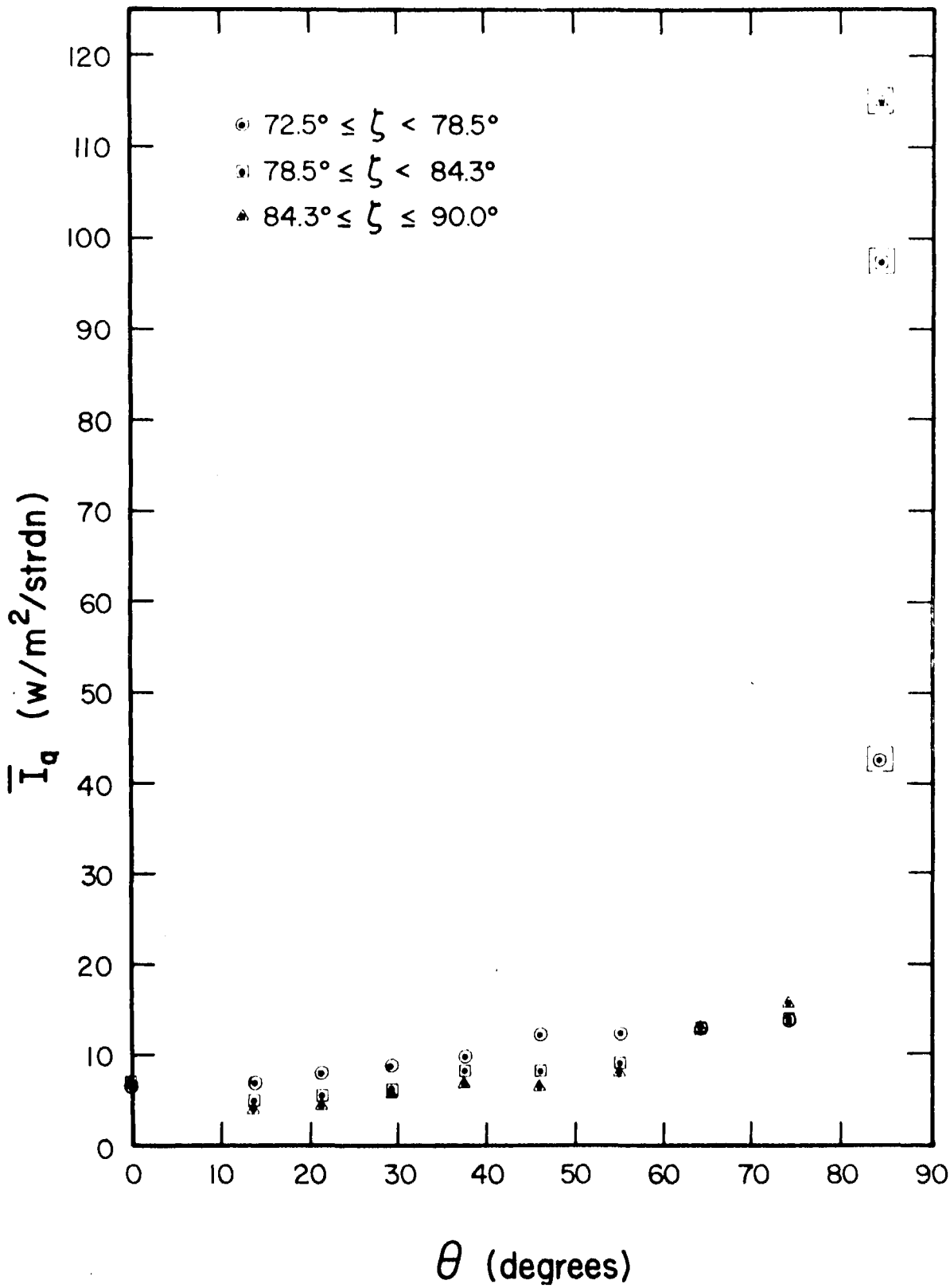

Figure 39. Azimuthal means of filtered reflected adjusted intensity as a function of zenith angle for the three intervals of largest solar zenith angle. The points in brackets, at 0 = 84°.5 are calculated such that the reflection coefficient (shown in fig. 38) will be constant for the four intervals of highest solar zenith angle (i.e., from 66°.4 to 90°.0). Approximate unfiltered adjusted intensities may be obtained by multiplying by 12.80.

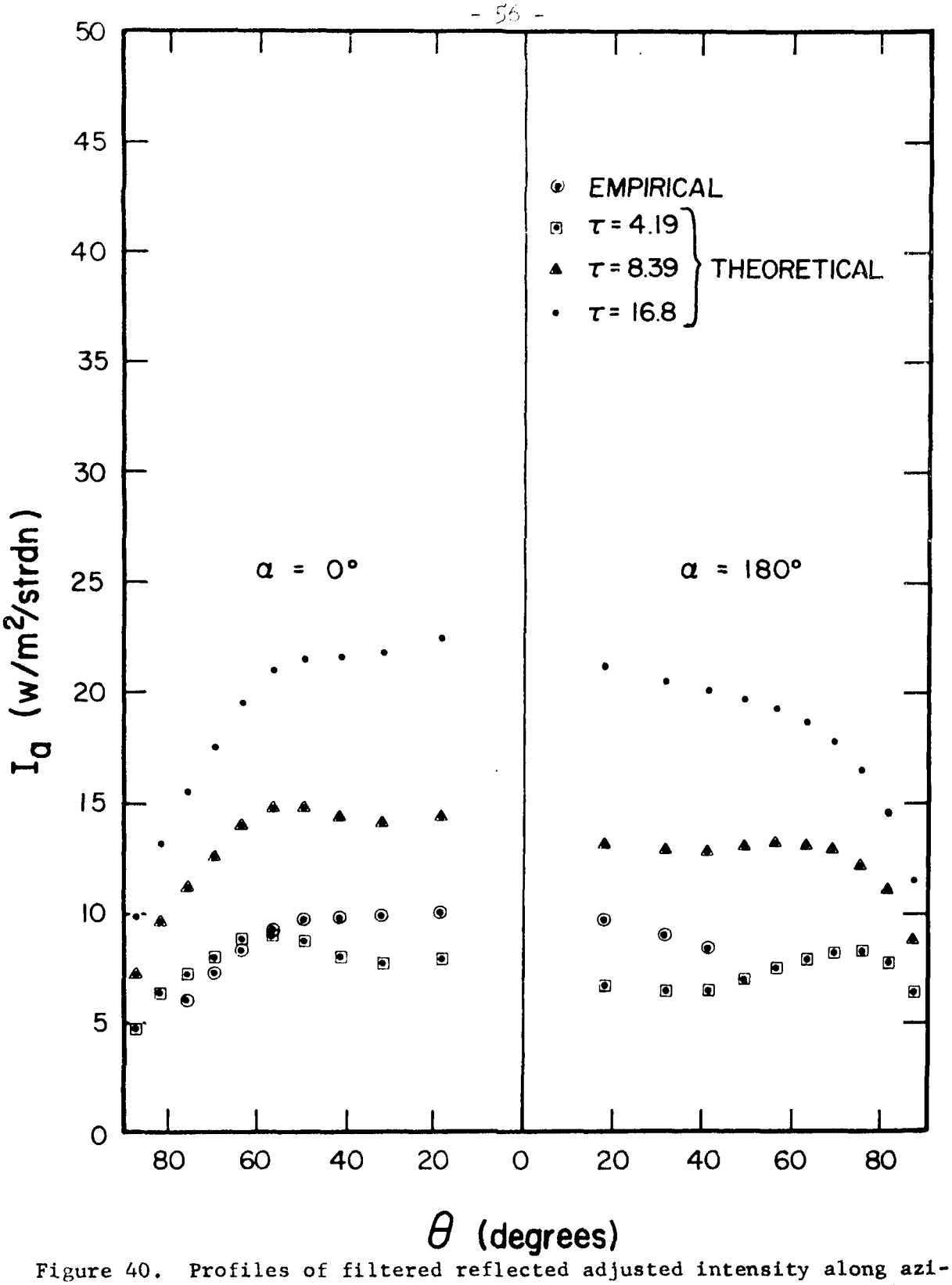

Figure 40. Profiles of filtered reflected adjusted intensity along azimuth 0°-180°, determined from theoretical calculations for three values of optical thickness, and from the symmetrized reflection pattern of this study. Solar zenith angles are between 0° and 25°.8. Approximate unfiltered adjusted intensities may be obtained by multiplying by 12.80.

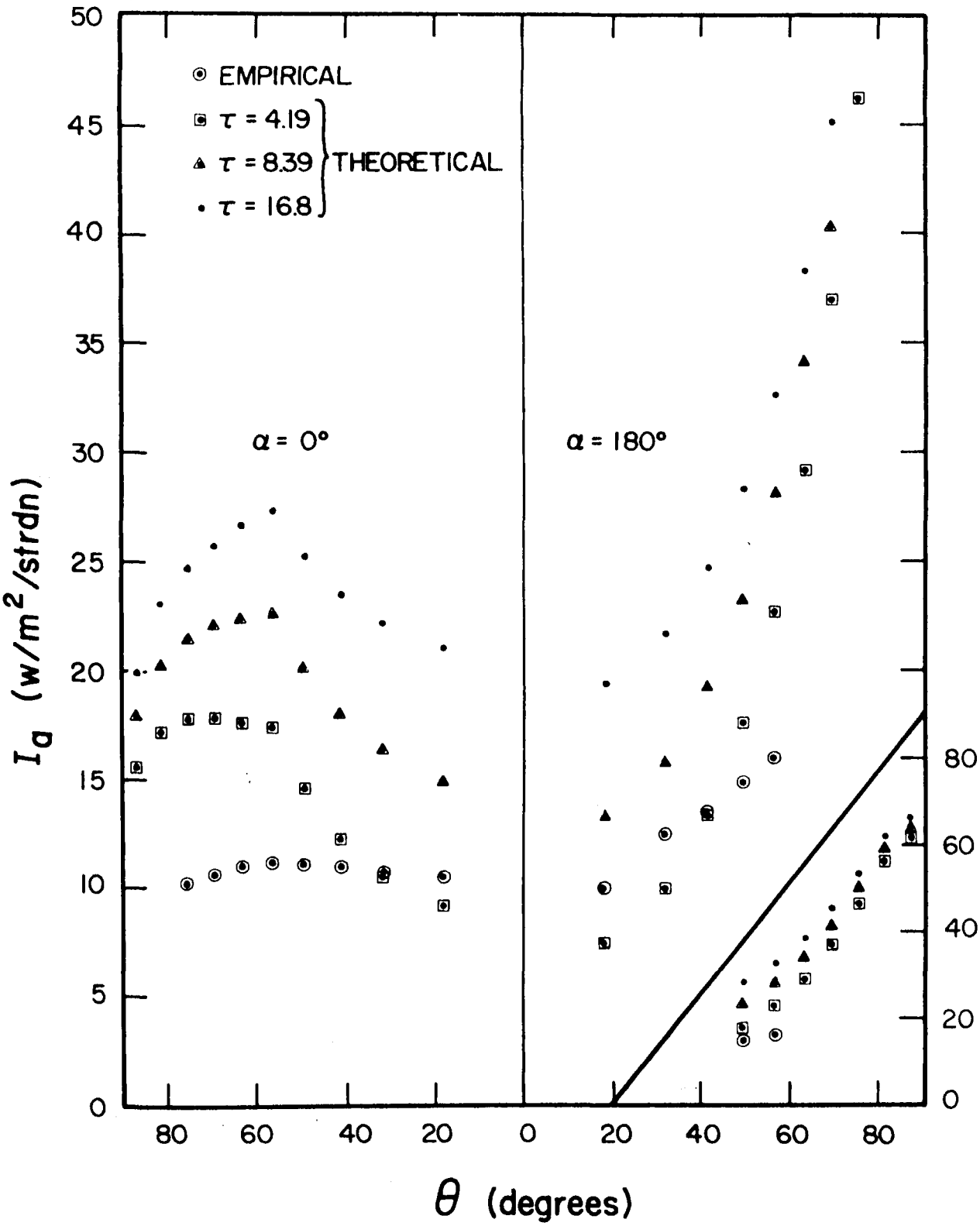

Figure 41. Same as figure 40, for solar zenith angles between 53°.1 and 60°.0.

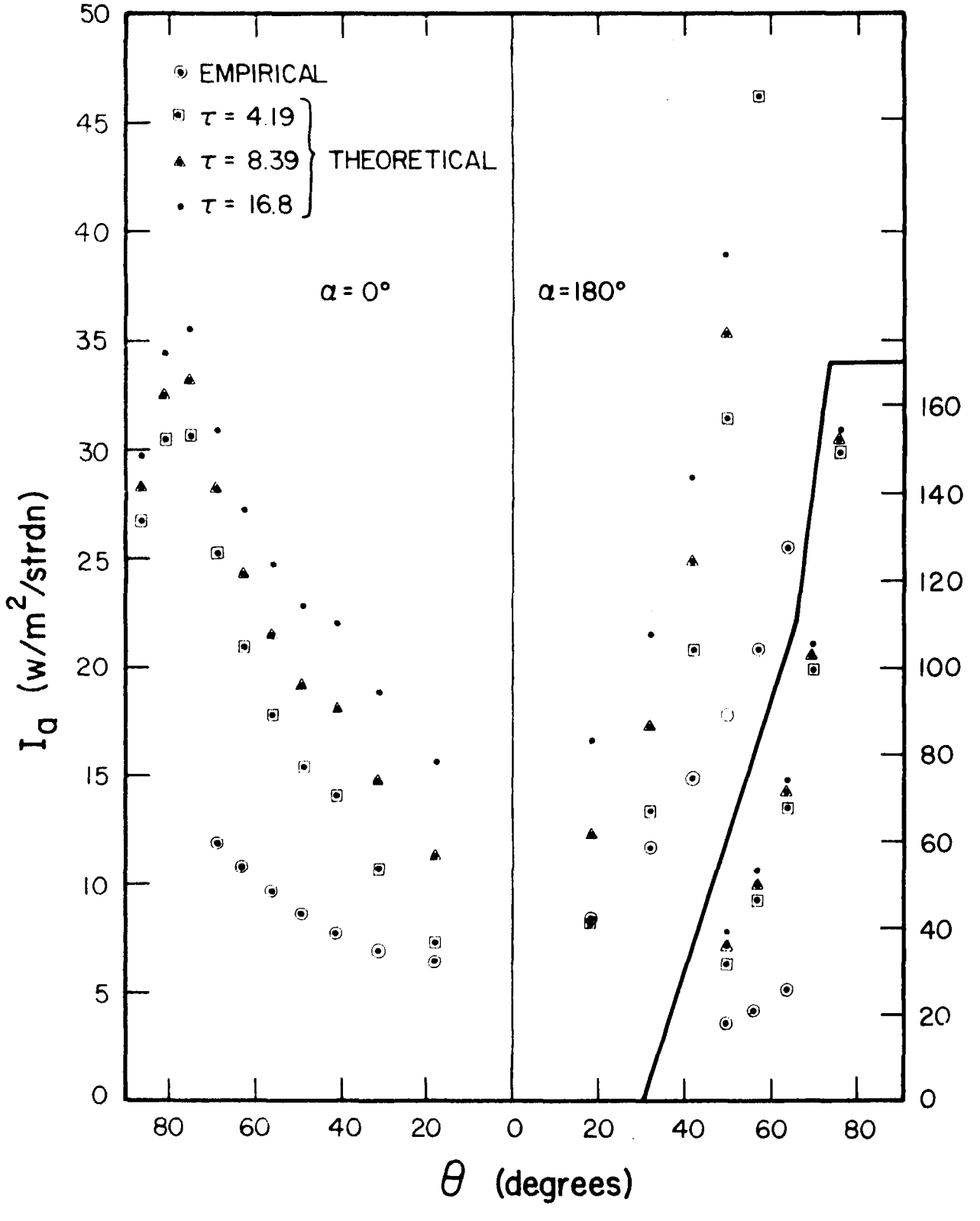

Figure 42. Same as figure 40, for solar zenith angles between 72°.5 and 78°.5.

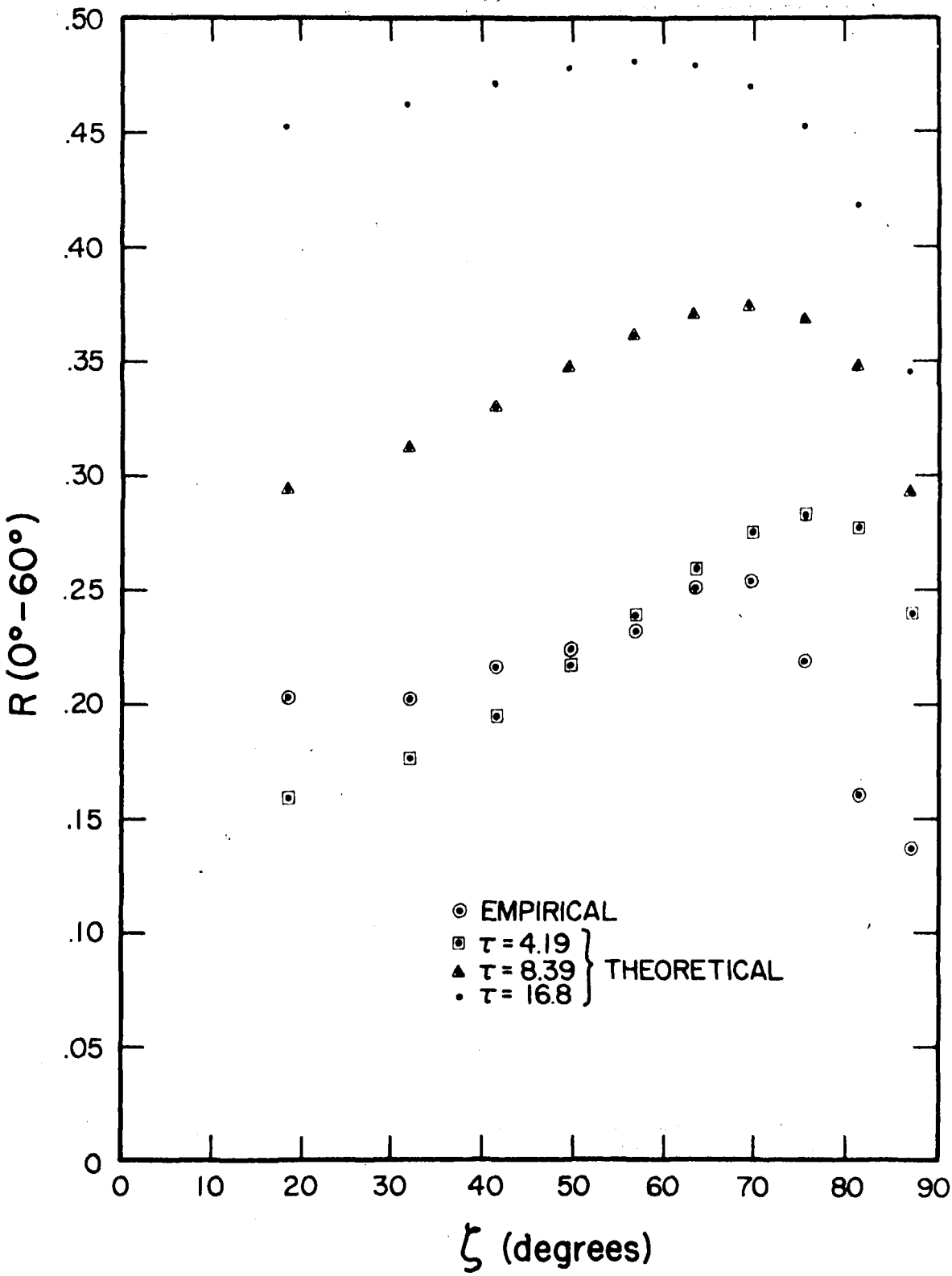

Figure 43. Partial reflection coefficients calculated between zenith angles of 0° and 60°, as a function of solar zenith angle. Points plotted for empirical results and for theoretical calculations for various values of optical thickness.

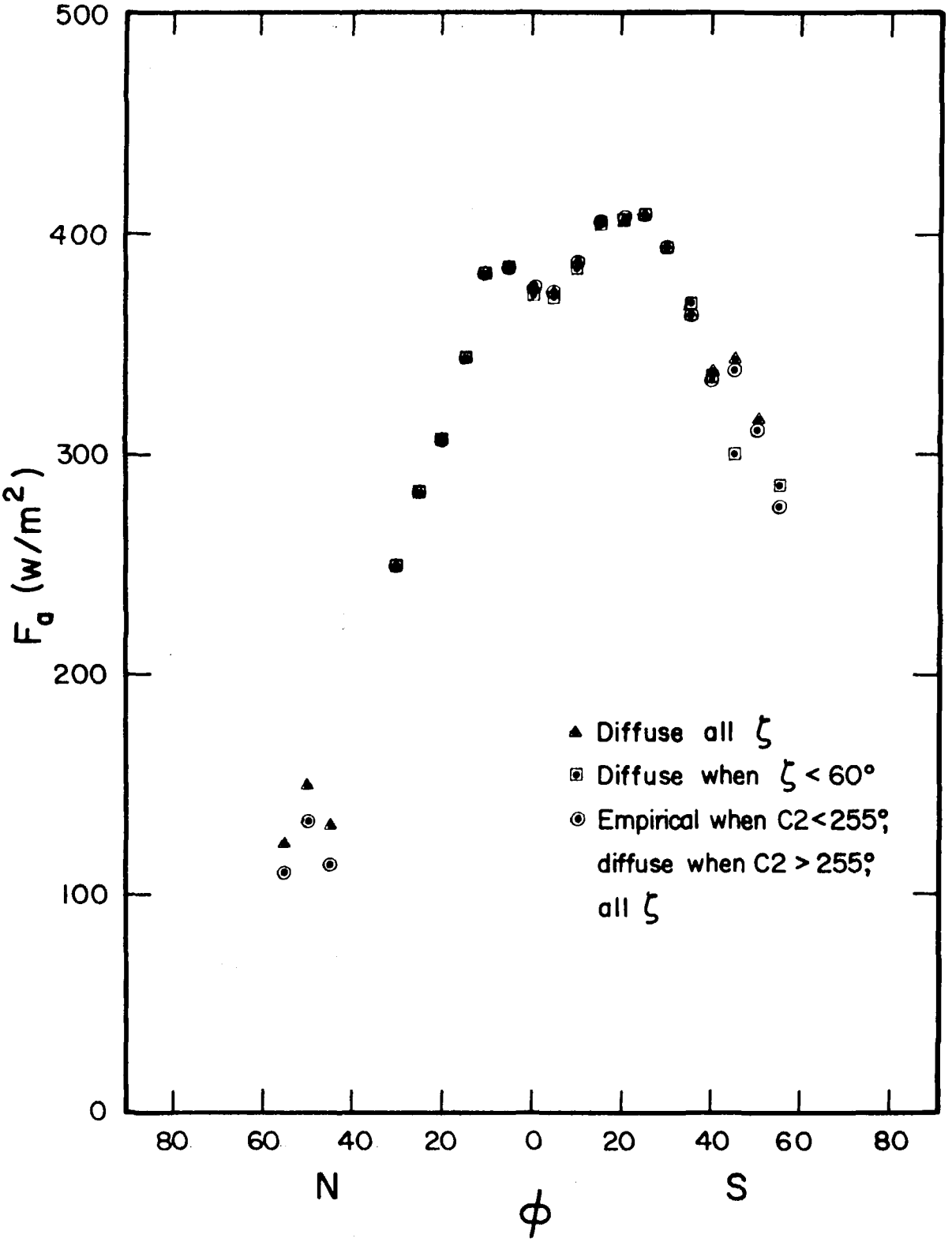

Figure 44. Mean latitudinal absorbed unfiltered flux for February 19, 1962 calculated from TIROS IV, channel 5 observations using (1) diffuse assumption, <60°; (2) diffuse assumption, all ; (3) empirical patterns when T_e for channel 2 is less than 255°K., diffuse when T_e is greater than 255°K.

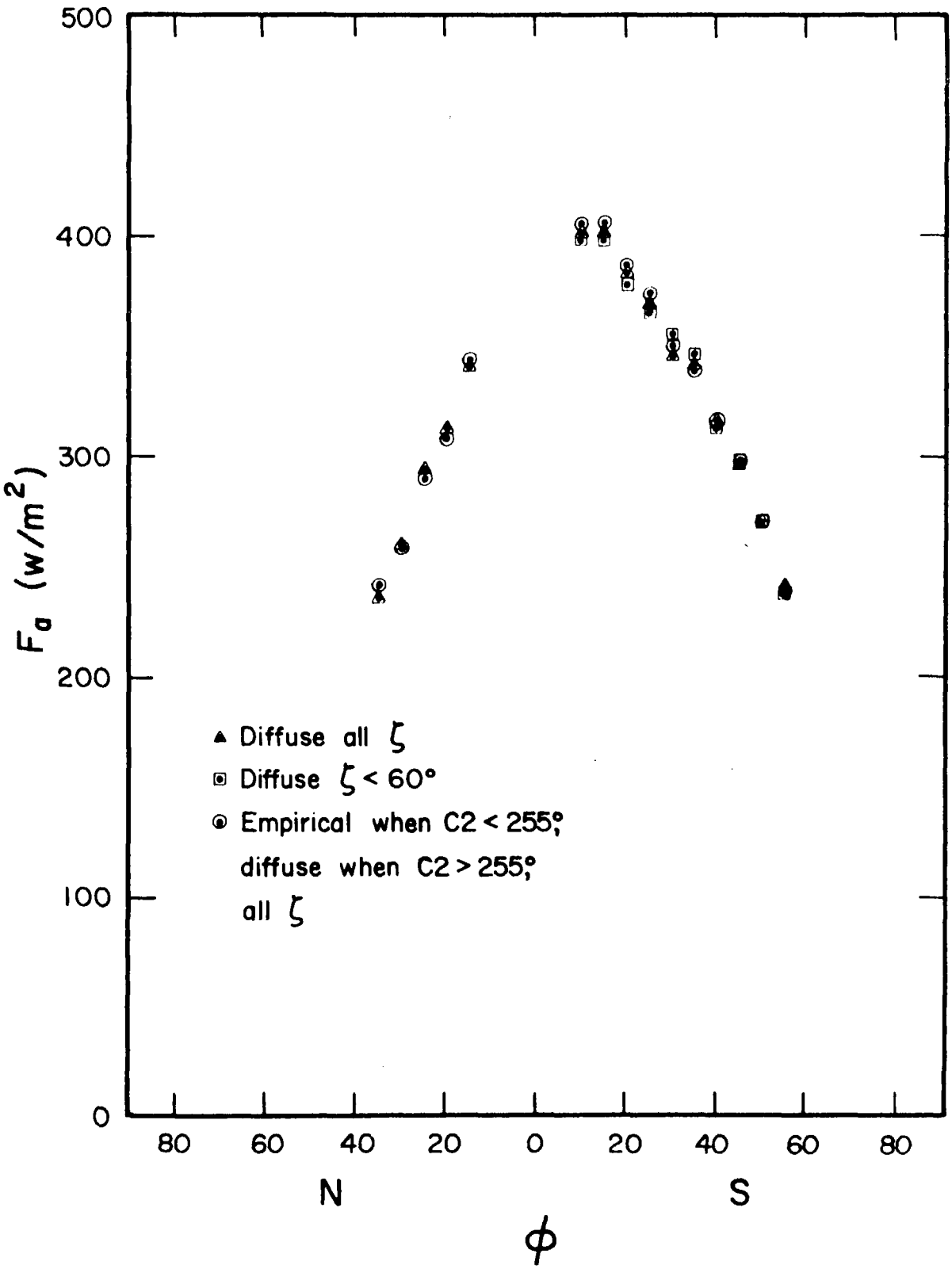

Figure 45. Same as figure 44, for March 5, 1962.

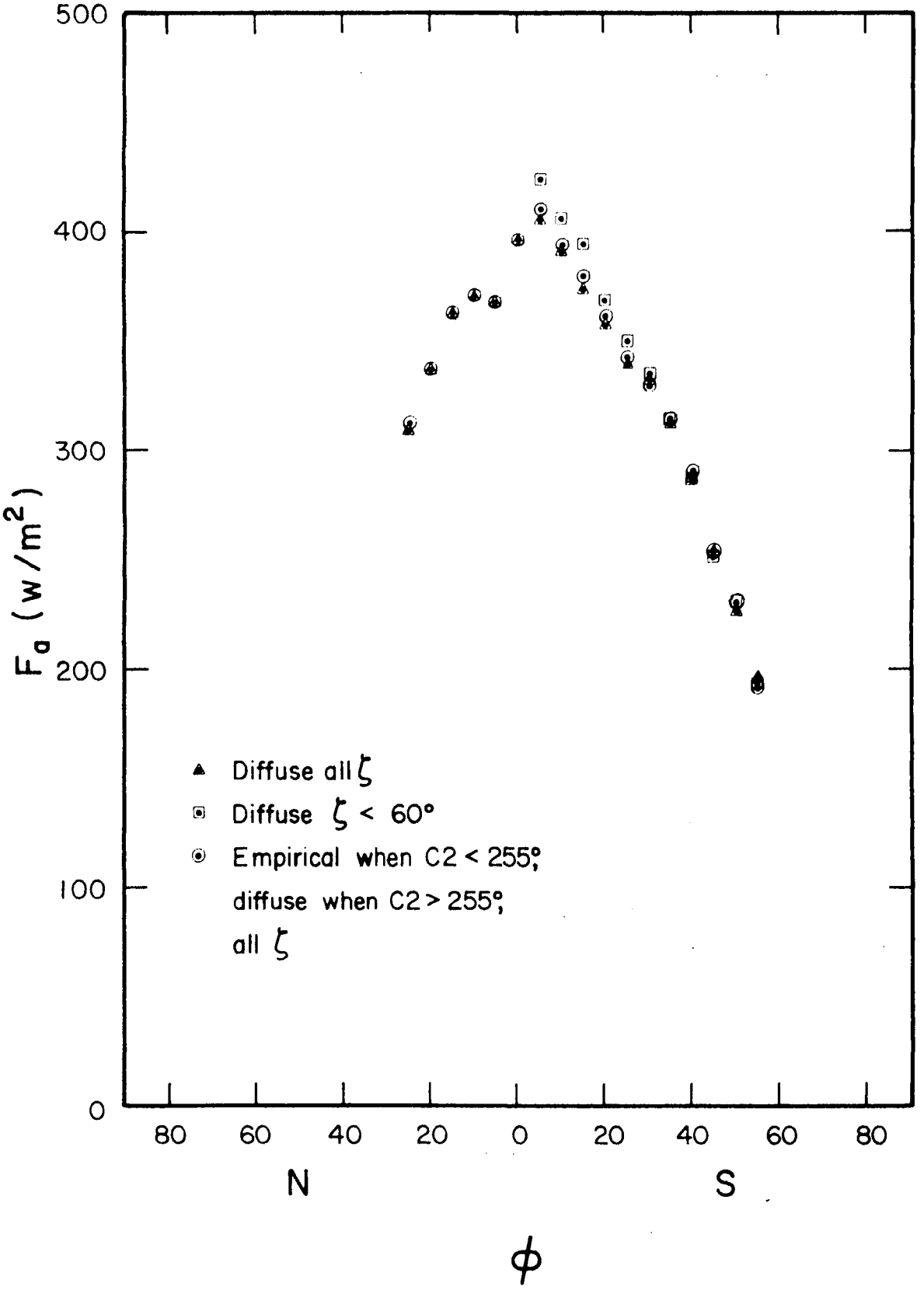

Figure 46. Same as figure 44, for March 15, 1962.

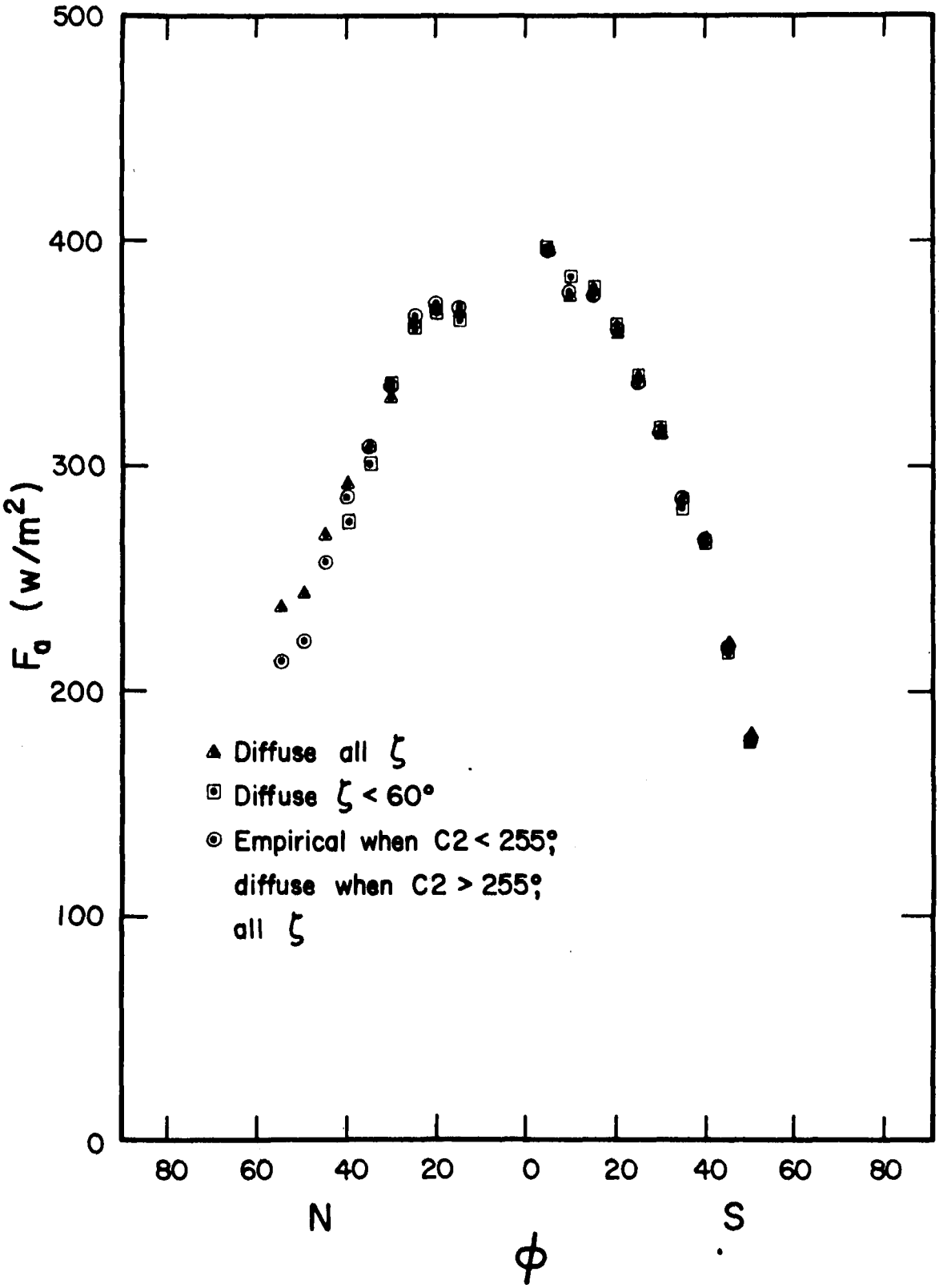

Figure 47. Same as figure 44, for March 25, 1962.

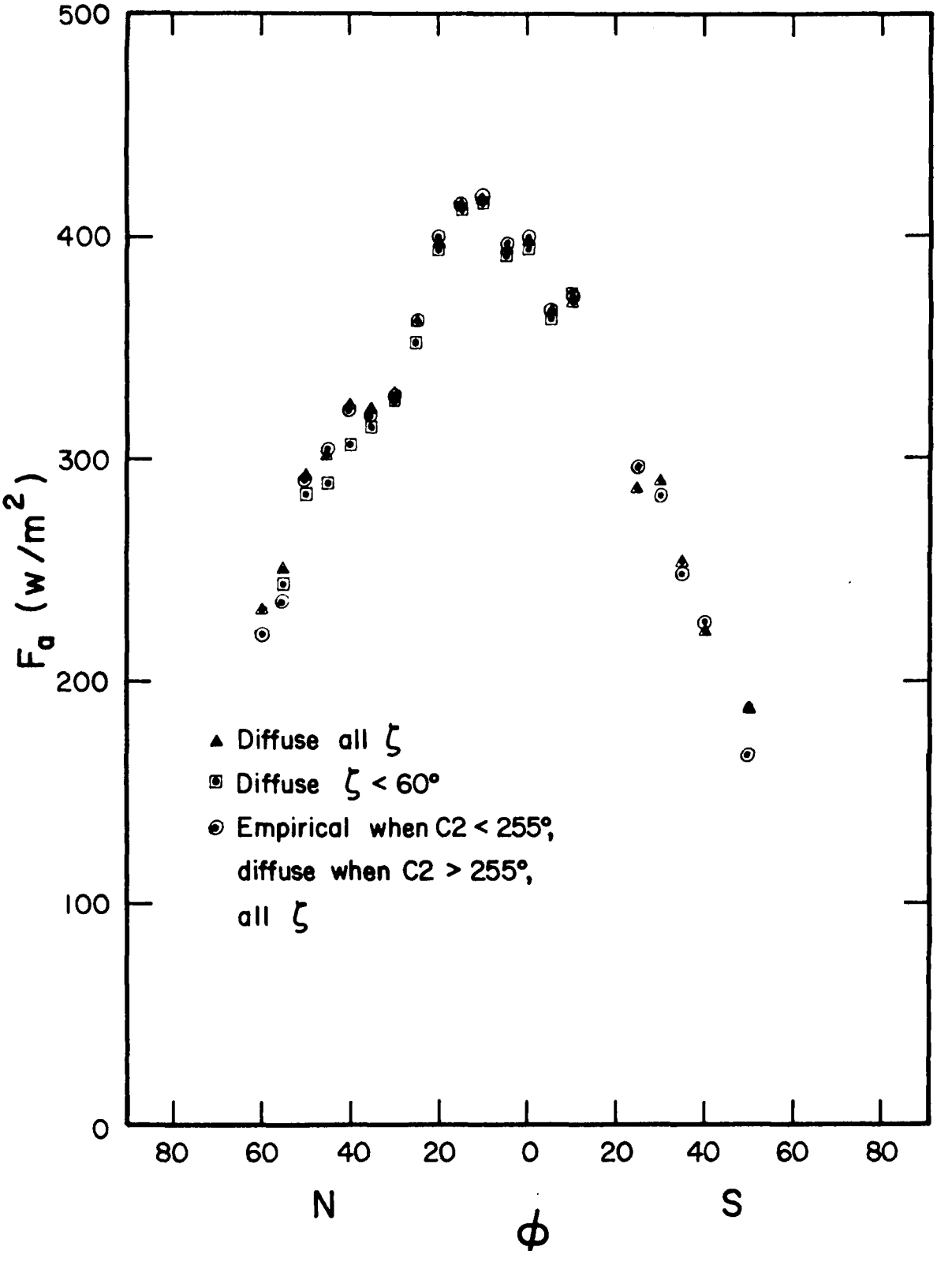

Figure 48. Same as figure 44, for April 5, 1962.

Number

*19. An Investigation of Meteorological Satellite Characteristics of Continuous Earth Coverage, T. I. Gray, Jr., and S. F. Singer, (July 1963) PB 163 745 $4.60

20. Conference on Satellite Ice Studies, M. D. Baliles and H. Neiss, (Ed.), (June 1963) PB 163 746 $9.10

21. Calculations of the Earth's Spectral Radiance for Large Zenith Angles, D. Q. Wark, J. Alishouse, and G. Yamamoto, (October 1963) PB 167 176 $3.00

22. Spectral Reflectance Photography of Earth from Mercury Spacecraft MA-8, S. D. Soules, (November 1963) PB 167 177 $2.00

23. The Use of Satellite Cloud Photographs in Numerical Weather Prediction, M. A. Ruzecki, (December 1963) AD 428 269 $2.60

*24. TIROS Cloud Pattern Morphology of Some Mid-Latitude Weather Systems, H. J. Brodrick, Jr., (January 1964)

25. Number reserved for future report

26. Meteorological Products from Digitized Satellite Vidicon Cloud Pictures, C. L. Bristor and W. M. Callicott, (March 1964) AD 600 078 $1.25

27. Number reserved for future report

28. Automatic Processing of Nimbus Infrared Radiometer Data, G. E. Martin and L. Rubin, (July 1964) PB 166 590 $2.00

29. Tropospheric Conditions Over the Tropical Atlantic as Observed by Two TIROS Satellites and Research Aircraft During 22 September 1962, H. M. Johnson and R. W. Fett, PB 167 178 $4.00

30. Lowlight Coverage from Polar and Sun-Synchronous Orbits, R. L. Pyle, (April 1964) AD 600 970 $.75

31. Specular Spectral Reflectance of Paints from 0.4 to 40.0 Microns, W. Y. Ramsey, (April 1964) PB 167 179 $2.00

32. TIROS Photographs and Mosaic Sequences of Tropical Cyclones in the Western Pacific During 1962, R. W. Fett, (July 1964) AD 608 095 $5.00

33. Wind Speeds from TIROS Pictures of Storms in the Tropics, A. Timchalk, L. F. Hubert and S. Fritz, (February 1965) PB 167 180 $2.00

34. An Investigation of Degradation Errors in TIROS IV Scanning Radiometer Data and the Determination of Correction Factors, P. K. Rao, E. G. Astling, and F. J. Winninghoff (October 1965)

35. Project Storm Cloud - An Aircraft - Satellite Case Study of an East Coast Cyclone, Part 1 - Descriptive Aspects, E. P. McClain and L. F. Whitney, Jr., (December 1965)

36. Experimental Use of Satellite Pictures in Numerical Prediction, Part II, H. J. Brodrick, E. P. McClain, and M. A. Ruzecki, (January 1966)

*37 Mesoscale Cellular Convection, L. F. Hubert, (May 1966)